1

NsG-13

OFFICIAL FILE - TECHNICAL REPORT N67-18031

nasa CR-81691

DRAG FORCES OF TWO-DIMENSIONAL V-SHAPED NOTCHES IN TRANSONIC AND SUPERSONIC TURBULENT FLOW

CASE FILE
COPY

RECEIVED
JAN 13 1 22 PM '67
OFFICE OF GRANTS &
RESEARCH CONTRACTS

BY

RONALD HUNTER HOWELL

B.S., University of Illinois, 1958

M.S., University of Illinois, 1959

THESIS

Submitted in Partial Fulfillment of the Requirements
for the Degree of Doctor of Philosophy in Mechanical Engineering
in the Graduate College of the
University of Illinois, 1967

Urbana, Illinois

OFFICIAL FILE
14-005-001
SECTION Copy file PER OG

㉚

REPORTS CONTROL No. SC-4425

DRAG FORCES OF TWO-DIMENSIONAL V-SHAPED NOTCHES IN TRANSONIC AND SUPERSONIC TURBULENT FLOW

BY

RONALD HUNTER HOWELL

B.S., University of Illinois, 1958

M.S., University of Illinois, 1959

THESIS

Submitted in Partial Fulfillment of the Requirements
for the Degree of Doctor of Philosophy in Mechanical Engineering
in the Graduate College of the
University of Illinois, 1967

Urbana, Illinois

ACKNOWLEDGEMENT

The author expresses his gratitude to his adviser, Dr. Helmut H. Korst, whose guidance and insight made this thesis possible. Thanks are also due Messrs. R. H. Crawford and L. W. Hirschler for the construction of the experimental apparatus and the operation of the mechanical equipment involved in this investigation. Acknowledgement is also made to Dr. A. L. Addy for the design of the preamplifier and to Dr. R. A. White for reviewing and checking the manuscript. Thanks is also given to Professor H. S. Stillwell of the Aeronautical and Astronautical Engineering Department for the use of his departmental facilities.

This investigation was conducted with the support of the National Aeronautics and Space Administration under their University Research Program Grant NsG 13-59, and their financial support is gratefully acknowledged.

The author also expresses his gratitude to his father, Harry A. Howell, for his encouragement and assistance during this investigation. Finally, the author is indebted to his wife Nancy for her patience and understanding during this work.

TABLE OF CONTENTS

Page

I. INTRODUCTION 1

II. LITERATURE REVIEW 7

A. Rectangular Notch Drag 7

B. Flow Components 14

C. Surface Skin Friction 19

III. PROBLEM ANALYSES 21

A. Basic Flow Model 21

B. Basic Flow Interactions 26

C. Direct Measurement of Drag Forces 27

D. Theoretical Analysis for Turbulent Flow over a Finite Length Flat Plate 28

E. Drag Force Analysis for the V-Notch 37

1. Drag Coefficient for V-Shaped Notches . . 37

2. Form Drag and Friction Drag 38

3. Phenomenological Flow Models 40

a) Shock-Expansion Theory 42

b) Linearized Supersonic Theory 44

c) Transonic Drag Force Theory 48

i) Utilization of Shock-Expansion Theory 49

ii) Mach Freeze Concept for Low Supersonic Approach Mach Number . . . 50

iii) Transonic Similarity Relations . 51

F. Drag Force Due to Boundary Layer Rehabilitation Downstream of the V-Notch 53

Page

IV. EXPERIMENTAL INVESTIGATION 55
- A. Experimental Objectives 55
- B. Blowdown Facilities 56
- C. Design of the Drag Force Balance 58
- D. Calibration and Testing 66
  - 1. Classification of the Supersonic Turbulent Boundary Layer 68
  - 2. Classification of the Transonic Turbulent Boundary Layer 72
  - 3. Accuracy of Flat Plate Measurements . . . 74
  - 4. Plate Misalignment Effects 77
  - 5. Effectiveness of the Labyrinth Seals . . 78
- E. Notch Drag Force Models 78

V. EXPERIMENTAL RESULTS FOR V-NOTCHES 80
- A. Separation Point Studies 80
- B. Supersonic Drag Coefficients 81
- C. Transonic Drag Coefficients 83
- D. Drag Force Test for Determining the Friction Drag of the Downstream Redevelopment 83

VI. DISCUSSION OF RESULTS 86
- A. Thin Approaching Boundary Layers 87
  - 1. Supersonic Results, $M_e \cong 2$ 88
    - a. Reynolds Number Effect 88
    - b. Notch Angle Effect 89
    - c. Shear Layer Effect 91

Page

2. Transonic Results, $M_e = 0.6$ to 1.18 . . . 91
    - a. Notch Angle Effect 92
    - b. Shear Layer Effect 93
    - c. Mach Number Effect 94

B. Thick Approaching Boundary Layers 96

1. Supersonic Results, $M_e \approx 2$ 96
    - a. Reynolds Number Effect 97
    - b. Notch Angle Effect 97
    - c. Shear Layer Effect 97

2. Transonic Results, $M_e = 0.6$ to 1.18 . . . 98
    - a. Notch Angle Effect 98
    - b. Shear Layer Effect 98
    - c. Mach Number Effect 99

C. Drag Forces of Rectangular and Circular Cavities 99

D. Redeveloping Shear Layer Drag Downstream from the Notch 100

VII. CONCLUSIONS AND RECOMMENDATIONS 101

LIST OF SYMBOLS 104

FIGURES 108

BIBLIOGRAPHY 155

APPENDIX 160

VITA 168

I. INTRODUCTION

As the speed of aircraft increases toward sonic velocity and further into the supersonic regime accurate information about local details in the surface configuration of the aircraft assume great importance. In the subsonic range of velocity, the effect of surface discontinuities such as protuberances, steps, and notches is not as prominent as in the supersonic regime. In passing through the transonic flow regime however, the drag coefficient for surface discontinuities can change by an order of magnitude. A better understanding of lift and drag force contributions by such disturbances as well as knowledge of the detailed flow mechanisms which determine aerodynamic stress distributions and heat transfer characteristics near such disturbances is necessary.

Traditionally flow separation at surface discontinuities has been considered a disadvantage in flight vehicles. However, separation can often be used to advantage for modifying aerodynamic lift and drag forces (spoilers and re-entry vehicles), amplifying thrust forces and influencing aerodynamic heating phenomena.

Many types of fluid handling devices such as compressors, jet engines, and gas turbines have local flow velocities in the region of sonic flow. As the design of these machines becomes more refined it also becomes necessary to have accurate information about the effects created by the presence of surface discontinuities.

Former design techniques used approximate empirical coefficients for the drag increase due to surface discontinuities. Some of these empirical drag coefficients are presented in Reference 22 and are discussed later. In many instances one had to rely on such data for approximate values of the drag coefficient even though the anticipated conditions were at best only close to the conditions under which the published drag coefficients were obtained. For many subsonic flows the differences in the flow characteristics and notch or protuberance geometries were unimportant while in transonic and supersonic flows they can become decisive factors.

Of special interest then are such surface configurations where not only the exact geometry of the walls but the details of the approaching and adjacent flow fields assume a major role in determining the solution to the problem. In contrast to the rather well defined boundary conditions (walls) for attached flows the occurrence of separation often allows major adjustments in the flow geometry as a consequence of small changes in flow conditions. Where flow separation is a prominent feature and where the dynamics of the flow field are the results of interactions between hydrostatic and viscous stresses associated with attached and free shear layers, understanding has remained incomplete in spite of proposed flow models and their utilization in analytical approaches. Examples of such theoretical models include those proposed by Crocco and Lees (Reference 13), Lees and Reeves (Reference 32), Chapman (Reference 8) and Korst (Reference 27).

From among the many geometries of interest the v-notch configuration has been selected for the present study for both practical and conceptually attractive reasons. The choice was practical because it has a bearing on the drag penalties of uncovered secondary flow intakes for ejector nozzles and it was conceptually attractive because it promised insight into the mechanisms of self adjusting flow geometries especially in the region of the transonic drag rise. The problem which was analyzed here was that of the increase in the drag force due to the presence of a v-shaped notch in a flat surface. Diagram 1 illustrates the wall geometry and flow configuration. The wall geometry was two-dimensional and remained restricted to symmetrical notches; the approaching boundary layer was always turbulent and the external flow was adiabatic and compressible and was either transonic or supersonic in nature.

For any given notch geometry (notch length L, notch angle $\Omega = \tan^{-1} 2\,r/L$), the free stream Mach number M_e

is to be considered the primary variable, but a full specification of viscous effects is also necessary. The latter requires the identification of a reference Reynolds number associated with the free stream and based on a suitable reference length, e.g., the virtual or apparent turbulent length x, and it also requires detailed information concerning the approaching boundary layer. The approaching boundary layer is specified by a reference thickness and a shape parameter. For the present investigation the approaching boundary layer was always turbulent and reasonably well representative of fully developed shear layers along adiabatic flat plates (thus defining the shape parameter $H = \delta^*/\theta$). Consequently, one could then rely on the momentum thickness θ, as a single specifying parameter for the approaching boundary layer. These quantities are indicated in Diagram 1.

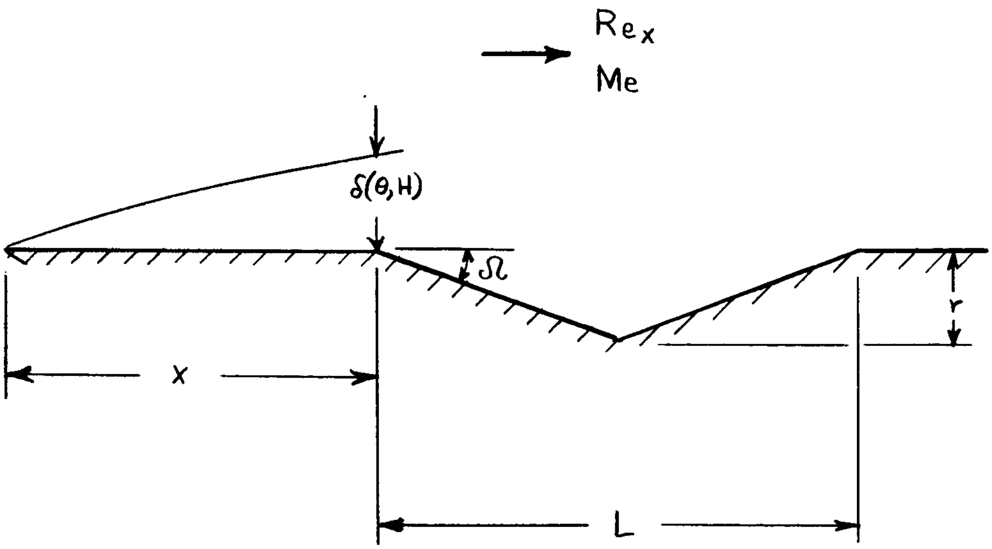

Diagram 1. Notch Geometry and Flow Variables

While it is desirable to develop an analysis capable of dealing with all the significant variables of the problem in both qualitative and quantitative aspects, the complexity of the flow phenomena indicated that an experimental investigation was needed to gain a better understanding of the detailed components and the mechanisms of their interactions. Recently, progress has been made in the analysis of laminar flows of similar nature, e.g., Lees and Reeves (Reference 32) and Holden (Reference 53). However, the present status of incomplete understanding of the shear layer-shock wave interactions, shear layer expansions, flow separation, free shear layer development in close proximity to walls, reattachment and attached shear layer redevelopment in the turbulent regime makes an entirely analytical approach unfeasible.

The experimental program, which was a major portion of this investigation, consisted of designing, constructing and operating a balance which measured directly the drag force of the v-notch. The balance was designed with enough versatility so that various two-dimensional configurations could be installed and their drag forces measured. These results are presented in the following sections.

As indicated above the major objective in this investigation was the determination of the drag of a v-shaped notch; however, several other aspects and effects were analyzed which were related to the notch flow problem. One was the effect of Mach number on the drag force near Mach number equal to unity. The data which were obtained indicated a displacement and a smoothing out of the theoretical maximum value of the drag coefficient near Mach number equal to one. Another effect that was investigated was that of the drag force in the region of a redeveloping boundary layer on a flat plate. This type of flow region existed immediately behind the notch. Tests were conducted to determine how far the influence of the notch was felt downstream of the notch.

In a broader sense, the investigation appears to be useful as it yields knowledge of the variation of the drag force from a region of attached flow to a region of separated flow. Or, it gives the drag variation from the skin friction on a flat surface to drag in a mixing region over a deep cutout.

The conditions under which the experiments were conducted did not give rise to non-steady phenomena. In particular, resonant conditions which are often observed for flows past relatively deep cavities (Reference 30) were not evident during this investigation.

II. LITERATURE REVIEW

An investigation of the relevant journals and reports revealed that no directly applicable theoretical analysis of the stated problem was available, especially in the turbulent regime, and also that no information on experimental drag coefficients for the specified flow conditions existed. However, some pertinent analyses have been made which furnish useful direction for dealing with the stated problem. The presentation of this relevant material will be made in three parts, rectangular notch drag, definition of interactions between component flow regimes, and surface skin friction as related to both the notch flow problem itself and experiments intended to establish the accuracy of a force balance designed for this investigation.

A. Rectangular Notch Drag

Roshko (Reference 40) presented experimental results dealing with flow in a rectangular cavity with subsonic flow passing over the cavity. Roshko's results indicated that there was a pronounced effect on the flow field as the depth to width ratio was changed. This effect was demonstrated in his work with a plot of the pressure coefficient for the cavity floor as a function of the depth to width ratio. A schematic representation of this data is shown in Diagram 2.

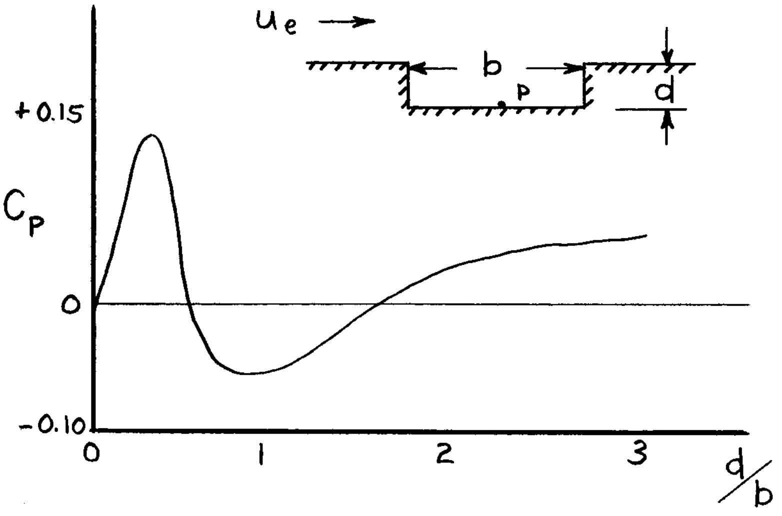

Diagram 2. Cavity Pressure Coefficient (Reference 40)

Hoerner (Reference 22) also presented results for drag coefficients of rectangular cutouts in subsonic flow. Two general types of cavities were considered; the deep notch where the external stream did not reattach to the bottom of the cavity floor and the shallow notch where the external stream did reattach to the bottom of the cavity floor. Diagrams 3 and 4 show the results of those tests.

These two diagrams depict the general trends for drag coefficients of notches. In Diagram 3 at h/e equal to approximately 0.8 the drag coefficient was a maximum and the external stream was attached to the bottom of the notch. As h/e was decreased the flow remained attached to the center portion of the bottom of the notch and the drag coefficient

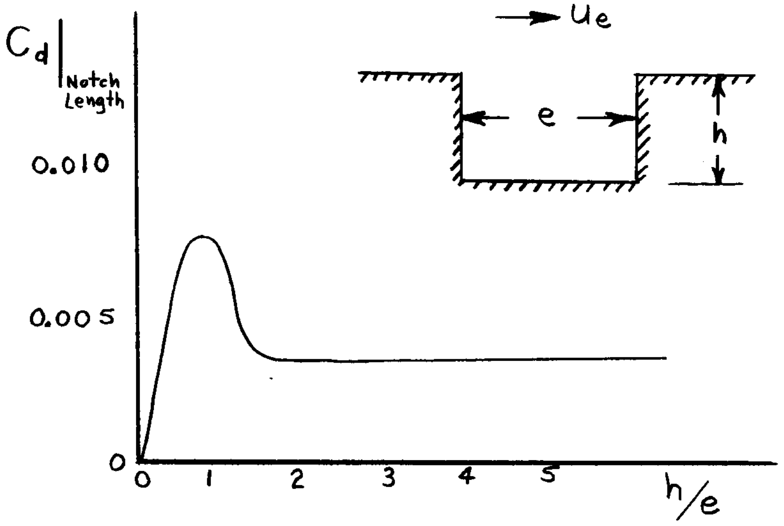

Diagram 3. Groove Drag Coefficients (Reference 22)

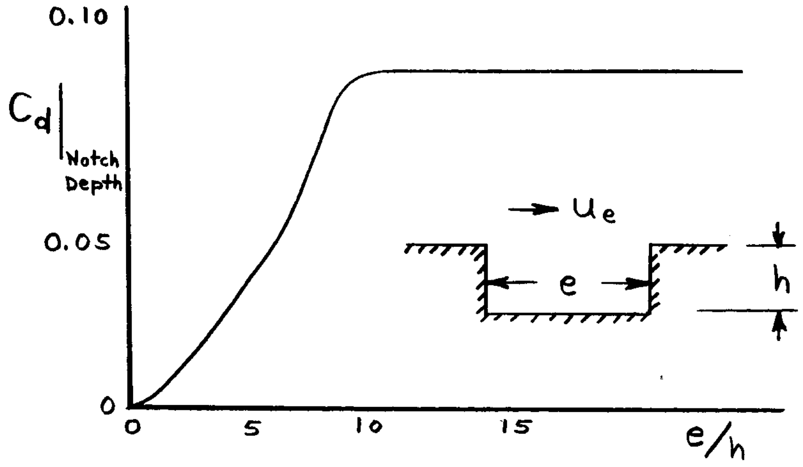

Diagram 4. Groove Drag Coefficients (Reference 22)

decreased with decreasing h/e. As h/e was increased the external stream became detached from the bottom of the notch and the drag coefficient decreased and then leveled off to a constant value. In Diagram 4 as e was increased the external flow became attached to the bottom of the cavity and the defined drag coefficient remained constant.

Thomke (Reference 47) has reported experimental data for supersonic turbulent flow over downstream facing steps and over rectangular cavities. Surface pressure measurements were made along with boundary layer traverses for a Mach number range of 2 to 4 and step heights of 0.25, 1.02, and 1.675 inches. For the cavity experiments the cavity length was varied and the data indicated that the same qualitative remarks concerned with drastic changes in the flow field apply for supersonic flow over notches as were stated for subsonic flow and reported by Hoerner (Reference 22).

Chapman, Kuehn, and Larson (Reference 8) presented experimental results for separated flows in subsonic and supersonic streams. The majority of their data were for the pressure rise near separation points for flow over front facing steps, at compression corners, on curved surfaces, and at shock reflections. However, for the present investigation their results were of qualitative value even though the flow configurations were different in as much as they gave information on the reattachment of free shear layers.

A more pertinent investigation was that by Charwat, Roos, Dewey, and Hitz (Reference 9). Their presentation described an investigation of separated regions near cutouts and ahead of and behind two-dimensional steps for a supersonic external stream with an approaching turbulent boundary layer. The authors found that there was a critical value for the ratio of the length of the separated free shear layer to the depth of the cavity beyond which the cavity became two separated regions. They reported that this critical length was nearly independent of Mach number and Reynolds number for turbulent flow. Additional insight into this problem has been gained through a theoretical study by Golik (Reference 20) where he showed that for low supersonic Mach numbers this critical length increased strongly for decreasing approach Mach number.

Charwat, et al., (Reference 9) calculated the drag force of a notch in a plate from measurements of the surface pressures on the notch faces normal to the free stream. The results of their calculations are shown in Diagrams 5 and 6.

It should be noted in Diagram 5 that the drag coefficient decreases with an increasing free stream Mach number for long notches. This result indicates that the basic nature of the flow over a notch is different for short notches and long notches. For turbulent flow over a long notch the stream is partially deflected into the cavity and Charwat, et al., proposed that the pressure distribution for

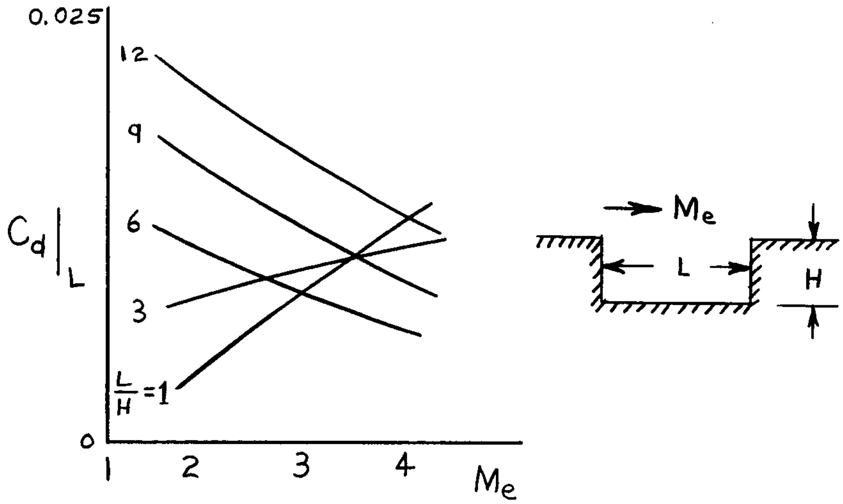

Diagram 5. Notch Drag Coefficients (Reference 9)

this type of deflection could be approximated by the flow over a double wedge. Using this approximation and linearized supersonic flow theory the drag coefficient C_d was found to be proportional to Δ^2/M_e, where Δ is the deflection angle of the external stream into the notch. The deflection angle Δ, for the range of notch lengths and depths tested here, was approximately proportional to $L/L_{critical}$ for the notch. L being the notch length and $L_{critical}$ the notch length at which the external stream just reattaches to the floor of the notch. The results shown in Diagram 5 for long notches, where the notch length was less than the critical length ($\frac{L}{H}$ = 6, 9, 12), are in approximate qualitative agreement with Charwat's proposal.

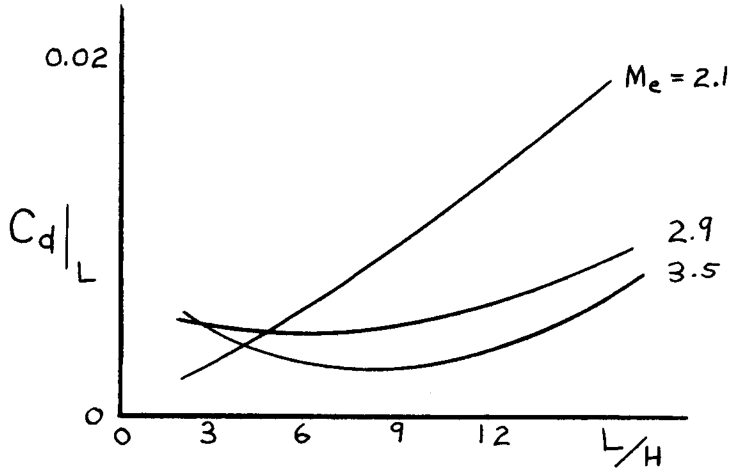

Diagram 6. Notch Drag Coefficients (Reference 9)

Diagram 6 is simply a cross plot of the data presented in Diagram 5 so as to demonstrate the effect of notch length on the drag coefficient for a constant free stream Mach number. These results were useful for estimating the order of magnitude of the drag force coefficient of v-shaped notches. Also, in general, the same trends in the variation of the drag force coefficients were observed for the v-shaped notches as were reported for rectangular cutouts. It is also interesting to note at this point that the trend of the notch drag coefficient curve for a Mach number equal to 2.1 (Diagram 6) is similar to the reported variation of C_d for subsonic flows shown in Diagram 4.

The above mentioned limited number of investigations can be considered as representative of the work done in this area. A more complete list of references can be found in an extensive bibliography given by Wuerer and Clayton (Reference 52).

B. Flow Components

In the following chapter of this investigation a flow model is devised by combining several types of flow components into a single flow model for a v-shaped notch. This flow model is illustrated in Figure 1. The preference for a flow model composed of rather well defined component flows (despite their complex interactions) over more generalized and comprehensive analytical models dealing almost entirely with integral quantities (References 32 and 53) is obviously dictated by the need for increased insight into the flow mechanisms. Investigation of the literature indicated that many analyses of these various flow components have been made and examples of these are described in the following paragraphs. The flow components which were considered are:

i. expansion of the external flow field and adjacent shear layer around a corner

ii. flow at a compression corner

iii. developing free shear layer.

Anandamurthy and Hammit (Reference 1) investigated in detail the interaction of expansion waves with a two-dimensional supersonic boundary layer. They made measurements on expansion angles of 5° to 30° with an approach

Mach number of 1.88 and an approach turbulent boundary layer thickness of 0.17 inch with a stagnation pressure of 105 psia. Their results showed that the static pressure which was exerted by the external flow field on the shear layer downstream from the corner approached the value predicted by the inviscid Prandtl-Meyer expansion flow about ten boundary layer thicknesses downstream from the corner.

White (Reference 50) investigated turbulent boundary layer separation from smooth-convex surfaces in supersonic two-dimensional flow and found that the static pressure of the external stream in expanding around a smooth (4 inch radius of curvature) corner was almost identical to that predicted by Prandtl-Meyer flow. He also reported the results of a theoretical calculation based on a method presented in Reference 25 for the development of the momentum thickness of the shear layer as it expanded around a smooth corner. Reported experimental values agreed very well with his predicted results.

Chuan (Reference 10) proposed a flow model using the Crocco-Lees mixing theory (Reference 13) in order to predict the flow field in the vicinity of a compression corner. Chuan reported that an important characteristic in the flow phenomenon was the entrainment of mass from the free stream into the viscous mixing region near the corner. He determined experimentally a mixing rate parameter for turbulent flow at a Reynolds number of 6×10^5 per inch and a Mach number of 2.54.

Erdos and Pallone (Reference 19) investigated the problem of viscous flow at a compression corner. They developed a simple model which used the essential physical features of the interaction between the external stream and the viscous shear layer. A solution was developed for the surface pressure distribution and the inviscid flow deflection and also a correlation formula was developed for determining the location of the separation and reattachment points.

Another method for analyzing viscous corner flow was proposed by Bloom and Rubin (Reference 3) in which they used a boundary layer integral method for compressible symmetric corner flow. Their method extended the constant density corner flow solution to the compressible flow case. Their proposed method was for the laminar boundary layer case but it could be adapted to turbulent flows.

Drougge (Reference 18) experimentally investigated separation of a turbulent boundary layer at a concave corner for a Mach number of 1.8 and 2.75. His main conclusion was that for a constant Mach number and a fully turbulent boundary layer the value of the ratio of separation length to boundary layer thickness was independent of Reynolds number. He also concluded that the pressure coefficient through the shock wave was the relevant parameter for the prediction of separation and for the prediction of the length of the separation distance.

Another investigation pertinent to the separation inside of the v-notch was that by Mager (Reference 34). Mager developed a model which is capable of determining the separation from a flat surface for a "free-interaction." By "free-interaction" it is meant that the flow field downstream of the separation point is free to adjust to any direction which results from the shock-boundary layer interaction. This method is capable of predicting the pressure rise due to separation.

For the developing free shear layer in the separated flow region several methods have been proposed to describe the mixing region. One of these methods was that proposed by A. J. Chapman (Reference 7). Chapman proposed a solution for the mixing characteristics of an incompressible free jet which included the effects of the initial shear layer configuration on the mixing region. The concept of a position parameter, η_P , which was a function of the dimensionless length Ψ of the developing shear layer was introduced in his solution. This method was developed further for the compressible flow case by Korst, et al. (Reference 26). The analysis was made for turbulent constant pressure mixing along a compressible free jet boundary and it also included the effects of the initial shear layer on the mixing region. This solution contained the same position parameter η_P as did Chapman's solution. Korst, et al., presented the asymptotic solution, $\eta_P \rightarrow 0$, corresponding to a fully developed mixing profile along the free jet boundary. Auxiliary functions pertaining to the kinematic, dynamic, dissipative, and thermodynamic characteristics of flow fields having fully established ($\eta_p \rightarrow 0$) similarity profiles were derived and tabulated values for these functions have been presented (Reference 28).

Carrière and Sirieix (Reference 6) suggested that for small values of η_p a lateral shift of the fully developed velocity profiles in the mixing region would be adequate to account for the effect of the initial shear layer. This concept, called equivalent bleed, was substantiated by Golik (Reference 20).

A recent analysis in the treatment of compressible developing free shear layers was made by Lamb (Reference 31). He analyzed theoretically the development of a two-dimensional free turbulent shear layer from an arbitrary initial power law velocity profile. The mean flow in the development region was represented by approximate velocity profiles which contained the position parameter η_p. Lamb obtained a relationship between η_p and the development length Ψ by applying the Navier-Stokes equations to the dividing streamline which separated the primary and secondary flow fields.

Another method of analysis which was investigated for the developing free shear layer component was that proposed by Steiger and Bloom (Reference 46) in which sets of similar solutions were derived for two-dimensional compressible free shear layers with initial velocity profiles that had a small velocity defect in comparison to the external velocity.

Wuerer and Clayton (Reference 52) presented a recent review of separated flow phenomena and methods of analyses in the area of separation and reattachment at high speeds. Other references were consulted for this analysis of flow components but they were not found relevant to the present discussion. Some of these will however be referred to where appropriate in later discussions.

C. Surface Skin Friction

The need for measuring drag forces directly was stated in Chapter I and a drag balance was consequently constructed. In order to establish the accuracy of the drag balance two methods of calibration were utilized, static, by weight forces, and dynamic, by fluid forces measured in the wind tunnel. The static calibration used an arrangement of pulleys mounted on instrument bearings and strings with weights to apply static loads to the balance to represent drag forces. The dynamic calibration consisted of the measurement of the drag force on a flat plate mounted in the balance and tested with supersonic external flow. These measured drag forces were then compared with measured forces reported in the literature. Published experimental values for the skin friction coefficient on a flat plate were given by Hakkinen (Reference 21), Jackson, Czarnecki, and Monta (Reference 23), Peterson (Reference 39), and Wilson (Reference 51) for compressible turbulent boundary layers in transonic and supersonic flow. Schlichting (Reference 42) and Sommer and Short (Reference 44) also presented data on skin friction coefficients and methods of measurement. The actual skin friction values that were used for comparison came from References 23 and 39.

In order to compare the skin friction data obtained with the drag balance to that available in the literature the boundary layer approaching the flat plate model had to be clearly defined in the same terms as utilized in the published results. The boundary layer characteristics corresponding to the published skin friction coefficients were used to define the approaching shear layer. The characteristics that were used included the exponent of the power law velocity profile, the momentum thickness, and the boundary layer shape parameter.

III. PROBLEM ANALYSIS

A flow model has been devised which is made up of the different flow components discussed in Chapter II. The concept of the model was derived from experimental observations of the flow over v-shaped notches, and the components were so chosen that simple interactions between them could be treated.

A. Basic Flow Model

A preliminary experimental study of the flow over v-shaped notches was conducted in the supersonic and transonic flow regimes. This investigation consisted of taking Schlieren photographs for various notch configurations along with measuring static pressure distributions in the notch. A representative sample of these Schlieren photographs is shown in Figures 2, 3, 4, and 5. Using these photographs and the static pressure measurements the general flow picture can be defined as shown in Figure 1, which depicts a v-shaped notch with an angle $\Omega = 10^{\circ}$. While the flow configuration depicted in Figure 1 was typical in a qualitative sense for a wide range of notch geometries and flow conditions, certain systematic changes can be pointed out which result from changes in the notch geometry and external flow conditions. The four basic variables in this problem are free stream Mach number, notch angle, Reynolds number, and the ratio of the approach boundary layer momentum thickness to the notch length. The effect on the flow model resulting from a change in these variables will now be systematically discussed.

Schlieren photographs of flow over a v-notch for constant approaching external free stream Mach numbers are shown in Figures 2 and 4. Figure 2 contains a series of photographs of flow at a Mach number of two over a two inch long v-shaped notch with different notch angles. Figure 4 contains Schlieren photographs of flow at a Mach number of 1.14 over two inch long notches with each photograph showing a different angle v-notch. As the notch angle ♌ was increased from the value depicted in Figure 1 of 10°, while the value of θ/L and Re_x remained approximately constant, the separation point S moved upstream and the reattachment point R moved downstream. As the notch angle was decreased the opposite effect was observed, the separation point moved downstream and the reattachment point moved upstream. For the approaching flow conditions used in this investigation the separation point S was almost at the leading edge of the notch when the notch angle was greater than 16°, however, the separation point never did move completely down to the vertex of the notch, even when the notch angle was reduced to 7°.

The effect of a systematic change in the Mach number, particularly in the transonic regime with θ/L, Re_x, and notch angle constant is depicted in Figures 3 and 5. These Schlieren photographs clearly indicate that the separation point shifts as the Mach number is changed. The separation point was nearest the leading edge of the notch near a Mach number equal to one while for larger or smaller Mach numbers the separation point moved further downstream. The development of the shock wave and expansion wave structure for a v-notch is clearly visible in Figure 5 for an increase through M = 1 while the effect of a change in notch angle on the shock wave-expansion structure is shown in Figure 4.

The effect on the flow configuration when θ/L was changed while maintaining a constant Mach number, Re_x, and notch angle was not noticeable for the relatively small range of values of θ/L. Schlieren photographs were taken of the flow structure over four inch long notches at a Mach number of two and the flow structures were identical to those shown in Figure 2 even though θ/L was smaller by a factor of one-half. The expected change in the flow structure as θ/L is decreased would be that the separation region decreases in length so that the inviscid flow configuration would be approached, at least for small angles. However, if θ/L is increased the flow configuration would change more drastically. The anticipated type of change would be such that as θ/L is increased the shock-expansion structure would become weaker and the relatively thick boundary layer would bury the notch in a low velocity flow field. For very high values of

θ/L the external stream would not be strongly affected by the notch and the shear layer component would only exhibit a slight thickening.

The basic flow model shown in Figure 1 depicts various flow components which were discussed in Chapter II. The relationship of these components to the over-all flow model and to each other is pointed out in the following paragraphs.

i. Between sections (1) and (2) the boundary layer and external flow field expand around the initial corner of the notch. Analyses of this flow component were presented by Anandamurthy and Hammit (Reference 1) and by White (Reference 50) who utilized a streamtube expansion concept and a simplified differential equation for shear profile integrals.

ii. Between sections (2) and (3) the expanded shear layer develops along the surface and this can be analyzed using boundary layer integral techniques.

iii. From section (3) to section (4) the shear layer separates from the surface while the external flow changes direction, causing the separation shock. Analysis of this component might be accomplished by methods proposed in References 8, 13 and 34.

iv. The region between sections (4) and (5) consists of a developing free shear layer. Several methods of analysis were discussed in Chapter II but the one chosen as best suited for this investigation was the one proposed by Lamb (Reference 31). The other methods discussed in Chapter II (References 46, 27, 6 and 20) were found not applicable for reasons particular to the individual methods. There is some concern as to whether Lamb's method will be adequate for this component since the free shear layer is in such close proximity to the wall. Lamb's method is based on the assumption of a quiescent wake, hence neglects effects of wall interference.

v. Between sections (5) and (6) the flow reattaches to the surface while the external flow changes direction resulting in a reattachment shock. Several analyses of this component have been made and a critical discussion of these methods is presented by White (Reference 50).

vi. From section (6) to section (7) the reattached shear layer begins to redevelop along the surface and boundary layer integral methods can be used to analyze the flow mechanism.

vii. The reattached shear layer and external flow field expand around the final corner of the notch between sections (7) and (8). This region is similar to that described in i), except that the approach shear layer is in the process of redevelopment after reattachment.

viii. Downstream of section (8) the shear layer undergoes further redevelopment along the flat surface.

The often unsatisfactory status of knowledge concerning the isolated flow components will be compounded by the complexity introduced through their internal interactions. On the other side, the delineation of the over-all model into components identifies such regions where the usual boundary layer assumptions are reasonably well satisfied [from section (2) to section (3); from section (6) to section (7); and after section (8)] and others which require special attention [such as section (1) to section (2); section (3) to section (4); section (5) to section (6); and section (7) to section (8)]. Alternate methods of solving flow problems involving separation and reattachment based entirely on boundary layer concepts [Lees and Reeves (Reference 32); Holden (Reference 53)] can be subjected to criticism arising from the questionable validity of the basic boundary layer assumptions near separation and reattachment points.

B. Basic Flow Interactions

In Part A above the basic flow model was defined and the various components of the model, (i) through (viii), were discussed. From the general remarks made there it is apparent that an exact analytical solution to the over-all problem of viscous flow over a v-shaped notch is not available at the present time. If the problem were simply to consider the separate components (i) through (viii) above and apply these results to solve analytically for the entire flow field a solution would be possible. However, in the present problem, the various components are strongly coupled making an analytical solution unfeasible.

For the range of flow variables considered in this investigation and the geometrical configurations used, the interactions of the various components are the important factors in determining the flow field. Since these interactions are the notable factors in the description of the flow field the investigation of flow over a v-notch was divided into studies of the influence of geometry changes and flow condition changes on these interactions which in turn effected the drag force characteristics of the v-notch.

C. Direct Measurement of Drag Forces

The difficulties encountered in trying to formulate an exact solution to the notch flow problem implied that direct measurement was the only reliable means of determining the drag force. Since it can be shown that the drag determination from flow profile measurements based on momentum principles cannot be expected to produce accurate results, a direct measuring force balance was designed and constructed. The description of this balance is given in

Chapter IV. When a new instrument, such as this drag force balance is built, it is necessary to test it for reliability and accuracy. The model used in testing for accuracy was the flat plate. There were several reasons for choosing the flat plate as a test case. First of all, theoretical analyses are available for predicting the drag forces acting on the plate, and one analysis is presented below. Second, there were available experimental data for the drag forces and these were used as comparisons with the drag forces obtained from the new balance.

D. Theoretical Analysis for Turbulent Flow over a Finite Length Flat Plate

The boundary layer analysis used here was based on the approach used by Truckenbrodt (Reference 48) for incompressible turbulent boundary layer flow with streamwise pressure gradient as adapted for the compressible flow case by use of the Culick-Hill transformation presented in Reference 14.

Truckenbrodt found two quadrature formulas for the characteristic parameters of boundary layer flow, momentum loss thickness θ and the velocity profile form parameter H. Truckenbrodt's assumptions limited the results to the two-dimensional flow case. The calculation of the momentum loss thickness was done by integration of the energy theorem while the equation for the velocity form parameter was obtained by coupling the momentum and the energy equations. Truckenbrodt's result for the momentum thickness for incompressible flow was

$$\theta_i(x) = \frac{\nu_o^{\frac{1}{1+N}}}{u_{e_i}^3} \left[\left(\frac{u_{e_1}\theta_1}{\nu_o} \right)^{1/N} \theta_1 u_{e_1}^{3+\frac{2}{N}} + A \int_{x_1}^{x} u_e^{3+\frac{2}{N}} \, dx \right]_i^{\frac{N}{N+1}} \tag{1}$$

where

$$A = \frac{N+1}{N} \alpha(N) \tag{2}$$

with the empirical values of N and $\alpha(N)$ given in Table 1.

Table 1. Values of N and $\alpha(N)$ (Reference 14)

$(Re_\theta)_i$	N	$\alpha(N)$
100-5000	4	0.0123
500-50000	5	0.0085
3000-6 x 10^5	6	0.0062
10^4-10^7	7	0.0048

By use of equation (2) and algebraic rearrangement of equation (1) one obtains

$$\left[\theta(x)^{\frac{N+1}{N}} \frac{u_e}{\nu_o} \right]_i^{1/N} = \left(\frac{N+1}{N} \right) \alpha(N) \, u_{e_i}^{-(3+\frac{2}{N})} \int_{x_1}^{x} u_{e_i}^{3+\frac{2}{N}} \, dx_i + \theta_{i_1}^{\frac{N+1}{N}} \left(\frac{u_e}{\nu_o} \right)_{i_1}^{1/N} \left(\frac{u_{e_1}}{u_e} \right)_i^{3+\frac{2}{N}} . \tag{3}$$

Culick and Hill transformed equation (3) to the compressible plane by using an analog to the Stewartson-Illingworth transformation for laminar flow. It was shown in Reference 14 that the transformation was valid if the effect of compressibility on the boundary layer shape parameter H could be represented by

$$H + 1 = (H_i + 1)\left(\frac{T_o}{T_e}\right) \tag{4}$$

and if the x-coordinate transformation was chosen such that it was conveniently related to the ratio of skin friction coefficients in compressible and incompressible flows. These two conditions were verified for turbulent boundary layers up to a Mach number of 5. The Culick-Hill transformation can be specified for a gas with a specific heat ratio of 1.4 by the following three equations.

$$U_{e_i} = a_o M \tag{5}$$

$$\theta_i = \left(\frac{T_e}{T_o}\right)^3 \theta \tag{6}$$

$$X_i = \int \left(\frac{T_e}{T_o}\right)^{4 - 1/N} dX \tag{7}$$

Equation (3), transformed to the compressible case by applying the transformation equations (5), (6), and (7) yields,

$$\left[\theta\left(\frac{T_e}{T_o}\right)^3\right]^{\frac{N+1}{N}} = \left(\frac{N+1}{N}\right)\alpha(N)\left(\frac{a_o}{\nu_o}\right)^{-1/N} M_e^{-\left(3+\frac{3}{N}\right)} \int_{x_1}^{x} M_e^{3+\frac{2}{N}}\left(\frac{T_e}{T_o}\right)^{4-\frac{1}{N}} dx + \left[\theta\left(\frac{T_e}{T_o}\right)^3\right]_1^{\frac{N+1}{N}}\left(\frac{M_e}{M}\right)_1^{3+\frac{3}{N}} . \qquad (8)$$

Equation (8) was applied to the special case of predicting the growth of the momentum thickness on a flat plate in compressible flow where the Mach number and the free stream temperature were independent of the x-position. This was done for two positions of x, x_1 and x_2. For x_1 equation (8) reduced to

$$\left[\theta(x_1)\right]^{\frac{N+1}{N}} = \left[\theta\left(\frac{T_e}{T_o}\right)^3\right]_1^{\frac{N+1}{N}}\left(\frac{M_{e_1}}{M_e}\right)^{3+\frac{3}{N}}\left(\frac{T_o}{T_e}\right)^{\frac{3(N+1)}{N}} . \qquad (9)$$

For x_2 equation (8) reduced to

$$\left[\theta(x_2)\right]^{\frac{N+1}{N}} = \left(\frac{N+1}{N}\right)\alpha(N)\left(\frac{a_o}{\nu_o}\right)^{-1/N} M_e^{-1/N}\left(\frac{T_e}{T_o}\right)^{4-\frac{1}{N}}(x_2-x_1)\left(\frac{T_o}{T_e}\right)^{\frac{3(N+1)}{N}} + \left[\theta\left(\frac{T_e}{T_o}\right)^3\right]_1^{\frac{N+1}{N}}\left(\frac{M_{e_1}T_o}{M_e T_e}\right)^{\frac{3(N+1)}{N}} . \qquad (10)$$

Now, taking the difference between equation (10) and equation (9) yielded

$$\theta(x_2)^{\frac{N+1}{N}} - \theta(x_1)^{\frac{N+1}{N}} = \frac{N+1}{N}\,\alpha(N)\left(\frac{a_o M_e}{\nu_o}\right)^{-1/N}\left(\frac{T_e}{T_o}\right)^{\frac{N-4}{N}}(x_2 - x_1)\ . \tag{11}$$

Equation (11) is an expression for the difference in the momentum thickness along a flat plate in compressible flow for a finite length, $x_2 - x_1$. Now, in order to adapt this equation for the special case which exists in the drag balance, namely, a small but finite length of flat surface, $\Delta\theta$ can be conveniently expressed as follows:

$$\Delta\theta = \theta(x_2) - \theta(x_1) \tag{12}$$

and $\theta(x_2)$ can be expressed as

$$\theta(x_2)^{\frac{N+1}{N}} = \left[\theta(x_1) + \Delta\theta\right]^{\frac{N+1}{N}}\ . \tag{13}$$

The quantity $\Delta\theta$ can be expressed in a closed solution if the binomial theorem is used to expand $\theta(x_2)$ to the power $(N + 1)/N$ shown in equation (13) , the result of which is given by equation (14).

$$\theta(x_2)^{\frac{N+1}{N}} = \theta(x_1)^{\frac{N+1}{N}} + \left(\frac{N+1}{N}\right)\theta(x_1)^{1/N}\Delta\theta + \left(\frac{N+1}{2N^2}\right)\theta(x_1)^{\frac{1-N}{N}}(\Delta\theta)^2 + \mathcal{R}em. \tag{14}$$

If the remainder term $\mathcal{R}em$ is neglected one obtains

$$\theta(x_2)^{\frac{N+1}{N}} - \theta(x_1)^{\frac{N+1}{N}} = \left(\frac{N+1}{N}\right)\left[\theta(x_1)^{1/N}\Delta\theta + \frac{1}{2N}\theta(x_1)^{\frac{1-N}{N}}(\Delta\theta)^2\right] \tag{15}$$

as a second-order approximation for $\theta(x_2)$ in terms of $\Delta\theta$.

Substituting the result from equation (15) into equation (11) yields

$$\theta(x_1)^{1/N}\Delta\theta + \frac{1}{2N}\,\theta(x_1)^{\frac{1-N}{N}}(\Delta\theta)^2 = \alpha(N)\left(\frac{a_0 M_e}{\nu_0}\right)^{-1/N}\left(\frac{T_e}{T_0}\right)^{\frac{N-4}{N}}(x_2 - x_1)$$

or rearranging

$$\Delta\theta = N\theta(x_1)\left[\theta(x_1)^{-1/N}\sqrt{\theta(x_1)^{2/N} + \frac{2}{N}\theta(x_1)^{\frac{1-N}{N}}\alpha(N)\left(\frac{a_0 M_e}{\nu_0}\right)^{-1/N}\left(\frac{T_e}{T_0}\right)^{\frac{N-4}{N}}(x_2 - x_1)} - 1\right]. \tag{16}$$

The momentum equation can now be used to express the drag force on a flat plate as a function of the momentum thickness. The control surface is shown in Diagram 7 for compressible flow.

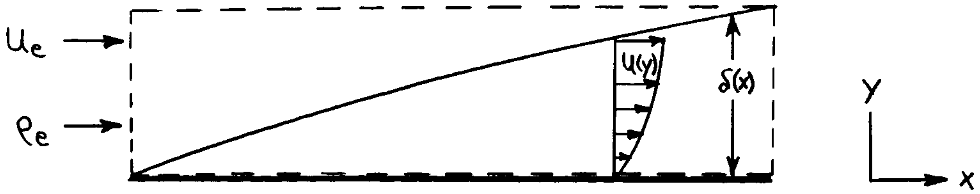

Diagram 7. Flat Plate Drag Force

Applying the momentum equation to the control volume shown in Diagram 7 for a width b, yielded

$$\frac{D}{b} = \int_0^{\delta(x)} \rho_e u_e^2 \, dy - \int_0^{\delta(x)} \rho u^2 \, dy - u_e \int_0^{\delta(x)} (\rho_e u_e - \rho u) \, dy$$

or rearranging

$$\frac{D}{b} = \int_0^{\delta(x)} (\rho u u_e - \rho u^2) \, dy \quad . \tag{17}$$

Equation (17) was rearranged to the following form

$$D = b \rho_e u_e^2 \int_0^{\delta(x)} \frac{\rho u}{\rho_e u_e} \left(1 - \frac{u}{u_e}\right) dy$$

or

$$D = b \rho_e u_e^2 \; \theta(x) \tag{18}$$

where $\theta(x)$ is by definition,

$$\theta(x) \equiv \int_0^{\delta(x)} \frac{\rho u}{\rho_e u_e} \left(1 - \frac{u}{u_e}\right) dy \; . \tag{19}$$

Now, from the above it is seen that the drag on a plate of length x_2 is

$$D_2 = b \, \rho_e \, u_e^2 \, \theta(x_2) \tag{20}$$

and of length x_1 is

$$D_1 = b \, \rho_e \, u_e^2 \, \theta(x_1) \; . \tag{21}$$

The drag force on the plate between x_1 and x_2 is the difference of the two equations, (21) and (20),

$$F = D_2 - D_1 = \rho_e \, u_e^2 \, b \; \left[\theta(x_2) - \theta(x_1)\right] = \rho_e u_e^2 \, b \, \Delta\theta \tag{22}$$

Solving for $\Delta\theta$ from equation (22) gives

$$\Delta\theta = \frac{F}{\rho_e \, u_e^2 \, b}$$

and now defining $\bar{C}_f$ and using equation (16) yields

$$\bar{C}_f = \frac{F}{\frac{1}{2} \rho_e \, u_e^2 \, b \, (x_2 - x_1)} = \frac{2 N \theta(x_1)}{(x_2 - x_1)} \times$$

$$\left[\theta(x_1)^{-1/N} \sqrt{\theta(x_1)^{2/N} + \frac{2}{N} \, \theta(x_1)^{\frac{1-N}{N}} \alpha(N) \left(\frac{a_0 M_e}{\nu_0}\right)^{-1/N} \left(\frac{T_e}{T_0}\right)^{\frac{N-4}{4}} (x_2 - x_1)} \quad - 1 \right] . \tag{23}$$

A power law expression for the temperature-viscosity relation,

$$\frac{\mu}{\mu_o} = \left(\frac{T}{T_o}\right)^{\beta}$$

along with the ideal gas relation and isentropic process for density change with temperature change,

$$\frac{\rho_e}{\rho_o} = \left(\frac{T_e}{T_o}\right)^{\frac{1}{K-1}}$$

and the isentropic speed of sound relation with temperature

$$\frac{a_o}{a_e} = \sqrt{\frac{T_o}{T_e}}$$

were used to simplify equation (23) to the final result given in equation (24)

$$\overline{C_f} = \frac{2N\,\theta(x_1)}{(X_2 - X_1)} \left[\sqrt{1 + \frac{2\,\alpha(N)}{N\,\theta(x_1)} \left(Re_{\theta_1}\right)^{-1/N} (X_2 - X_1) \left(\frac{T_e}{T_o}\right)^{\frac{N-\beta-1}{N}}} - 1 \right] \tag{24}$$

where

$$Re_{\theta_1} = \frac{u_e\,\theta_1\,\rho_e}{\mu_e} \quad .$$

Three distinct drag coefficients related to the shear stress or drag force on a flat surface may now be distinguished. The local friction coefficient, C_f, is defined as the local shear stress at the surface divided by $\frac{1}{2}\,\rho_e\,u_e^2$. The total shear stress coefficient, C_F, is defined as the total shear force acting on the plate from the beginning of the plate to the length L, divided by $\frac{1}{2} \rho_e u_e^2 bL$. The average drag force coefficient $\overline{C}_f$, defined by equations (23) and (24), is an approximate theoretical representation for the shear force on the finite length of flat surface divided by $\frac{1}{2} \rho_e u_e^2 b(x_2 - x_1)$. This approximate coefficient for a finite length flat plate was used as a comparison for the experimental data.

E. Drag Force Analysis for the V-Notch

1. Drag Coefficient for V-Shaped Notches

In Part D several drag coefficients applicable to uniform flow past a flat surface were defined and discussed. These included the local skin friction coefficient C_f, the total shear stress coefficient C_F and the average coefficient $\overline{C}_f$ all of which use the wetted surface of the plate as a reference area. The drag coefficient for a notch or groove is usually defined in one of two ways, depending on the selection of a reference area. The most common definition which utilizes an area equal to the length times the width of the notch, the projected area on the plane surface, will be used as the definition of the drag coefficient and is given by equation (25).

$$C_d = \frac{D}{\frac{1}{2}\rho_e u_e^2\, b\, L} \tag{25}$$

This is also a most convenient definition for the present case since the flat plate can be considered to be a v-notch with vanishing angle Ω.

2. Form Drag and Friction Drag

The drag force can be thought of as having two parts, drag due to shear forces and drag due to normal forces. The more common names are drag due to friction and pressure drag. The term pressure drag or form drag, is commonly used for subsonic flow, while the term wave drag is used in supersonic flow. In many gas dynamic problems involving drag forces the pressure or wave drag may be five to ten times greater than the friction drag. For typical airfoils in transonic and supersonic flow the order of magnitude for the friction drag coefficient is about 0.005 while the total drag coefficient might be of the order of 0.02 to 0.08.

The form drag or wave drag is determined, within certain limitations arising from viscous interactions, by the geometry of the walls. The situation may change considerably however, when there is a region of separated flow such as exists in a v-shaped notch. For this case the separation causes the pressure or wave drag to be strongly modified as a consequence of the actual flow geometry being at variance with wall boundary conditions. This is borne out by Figure 6 where three different static pressure distributions are shown:

i. the theoretical wall pressure distribution for a supersonic flow (in absence of separation) due to Prandtl-Meyer expansions and a shock located at the vertex of the v-notch,

ii. the theoretical shock-expansion pressure distribution consistent with the flow model shown in Figure 1,

iii. experimental values obtained for the 10° v-shaped notch.

As noted before the measured pressure distribution differs greatly from curve i). As a consequence of separation the pressure increase at the center of the notch is eased by the interaction between the free stream with shear flow regions. Consequently, it can be recognized that the form or wave drag is not directly related to the wall geometry, but rather to the flow geometry as affected by separation. In comparing ii) to iii) it is also seen that the viscous layers by themselves are of major interest and also introduce an important modifying element to the theoretical shock-expansion model.

An important parameter which must be considered as influencing the two components of drag is the boundary layer thickness relative to the notch length. For many of the classical gas dynamic solutions to the drag problem, such as airfoil drag, the existence of a boundary layer was of only minor importance. However, in the problem being analyzed here, the boundary layer presence is an important factor. The qualitative effect of the boundary layer when it is of significant thickness in comparison to the length of the notch is to reduce the drag force. For boundary layers that are thick relative to the notch dimension the notch is buried under the shear layer. The limiting case for this situation would be when the notch appears only as a surface imperfection for very thick boundary layers ($\delta/L \rightarrow \infty$).

3. Phenomenological Flow Models

The most significant difference between the inviscid and the actual flow configuration was recognized to be in the deviation of the streamlines from the geometry introduced by the solid walls. Consequently, the wave drag is no longer exclusively determined by the wall geometry, but instead, by the separating and reattaching free shear layer. Because of this occurrence an attempt was made to examine the over-all drag force on the basis of a simplified, phenomenologically conceived model comprising the wave drag of the actual (separated) streamline configuration and those shear stresses contributed by the mixing shear layer. This concept should be reasonably correct as long as the shear force due to the attached boundary layers between sections (2) and (3) and between sections (6) and (7) in Figure 1 remain small as compared to the form drag of the wall portions, which will not be the case for very shallow notches with vanishing separation regions. Such a model is shown schematically in Diagram 8.

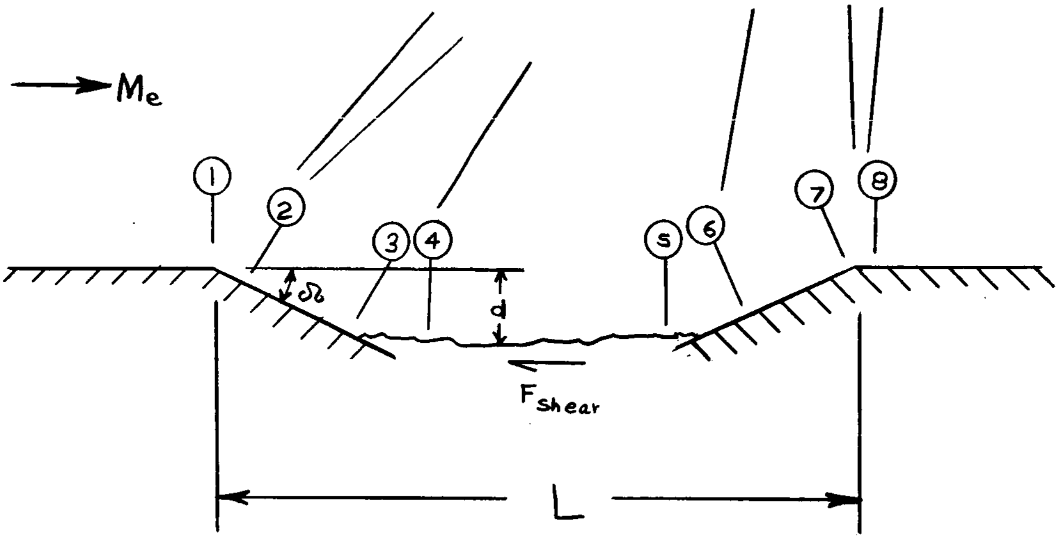

Diagram 8. Proposed Drag Force Model

It should be noted that the exact locations of either the separation point or the reattachment point are generally not known nor can they be determined presently by entirely analytical methods. However, for the present purpose it can be assumed that the separation streamline remains practically parallel to the external flow such that a single geometrical parameter, namely the penetration depth ratio d/r, fully describes the flow geometry of the model. Since d/r is strongly dependent upon the already established parameters controlling the problem it will be treated as an undetermined quantity in the following theoretical analysis.

a) Shock-Expansion Theory

Shock-expansion theory can be utilized and applied to both supersonic flow past notches (without further restrictions) and transonic flow past notches (with the further restriction that the Mach numbers encountered within any flow region of the model exceed unity).

The wave drag of the actual configuration can be calculated using the Prandtl-Meyer expansion relation (Reference 43) between sections (1) and (2) and the plane shock relations (Reference 15) between sections (3) and (4) and sections (5) and (6). The Prandtl-Meyer function, PM(M,k), given by equation (26),

$$PM(M,k) = \sqrt{\frac{k+1}{k-1}}\tan^{-1}\sqrt{\frac{k-1}{k+1}(M^2-1)} - \tan^{-1}\sqrt{M^2-1} \qquad (26)$$

is related to the notch angle by

$$PM(M_2,k) = PM(M_1,k) + \Omega \qquad (27)$$

and the pressure change through the expansion is isentropic and is given by

$$\frac{P_{o2}}{P_2} = \left(1 + \frac{k-1}{2} M_2^2\right)^{\frac{k}{k-1}} . \tag{28}$$

The assumptions,

$$\begin{aligned} P_{o1} &= P_{o2} = P_{o3}, \\ M_2 &= M_3 , \\ P_2 &= P_3 , \\ P_4 &= P_5 , \\ P_{o4} &= P_{o5} , \\ \text{and} \qquad M_4 &= M_5 \end{aligned} \tag{29}$$

are made and appear to be reasonable for this analysis. The plane shock relations are as follows:

$$\tan \Omega = 2 \operatorname{Cot} \theta_{wave} \frac{M_x^2 \sin^2 \theta_{wave} - 1}{M_x^2 (k + \operatorname{Cos} 2\theta_{wave}) + 2} \tag{30}$$

$$M_y^2 \sin^2(\theta_{wave} - \Omega) = \frac{1 + \frac{k-1}{2} M_x^2 \sin^2 \theta_{wave}}{k M_x^2 \sin^2 \theta_{wave} - \frac{k-1}{2}} \tag{31}$$

$$\frac{P_y - P_x}{P_x} = \frac{2k}{k+1} \left(M_x^2 \sin^2 \theta_{wave} - 1 \right) \tag{32}$$

$$\left(\frac{P_{oy}}{P_{ox}}\right)^{K-1} = \frac{1}{\left(\frac{K-1}{K+1} + \frac{2}{(K+1)\, M_x^2 \sin^2\theta_{wave}}\right)^{K} \left(\frac{2K}{K+1} M_x^2 \sin^2\theta_{wave} - \frac{K-1}{K+1}\right)} \tag{33}$$

where θ_{wave} is the wave angle and the subscripts x and y denote the upstream and downstream sides of the shock wave respectively.

With the above relationships the pressure at the various sections can be calculated and utilized in calculating the wave drag force. The drag force due to the shear forces in the mixing region is calculated by the method presented in the following section.

b) Linearized Supersonic Theory

For the restrictions that the Mach number is greater than unity (but not close to unity) and less than ten, linearized supersonic theory can be used to calculate the wave drag in the model. This calculation is an alternative to the shock-expansion method presented in the preceding section. For the actual configuration shown in Diagram 8 the drag force due to wave drag is given by (Reference 43)

$$D_{wave} = \frac{1}{2} \rho_e u_e^2 b L \left(\frac{4}{\sqrt{M_e^2 - 1}}\right)\left(\frac{d}{L}\right) \tan(\Omega) \,. \tag{34}$$

The advantage of using linearized theory is that this relatively simple expression (equation 34) is found for the wave drag rather than the complex system of equations needed in the shock-expansion method.

The drag force contribution of the separated shear layer is treated utilizing the method presented by Lamb (Reference 31). Lamb analyzed theoretically the development of a two-dimensional free turbulent shear layer from an arbitrary initial velocity profile. The theoretical model for the developing free shear layer is shown in Diagram 9.

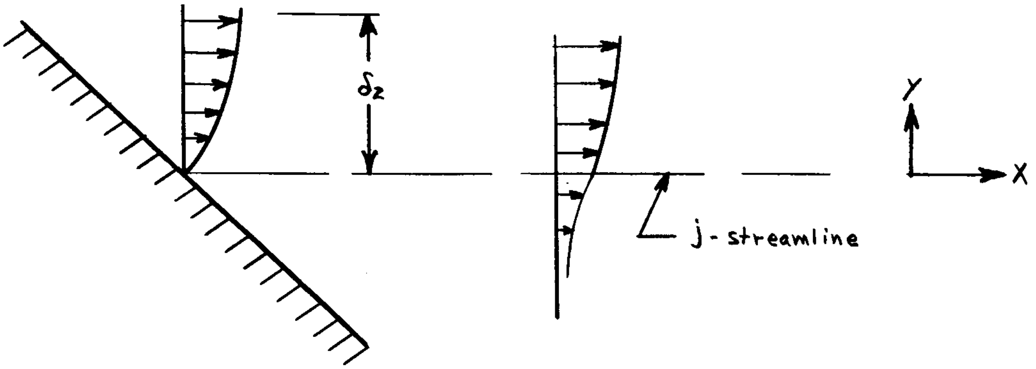

Diagram 9. Model for Developing Free Shear Layer

The drag force along the dividing streamline is given by

$$D_{Mixing} = b \int_0^x \tau_j \, dx \quad . \tag{35}$$

Equation (35) can be rearranged to

$$D_{\text{Mixing}} = \rho_e u_e^2 (1 - C_e^2) \delta_2 b \int_0^{\psi} J_j \, d\psi \tag{36}$$

where

$$\psi = \frac{x}{\delta_2}$$

and

$$J_j = \frac{\tau_j}{\rho_e u_e^2 (1 - C_e^2)} \quad . \tag{37}$$

Lamb shows that J_j is related to the integral $I_{j\eta_p}$ by

$$J_j = \frac{d}{d\psi}\left(\frac{I_{j\eta_p}}{\eta}\right) \quad . \tag{38}$$

Separating the variables in equation (38) and then integrating yields

$$I_{j\eta_p} = \eta_p \int_0^{\psi} J_j \, d\psi \quad . \tag{39}$$

η_p is called the position parameter and is equal to $\frac{1}{2}\sqrt{\xi}$ where $\xi = \frac{1}{2\sigma^2} \int_0^{\psi} \psi f(\psi) d\psi$. The relationship between η_p and ψ was obtained by Lamb by applying the Navier-Stokes equations to the dividing streamline. The integral $I_{j\eta_p}$ for the isoenergetic case is

$$I_{j\eta_p} = \int_{-\infty}^{\eta_j} \frac{\phi^2}{1 - C_e^2 \phi_2} \, d\eta \tag{40}$$

where $\eta = \frac{y}{\delta_2} \eta_p$ and $\phi = \frac{u}{u_e} = \phi(\phi_2, \eta, \eta_p)$ where ϕ_2 is the initial velocity profile at separation. Substituting from equation (39) into equation (36) yielded

$$D_{Mixing} = \rho_e u_e^2 \, b \left(1 - C_e^2\right) \frac{\delta_2}{\eta_p} I_{j\eta_p} \, . \tag{41}$$

Adding D_{wave} and D_{mixing} and substituting this quantity into the expression for the notch drag coefficient [equation (25)] yields

$$C_d = \frac{2r}{L}\left[\frac{4}{\sqrt{M_e^2 - 1}}\left(\frac{d}{L}\right) + \left(1 - C_e^2\right)\frac{I_{j\eta_p}}{\eta_p}\left(\frac{\delta_2}{L}\right)\left(\frac{1 - \frac{d}{r}}{1 - \frac{d}{L}}\right)\right] \tag{42}$$

Equation (42) was evaluated for various values of r/L and for representative values of δ_2 and C_e. The values of $I_{j\eta_p}$ were calculated using the IBM 7094 digital computer operated by the Department of Computer Sciences at the University of Illinois. The results of the calculations will be discussed in Chapter VI.

c) Transonic Drag Force Theory

A simplified model for the analysis of the drag force of a v-notch can be constructed for the transonic flow regime (but with M_e greater than unity) if several assumptions are made. First, it is assumed that the notch angle is small (less than 10°) so that there is little if any separated flow near the vertex of the notch. Secondly, it is assumed that wall shear drag (and mixing shear drag if present) is small as compared to wave drag. The flow model, which consists of a two-dimensional symmetrical v-shaped notch with an inviscid flow approaching the notch, is shown in Diagram 10.

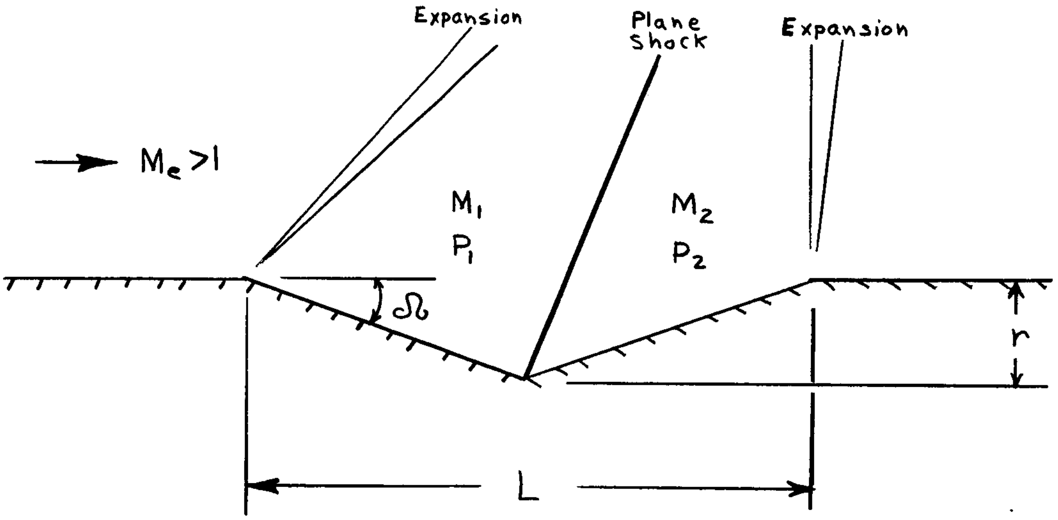

Diagram 10. Transonic Flow Model

The concept of this flow model is more clearly demonstrated if the change in the flow field is considered as M_e is decreased from a supersonic value of approximately two to unity. The drag coefficient for the notch shown in Diagram 10 is

$$C_d = \frac{(P_2 - P_1)\, r\, b}{\frac{\rho_e}{2}\, u_e^2\, L\, b}$$

which can be rearranged to give the more convenient form

$$C_d = \frac{\left(\frac{P_2}{P_1} - 1\right)\left(\frac{P_1}{P_e}\right)\left(\frac{r}{L}\right)}{\frac{K}{2}\, M_e^2} \quad . \qquad (43)$$

i) Utilization of Shock-Expansion Theory

The quantities in equation (43) can be easily determined with the help of tabulated functions. The functions which relate the Mach numbers and pressures were discussed in Section E.3.a. The pressure and Mach number after the expansion around the initial corner of Ω degrees can be determined by using the Prandtl-Meyer relation (Reference 43). The Mach number and pressure after the compression due to the turning angle of 2Ω can be found by using the plane shock relations with the aid of the charts presented in Reference 15. These calculations have been made for a 7° v-notch and the results are plotted in Figure 7 for a Mach number range of 1.33 to 2.0. The drag coefficient is evaluated only down to a Mach number of 1.33 because at this value for M_e and $\Omega = 7^\circ$ the shock wave at the vertex of the notch is about to detach from the corner.

ii) Mach Freeze Concept for Low Supersonic Approach Mach Number

For the example considered here ($\Omega = 7^{\circ}$) when the approach Mach number is less than 1.33 the shock wave, which was assumed to be located at the vertex of the notch, must be detached from the vertex and located further upstream. This is exactly the phenomenon which can be observed in the photographs in Figure 3. In order to facilitate the calculation of the drag coefficient in the region $1.0 < M_e < 1.33$ for a seven degree notch, the Mach number freeze concept first proposed by Bryson (Reference 5) is used. The basis of this concept is that for free stream Mach numbers near one the local Mach number at a fixed location is approximately constant. When this concept is applied to this flow model the free stream Mach number, as far as the Mach freeze concept is concerned, is M_1 while the local Mach number is M_2. Then, assuming a constant Mach number M_2 after the shock wave for M_e corresponding to 1.33 and $M_1 = 1.575$, the pressure ratio $P_2/P_{stag.}$ has a constant value. This must mean then, that the shock wave detaches from the vertex of the notch and changes the angle which it makes with the flow direction so as to give a constant value of $P_2/P_{stag.}$ as M_e decreases from 1.33 to 1.0.

The drag coefficient calculated using the Mach freeze concept is also plotted in Figure 7 for $1 < M_e < 1.33$. The merits of this model and its relation to the real flow case will be discussed in Chapter VI.

iii) Transonic Similarity Relations

The correlation of drag coefficients in the transonic flow regime is generally done by utilizing the transonic similarity parameters, $\mathcal{K}$ and $\mathcal{J}$.

$$\mathcal{K} = \frac{M_e^2 - 1}{2\left(\frac{k+1}{2}\right) M_e^2 \left(\frac{r}{L}\right)} \tag{44}$$

$$\mathcal{J} = \frac{C_d \left(\frac{k+1}{2}\right)^{1/3}}{\left(\frac{r}{L}\right)^{5/3}} \tag{45}$$

The similarity parameters $\mathcal{K}$ and $\mathcal{J}$ are obtained from the transonic similarity law (Reference 43). This similarity law relates the flow patterns for affinely related profiles in flows of different free stream Mach numbers through the similarity parameter $\mathcal{K}$. The similarity parameter $\mathcal{J}$ relates the drag characteristics for affinely related airfoils. The general nature of the relationship between the functions is illustrated in Diagram 11.

The trends shown in Diagram 11 are for wedge shaped bodies and also for thin airfoil profiles (Reference 43). The experimental relationship between $\mathcal{K}$ and $\mathcal{J}$ for v-shaped notches has been determined and the function is similar to that shown in Diagram 11. This relationship is discussed in more detail in Chapter VI.

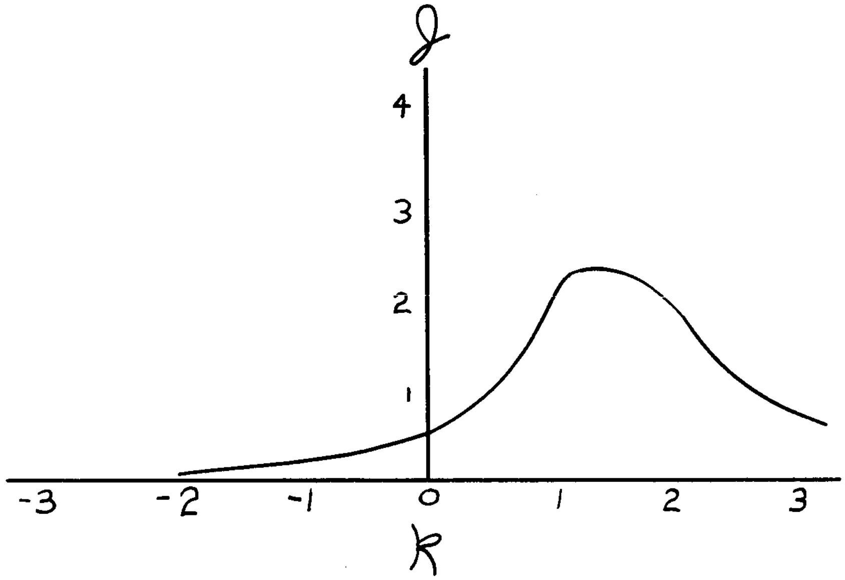

Diagram 11. The General Transonic Similarity Parameter

Diagram 12 illustrates the general nature of the pressure drag coefficient in the transonic flow regime for forebody profiles, aftbody profiles, and the complete profile.

The drag force characteristics of forebodies and aftbodies are distinctly different as can be seen in Diagram 12, where the drag force coefficient reaches a maximum at a free stream Mach number slightly less than unity for an aftbody, while the drag force coefficient reaches a maximum value at a free stream Mach number larger than unity for a forebody. The combination of the fore- and aft-bodies, which would represent the configuration of an airfoil profile, still exhibits the peak value of the drag coefficient at a Mach

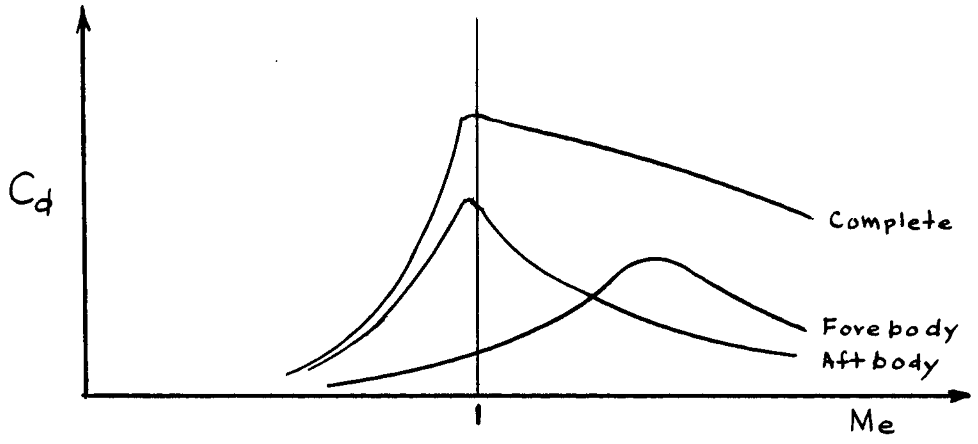

Diagram 12. Transonic Pressure Drag Force Characteristics for Forebody and Aftbody

number less than unity. It must be emphasized however that these qualitative remarks are for thin profiles not having major flow adjustments or large separated flow regions and for cases where the effect of shear layers on the surface is negligible.

F. Drag Force Due to Boundary Layer Rehabilitation Downstream of the V-Notch

Part of the contribution to the drag force of a v-shaped notch is the increased skin friction on the flat surface downstream from the notch due to the redeveloping shear layer. As can be seen in Figures 2, 3, 4, and 5 there is nearly always a region of separated flow inside of the notch which causes a distorted (in comparison to the fully developed turbulent velocity profile) velocity profile at the end of the notch.

A prediction of the variation of the drag force in this region can be based on the concepts of boundary layer development within shear flow regions (Reference 29) where this development is related to the shear layer development inside of the notch.

The drag force on the flat surface in the redevelopment region can also be approximated by assuming that the flow separates in passing over the notch and then redevelops at the start of the flat surface behind the notch. The parameter which can be used to relate the redeveloping drag force after the notch to the free shear layer development within the notch is the ratio of the effective approach velocity at the start of the redevelopment region to the external free stream velocity. This effective velocity will depend primarily upon the expansion angle Ω and the length of the separated region within the notch (along with some modifying factors). By making a reasonable estimate of this velocity ratio the redevelopment drag can be approximated. This method will be discussed in more detail in Chapter VI.

IV. EXPERIMENTAL INVESTIGATION

In order to evaluate the effect of notch geometry and boundary layer thickness on the drag coefficient an extensive series of tests was conducted in the supersonic and transonic flow regimes. All of the tests were conducted in a blowdown type wind tunnel instrumented with a newly designed drag force balance.

A. Experimental Objectives

The objectives were chosen to completely specify the effects of notch geometry, Mach number, Reynolds number, and shear layer thickness on the drag force.

1) Schlieren photographs were taken to obtain qualitative information about the flow field.
2) The oil film technique was used to locate the point of separation within the notch.
3) Static pressure distributions were measured to establish the importance of the pressure drag term.
4) Boundary layer traverses were made in the transonic and supersonic test sections in order to define the boundary layer.
5) A drag balance was designed and calibrated to be used with the blowdown wind tunnel.
6) Models of various notch lengths and notch angles were tested in supersonic and transonic flow.

7) One notch ($\Omega = 7^\circ$, $L = 3/8''$) was tested at various locations on the flat surface of the model in order to determine the effect on the downstream drag coefficient.

B. Blowdown Facilities

The experimental work was carried out in the supersonic and transonic blowdown wind tunnel operated jointly by the Department of Mechanical and Industrial Engineering and the Department of Aeronautical and Astronautical Engineering. This tunnel is located in Aeronautical Laboratory B at the University of Illinois, Urbana, Illinois. The blowdown tunnel was supplied with air from a system of storage tanks with a total capacity of approximately 2500 cubic feet. The storage tank system was filled by using a 125 horsepower air compressor pumping up to a maximum pressure of 115 psig. Approximately one-half of an hour was required to fill the storage tank system to its capacity at 115 psig.

The supersonic test section had an area of 8 square inches and allowed observation through glass side windows and could be operated with stagnation pressures between 13 psig and approximately 60 psig. The stagnation temperature varied between 50 F and 90 F depending on the ambient conditions, stagnation pressure and run-time. The maximum run time for the supersonic tunnel was approximately four minutes for low stagnation pressures (less than 25 psig) and one minute for the higher stagnation pressures (greater than 35 psig). The test section Mach number was 1.96 but varied slightly with the stagnation pressure. At a stagnation pressure of about 30 psia and a stagnation temperature of 50 F the tunnel had a Reynolds number per foot of 9 x 10^6.

A transonic test section with rectangular cross section was also used where the side walls consisted of glass plates suitable for optical studies while the top and bottom walls were slotted. For the purpose of the present investigation the slotted wall at the bottom was replaced by a solid wall into which the notch models or the balance carrying the drag models could be installed. The reduction in the wall permeability was permissible due to the small effective blockage effects of the models. The Mach number at the test section could be varied from approximately 0.5 to 1.2 by changing the tunnel stagnation pressure. No direct means of controlling the Reynolds number is possible in this range. The momentum thickness Reynolds number at the beginning of the test section varied from 7800 to 9500 for the stated Mach number variation. The maximum running time for the transonic test section was approximately one and one-half minutes at the higher Mach numbers (1 → 1.2) and about three minutes at the lower (less than 0.9) Mach numbers.

C. Design of the Drag Force Balance

At the inception of this investigation there was no means for directly measuring drag forces on the model in the tunnel so a drag force balance was designed and constructed.

The basic design characteristics which were necessary for a force balance for two-dimensional models are listed below.

i) Indicate drag or thrust forces from 0.05 lb to 5 lb.

ii) Indicate drag or thrust independent of lift and center of pressure.

iii) Have model deflections less than 0.002 inches.

iv) Capabilities to allow accurate alignment to within ±0.001 inch between the model surface and the edge of the base of the balance.

v) Capabilities to measure pressure distributions in the gap between the model and the balance base.

vi) Seals between the model and the balance base at the upstream and downstream edges that allowed only a negligible flow rate of air into and out of the gap without interfering with the force measurement.

vii) An electrical output signal that was of sufficient size to be measured and changed enough to give an accurate and repeatable reading of drag force.

viii) Large enough side gaps to that pressure differentials did not exist between the balance cavity and the tunnel static pressure (Blowdown operation).

ix) Symmetrical design so that thermal stresses did not cause extraneous forces in the same sense as the drag force (Blowdown transients).

x) Proper thermal insulation so that temperature changes at the electrical sensors did not cause extraneous electrical signals.

xi) Compatibility with the existing blowdown facilities so that major tunnel modifications were not needed.

In order to meet the design requirements i), ii), iii), vii), and ix), strain gages were chosen as the sensing elements for the drag force. Another type of sensing element that might have been used was the differential transformer. This type of transformer uses a mechanical deflection to produce a corresponding change in reactance. However, strain gages were chosen over the differential transformer because of cost and their electrical characteristics.

Perry and Lissner (Reference 38) state that the best way to measure drag independent of lift and point of location was by using a platform on legs with strain gages mounted at the bottom of the legs. This arrangement is shown in Figure 8. When four strain gages were used and connected in the bridge as shown in Figure 8, the following advantages were gained:

i) The change in resistance in the output leg of the bridge was twice that of a single gage.

ii) The change of resistance due to the weight of the model and lift force was equal in all four strain gages and thus it did not affect the output signal.

iii) When all four strain gages are exposed to the same temperature change then the change of resistance due to a temperature change of the gages does not affect the output signal.

iv) The moments caused by the non-symmetric application of the drag force did not affect the output signal because the resistance changes in the bridge arms summed to zero.

The next step in the design was to determine if a large enough strain was produced by the drag forces which were to be measured while at the same time maintaining a reasonable length and thickness of the strain beams.

The stress at the outer fiber in a cantilever beam is

$$S = \frac{Bz}{I} = \epsilon E \qquad (46)$$

but,

$$\epsilon E = \frac{F \ell \, t/2}{W \, t^3} \quad (12)$$

so that

$$\epsilon = \frac{6 F \ell}{E w t^2} \quad . \tag{47}$$

The deflection of the end of the cantilever beam is

$$\bar{y} = \frac{F \ell^3}{3 E I} \tag{48}$$

or

$$\bar{y} = \frac{4 F \ell^3}{E w t^3} \quad . \tag{49}$$

Equations (47) and (48) relate the properties that affect the output signal ($\Delta V \propto \epsilon$) and the deflection of the model, $\bar{y}$. Calculations were made using these two equations to determine what would be the best material and size of beam for maximum strain (ϵ) with minimum deflection ($\bar{y}$). The calculations were made for three different materials: aluminum, brass, and steel and for a force range of 0.1 lb. to 5 lbs. The length of the beam considered was from 1½" to 4" because of tunnel restrictions and the width of the beam was varied from ½" to 1½". The thickness of the beam ranged from 0.100 to 0.150 inches. The minimum output signal (ϵ) was chosen to be 200 micro inches/inch. This value was chosen because it gave a full scale deflection on the equipment available for measurement. For the maximum force with this strain the deflection was found to be 0.002 inches. From these calculations the best beam material and dimensions were found to be:

i) Aluminum
ii) Length = 2"
iii) Width = 0.5"
iv) Thickness = 0.125".

The next design step was to specify the model clearance. This value was determined by fixing the maximum measurable force. A 5 lb. force acting on the model gave a deflection 0.0024 inches. The minimum clearance between the force balance and model was therefore set at 0.003". With these design dimensions and a model size of 2½" by 4" long another problem presented itself, namely that of flow between the model and the base by virtue of the pressure gradient in this space, and the blow down pressure transient $(dp/d\bar{t})$ inside of the balance.

Calculations were made to estimate how rapidly the pressure inside the balance changed with respect to the static pressure change in the tunnel. The reason for concern about this pressure transient was that the transient existed on either side of the model and that if the clearances between the model and the indicator were too small, large forces would exist on the model during start-up. For the calculation of this pressure transient, the following approximations were made:

i) ideal gas

ii) reversible adiabatic process in the large volume

iii) laminar out-flow between two parallel walls (model and balance) without seals

iv) experimental data from blowdown tunnel was used.

With the gap clearance stated above and the preceding assumptions the pressure transient was

$$\frac{dp}{dt} = K R T \frac{\bar{A}}{\bar{V}} \frac{g_c \bar{d}^2}{3\nu} \frac{dp}{dx} \qquad (50)$$

and substituting yielded

$$\frac{dp}{dt} = 38{,}000 \text{ psi./sec.}$$

With a maximum indicator volume pressure change of about 10 psi there was no problem with transient pressure equilibrium during tunnel start-up.

With the gap clearance stated above there would be flow from the test section into the balance cavity and from the balance cavity back into the test section. This flow in general would be into the cavity at the downstream gap and out of the upstream gap into the test section boundary layer (see Figure 9). Of course, with expansion waves or shock waves near the floating element these flow rates might be reversed. It was virtually impossible to completely eliminate this flow of air but it was possible to make the flow rate very small. Two detrimental effects existed from this circulation around the floating element model. The first, a rather large pressure drop through the gap existed, causing a force which acted on the model in the direction of the drag force, and second, there was the disturbance created in the boundary layer because of the flow out of and then back into the boundary layer.

In order to successfully measure drag forces on two-dimensional models this circulatory flow rate had to be minimized. The method chosen for doing this was to use labyrinth seals on the underside of the model. A schematic diagram of this arrangement is shown in Figure 9. The labyrinth seals are located near the upper and lower surfaces so as to cancel the viscous flow forces developed within the labyrinths. These seals were so located that the pressure force on the sides of the model in the direction of the drag force was constant. This was true if the space between the model and the balance was larger than the gap clearance; however, provision was made to measure these pressures acting on the model faces. A series of pressure taps were located in the force balance across from the model faces where these pressures acted. There were four pressure taps for each face so that the pressure gradient could be determined. Theoretical calculations were made (Reference 43) in order to find the flow rate as a function of the number of seals and the gap clearance.

The design value for the seal gap clearance was chosen as 0.002 inches and seven labyrinth seals were used. This gave a flow rate through the model clearance space of 5×10^{-6} lb/sec. The model clearance was chosen as 0.003 inches so that the calculated velocity within the passage and into the tunnel test section was 4 feet/sec. These quantities were small in comparison to the tunnel flow rate of 3 lb/sec. and the test section velocity of 1600 feet/sec.

The next phase in the design of the drag force balance was to assemble an electronic system for measuring the electrical output signal from the strain gage bridge formed by the four gages located on the beams. The gages used were Baldwin-Lima-Hamilton type FAP 50-12-12 foil gages. They were specifically designed for small static strains.

A Baldwin-Lima-Hamilton Type N strain indicator was used for measuring the output signal from the strain gage bridge, however, it was discovered that the output of the bridge circuit in the drag balance was not large enough to give an accurate reading on the strain indicator. In order to increase the signal coming from the drag balance bridge a low level pre-amplifier was designed and used with the Baldwin-Lima-Hamilton strain indicator. The circuit for this multi-gain pre-amplifier was designed to match the frequency and voltage level of the strain indicator because the carrier signal from the strain indicator was preamplified and then returned to the strain indicator where it was amplified again and compared to a measuring bridge. This measuring bridge was sensitive to both voltage and frequency of the signal so that no large distortion in any of the amplifiers was permissible. This low-level preamplifier had a range of gain from 5 to 30 in increments of 5 along with a balancing potentiometer which was used for convenience in setting the reading dial on the strain indicator. A schematic diagram of the electronic system is shown in Figure 10.

D. Calibration and Testing

The drag force balance was extensively tested for preciseness and accuracy and it was also checked to see that it met the general design requirements. The model used for aerodynamic testing was a flat plate 4 inches long and 2.5 inches wide.

The results of the tests were satisfying. For various Reynolds numbers in the tunnel the minimum reading obtained was about 10% of the dial capability of 200 units. The dial position could be read to within ±2 units.

The repetitiousness of test results was good for both the dead weight and the aerodynamic calibration. Virtually no zero shift occurred in the output signal for a force less than 0.4 lbs, however, at larger loads (greater than 1 pound) there was some zero shift but it was small, about 10 units out of 2000. The drag balance was calibrated statically for both an upstream force and a downstream force, by using a string and weights with a pulley. The pulley was mounted on a miniature instrument bearing to reduce frictional forces during calibration and the drag force balance was calibrated while it was in place in the wind tunnel. A typical calibration curve is shown in Figure 11. Many readings were taken to establish the curve and the data were repeatable to within ±½%. The calibration curve was linear in this force range, as was expected, and passed through zero. The calibration constant, from the curve, was

$$\bar{K} = 0.1314 \text{ grams/dial unit.}$$

To verify that the balance measured only drag forces, a weight was placed on the horizontal flat plate model at different positions. No change in the output signal was observed.

To show that the balance reading was independent of the point of action of the drag force, the peg for connecting the calibrating force was moved to different locations along the centerline of the plate. The point of application of the calibrating force made no difference in the output signal of the balance.

The drag force balance was tested aerodynamically by using a flat plate model. This testing was conducted to determine three basic characteristics of the indicator:

i) accuracy
ii) plate misalignment effects
iii) effectiveness of the labyrinth seals.

Before the accuracy of the balance could be verified the boundary layer at the beginning of the flat plate had to be defined. Once the approach boundary layer was defined, published theoretical or experimental values for drag coefficients were found for the corresponding boundary layer conditions.

1. Classification of the Supersonic Turbulent Boundary Layer

Velocity traverses were made with a small probe (0.018 inches thick) on the floor of the tunnel at the beginning of the test section. The probe was attached to a linear position indicator (strain gage beam) and its output was recorded on a recording oscillograph. The pressure inside the probe was measured with a pressure transducer and recorded on the same oscillograph trace. The recording oscillograph was manufactured by the Consolidated Electrodynamics Corporation (CEC) and was of Type 5-116. The pressure transducer was also manufactured by CEC and had a range of 0 to 100 psia. The pressure transducer and the linear indicator were both energized by a CEC Type 2-105 A oscillator power supply, and their output signals were amplified by two CEC Type 113-B carrier amplifiers. Before each test both the linear position indicator and the pressure transducer were calibrated using a micrometer and a Wallace and Tiernan precision pressure gage respectively.

The results of these traverses are shown in Table 2. The characteristics determined from these traverses were; boundary layer thickness δ, displacement thickness δ^*, momentum thickness θ, shape parameter H, Reynolds number based on the virtual length Re_x, and Reynolds number based on the momentum thickness Re_θ.

Table 2. Supersonic Turbulent Boundary Layer Characteristics at the Beginning of the Test Section

P_o psia.	δ ins.	δ^* ins.	θ ins.	H	Re_x	Re_θ
34.0	0.147	0.035	0.0104	3.33	8.13×10^6	8855
39.95	0.147	0.0332	0.0099	3.34	8.36×10^6	9966
44.6	0.146	0.0324	0.0098	3.31	10.6×10^6	10944
49.4	0.144	0.031	0.00939	3.30	11.5×10^6	11685

Figures 13, 14 and 15 show various plots of pitot tube traverse data. In Figure 13 u/u_e is plotted against y/δ for four different tunnel stagnation pressures or Reynolds numbers. Also shown in this figure is the commonly used 1/7 profile. It was evident that the experimental velocity profiles were not exactly 1/7 profiles. This fact was not surprising since tunnel turbulence level and previous boundary layer history affect the shape of the velocity profile. Several comments must be made about these data. First of all, Figures 13, 14, and 15 indicated that there was probe-wall interference for $y/\delta < 0.3$ and for $y/\theta < 4$. When a probe of the size used here (0.018") was placed near the wall there were regions of separated flow near the tip of the probe and the wall causing smaller total pressure readings. Also, when the probe was near the wall there was interference between the wall and the bow shock that stood in front of the total pressure probe. As the probe was moved away from the wall this bow shock stood off from and curved around the front of the probe. When calculating the velocity from the total pressure reading, it was assumed that this bow shock was flat and normal to the probe at the probe centerline. This bow shock-wall interference caused the measured velocity to be lower than the actual velocity. This type of probe interference was reported and verified by Wilson (Reference 51), Brinich and Diaconis (Reference 4), and O'Donnel (Reference 36). The error caused in the momentum thickness by the bow shock wall interference was estimated to be about -5%. The error in the displacement thickness measurement was almost twice as great at about +10%. Using these probable errors and the values for displacement thickness and momentum thickness from Table 2, H was recalculated. The new value of H is very close to 3.1 which is the approximate accepted value for a Mach number equal to two as given by Wilson (Reference 51).

Figure 14 indicated a second important feature of the experimental velocity profiles. This Figure shows u/u_e against y/θ for the experimental points and for the theoretical curve of

$$\frac{u}{u_e} = 0.683\left(\frac{y}{\theta}\right)^{1/7} \tag{51}$$

Equation (51) was taken from Reference 36 and it was verified by Brinich and Diaconis (Reference 5). A second empirical curve was plotted according to equation (52).

$$\frac{u}{u_e} = 0.698\left(\frac{y}{\theta}\right)^{1/7} \tag{52}$$

It is seen in Figure 14 that the experimental data fits the curve given by equation (52) for $y/\theta > 4$.

Figure 15 is a plot indicating that the outer portion ($y/\delta > 0.3$) of the compressible turbulent boundary layer did have 1/7 slope.

The boundary layer growth and development was also calculated theoretically with the aid of the IBM 7094 Digital Computer located at the University of Illinois, Urbana, Illinois, using the method given in Reference 25. This method is an approximate one, and was based on integral forms for the momentum and energy equations, and on a transformation which was suggested by Culick and Hill (Reference 14) as the turbulent analog to the Stewartson-Illingworth transformation for laminar flow.

The computer program used as input the actual tunnel Mach number distribution, reference gas properties (P_O, T_O, R, μ_o), the empirical compressible boundary layer characteristics N and $\alpha(N)$ (see Chapter III), and the transition Reynolds number. The output consisted of the momentum thickness, displacement thickness, and shape parameter. Figure 16 is a comparison of the computer results with the measured results at the start of the model. The deviation between the two results varied from about 1% at 30 psia. to 5% at 50 psia. Table 3 gives a comparison between the measured values and the calculated values for various stagnation pressures.

Figure 17 is a graphic comparison of the calculated Re_θ at the start of the model and the measured Re_θ at the same location as a function of stagnation pressure.

Table 3. Comparison of Calculated and Measured Boundary Layer Quantities at the End of the Splitter Plate

P_o, psia.	$*$, in.		θ, in.		H	
	calc.	meas.	calc.	meas.	calc.	meas.
34.0	0.0306	0.035	0.0105	0.0104	2.91	3.33
39.95	0.0299	0.033	0.0103	0.0099	2.90	3.34
44.6	0.0291	0.0325	0.0101	0.0098	2.9	3.31
49.4	0.0286	0.0309	0.0099	0.0094	2.89	3.30

2. Classification of the Transonic Turbulent Boundary Layer

Similar boundary layer traverses were made for the transonic flow regime using the same equipment as was used for the supersonic measurements. The results from these measurements are presented in Table 4.

Table 4. Transonic Boundary Layer Characteristics at the Beginning of the Test Section

M_e	θ, in.	*, in.	H	Re_θ
0.606	0.023	0.0331	1.433	7920
0.91	0.0206	0.0346	1.683	9350
1.11	0.0156	0.0287	1.838	8530
1.24	0.0127	0.0242	1.902	8270

The momentum thicknesses calculated from the velocity traverses are plotted in Figure 18. These traverses were made at two locations in the test section so that not only the absolute value of θ was determined but also the gradient of the momentum thickness in the flow direction was estimated.

The results of the transonic velocity traverses were similar to those taken for supersonic flow and the velocity profiles for the two flow regimes were comparable with respect to shape and thickness. However, an absolute comparison of all the quantities listed in Tables 2 and 4 is not possible since the momentum thickness and the density values are not the same. The momentum thickness Reynolds number at the start of the drag balance model was plotted in Figure 19. Re_θ reached a maximum value near Mach number equal to one and then decreased with increasing Mach number. The level of Re_θ and the location of the maximum Re_θ is a characteristic of each tunnel and cannot be compared in absolute value to results from other wind tunnels.

3. Accuracy of Flat Plate Measurements

The accuracy of drag force measurements in supersonic turbulent flow was difficult to ascertain. By examining previous results such as those presented in References 21, 23, 42, 44, 39, and 51 it was seen that accurate values of C_f and C_F were difficult to establish. There are several reasons for the uncertainty in the values of C_f and C_F. The main reason is that for data obtained from wind tunnel tests there is difficulty in establishing an accurate reference length to be used in the Reynolds number. In most cases the reference length used was the distance from a virtual origin where it was assumed that the turbulent boundary layer began. In most of the experimental investigations reported boundary layer trips were used to force the flow into a turbulent boundary layer. In these cases the usual assumption was that for small boundary layer trips the momentum thickness in the laminar boundary layer at transition was equal to the momentum thickness in the turbulent boundary layer at transition. With this assumption a virtual origin for the turbulent boundary layer was established.

Other factors which influenced the accuracy of C_f C_F were the level of turbulence in the tunnel and the rate of heat transfer on the model surface.

Two approximate methods were used for comparing the results of the drag force balance with published values of drag. One was to use the drag force found from the drag balance and calculate an average wall shear stress and a C_f for the entire plate based on this average wall shear stress. Then, using a Reynolds number based on the length to the center of the plate, compare C_f with local values at this Reynolds number.

Some of the data obtained with the flat plate model mounted in the drag indicator are shown in Figure 20 plotted as a calculated C_f versus stagnation pressure P_o. There are three other points indicated on this plot that were taken from References 23 and 39. The three points shown were obtained at tunnel conditions very close to the tunnel conditions of the present experimental data. The conditions that were matched were Mach number, stagnation pressure, momentum thickness, Re_θ, and Re_x. As can be seen the agreement between the experimental data and the published results was satisfactory. There was a small displacement of 5% but this was probably due to the approximations that were made.

A second approximate method of analysis of the data was made using published values of the integrated coefficient C_F to find the drag force on a plate this size for the tunnel conditions used and then compare this drag force with the drag force obtained experimentally from the drag balance. The results of this method are shown in Figure 21. The drag force was linear with respect to the stagnation pressure in this pressure range. Also shown in this Figure is one point where the drag force was calculated using an average C_F

(Reference 39) at almost the same tunnel conditions as existed when the experimental points were obtained. Again, the drag force balance results were almost indistinguishable from those reported in the literature.

Figure 22 is a more accurate comparison of the experimental flat plate results with theory. Equation (24) was used with N = 5 to calculate $\overline{C}_f$ at the center of the model, where $\overline{Re}_\theta$ is the average Re_θ for the flat plate. The agreement between the experimental values and the theoretical values is excellent.

The flat plate model was also tested in the transonic test section and the experimental drag forces are plotted in Figure 23. The transonic data was less precise than the supersonic data but still of good quality.

Considering all of the comparisons presented in Figures 20, 21, and 22 several conclusions can be made about the drag force balance. First, the accuracy of the measurements made by the balance is within reasonable limits. Second, the precision of the balance is within the usual experimental limits. The exact precision of the measurements was influenced by factors other than the drag force measurement. Such factors as the throttle control valve on the tunnel and the transient pressure measurements caused a loss in the precision of the drag force measurements.

4. Plate Misalignment Effects

Some tests were run with the drag balance where the flat plate model was intentionally misaligned with the balance base. The results of these tests showed that there was about a 10% deviation from the aligned value with approximately 0.003 inches misalignment. This deviation was somewhat less than that reported by O'Donnel and Westkaemper (Reference 37) who reported about 16% deviation at 0.003 inches misalignment at a Mach number equal to two. The misalignment effects reported here however cannot be compared on an absolute basis to those reported by O'Donnel and Waestkaemper because of the difference in the order of magnitude of the forces which were measured, but the qualitative effects were identical. Table 5 gives the deviations from the aligned position for several values of misalignment. With the present model of the drag force balance the misalignment can be kept to within ±0.001 inches so that there was probably about ±3% error in the results due to misalignment.

Table 5. Misalignment Effects (Reference 37)

$M_e = 2.0$	$Re_\theta = 9830$
Misalignment (inches)	Deviation (% of aligned reading)
+0.001	+ 3
-0.001	- 3
+0.002	+ 8
-0.002	- 8
+0.003	+16

5. Effectiveness of the Labyrinth Seals

During the testing of the drag force balance several of the pressure distributions along the upstream and downstream faces were plotted in order to determine if the labyrinth seals were effective. These plots disclosed that if approximately 0.003 inches seal clearance were maintained then the pressure along the model faces was constant. Tests were run with and without the seals for the flat plate model and there was essentially no difference in the indicated drag force. The seals were intended only to reduce the flow rate due to a large pressure difference between the upstream and downstream gaps, but for the models tested in the remainder of the test program there were no large pressure differences at these two locations. Therefore, the remaining tests were conducted without using the seals.

E. Notch Drag Force Models

A large set of notch configurations and drag force models were tested. The models were all made of steel so that they could be surface ground to make all of the model surfaces smooth. The models used are listed in Table 6.

Table 6. Drag Force Model Dimensions

Notch Length (in.)	Notch Angle (°)	Notch Depth (in.)	Notch Shape	Distance from Model Leading Edge to Notch Leading Edge (in.)
3.5	7	0.215	V	0.25
3.5	10	0.308	V	0.25
3.5	13	0.405	V	0.25
2.25	7	0.138	V	1.5
2.25	10	0.198	V	1.5
2.25	13	0.260	V	1.5
1.0	7	0.061	V	2.75
1.0	10	0.088	V	2.75
1.0	13	0.115	V	2.75
0.625	7	0.038	V	3.31
0.625	10	0.055	V	3.31
0.625	13	0.072	V	3.31
0.375	7	0.023	V	3.56
0.375	10	0.033	V	3.56
0.375	13	0.043	V	3.56
1.0	90	0.75	Rectang.	2.75
2.25	90	0.75	Rectang.	1.50
0.512	--	0.70	Circular	2.98
0.375	7	0.023	V	3.25
0.375	7	0.023	V	2.875
0.375	7	0.023	V	2.5
0.375	7	0.023	V	2.125
0.375	7	0.023	V	1.5
0.375	7	0.023	V	1.125

V. EXPERIMENTAL RESULTS FOR V-NOTCHES

A. Separation Point Studies

Several methods were used to locate the point of separation inside the v-shaped notches. Schlieren photographs were taken of the flow fields in supersonic and transonic flow for many of the v-shaped notches listed in Table 6. From these photographs approximate separation locations were measured and recorded. Typical photographs are shown in Figures 2, 3, 4, and 5.

For many of the notch shapes models were constructed with pressure taps (approximately 40) along the bottom of the notch so that static pressure distributions could be measured in the notch. A typical notch pressure distribution is shown in Figure 6 for a two inch, ten degrees notch with a free stream Mach number of 1.96. The approximate separation and reattachment points are also indicated in Figure 6.

A third method that was used to locate the point of separation was the oil film technique. In this method a thin film of heavy oil (steam cylinder oil) was placed along the separating surface before the test. During the test a thin line of oil accumulated at the separation region due to the reversed flow on the downstream side of the separation point. The location of this line was then recorded by observing its position relative to the pressure taps.

The results from all three methods are shown in Figure 24 for a two inch long notch. The individual results from the different techniques are not differentiated in Figure 24 but the three methods were all in close agreement.

B. Supersonic Drag Coefficients

Nearly all of the notches listed in Table 6 were tested in the supersonic test section. For each of the notches tested two corrections were made to the indicated drag force. Diagram 13 depicts the forces acting on the model during the test.

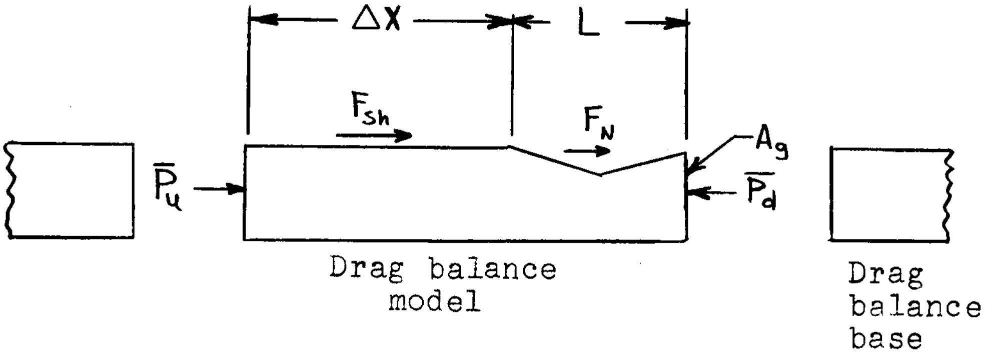

Diagram 13. Drag Force Correction Terms

$\overline{P}_u$ is the average pressure acting on the area A_g in the upstream model gap and $\overline{P}_d$ is the average pressure acting on the area A_g in the downstream model gap. The first correction term was that of the force, $F_{\Delta p}$, acting on the model due to the pressure difference acting on the two model faces perpendicular to the free stream. $F_{\Delta p}$ is given by

$$F_{\Delta p} = \left(\bar{P}_u - \bar{P}_d\right) A_g$$

where A_g is the area over which the average pressures act. The second correction which was made to the indicated drag force reading accounted for the friction drag acting on the flat plate portion of the model. This correction term, F_{sh}, is given by

$$F_{sh} = \frac{1}{2} \rho_e u_e^2 \Delta x \, b \, \overline{C_f}$$

where $\bar{C}_f$ is the average drag force coefficient acting on the surface of length Δx and is given by equation (24).

The net drag force F_N of the notch then is given by

$$F_N = F_{balance} - F_{sh} - F_{\Delta p}$$

where $F_{balance}$ is the reading obtained from the drag force balance during the test.

For each model tested in the supersonic section the Reynolds number was the only quantity that could be varied. The results from the supersonic notch tests are given in Table 7 which is located in the Appendix due to its length. The results listed in Table 7 are plotted in Figures 25, 26, 27, and 28 with the notch drag coefficient as the ordinate and the momentum thickness Reynolds number as the abscissa with notch length and angle as parameters. The effect of the shear layer thickness on the drag coefficient is depicted in Figure 29 and will be discussed in Chapter VI.

C. Transonic Drag Coefficients

Nearly all of the notches listed in Table 6 were tested in the transonic test section in a manner similar to that presented in Part B above. However, for the transonic tests the main variable was the Mach number and there was no direct control over the Reynolds number. The results from the transonic tests are given in Table 8, located in the Appendix. The primary results, drag coefficient as a function of Mach number, are plotted in Figures 32, 33, and 34 with notch length and notch angle as parameters. Figure 40 shows the effects of the shear layer thickness, θ/L, on the drag coefficient with Mach number as a parameter.

D. Drag Force Test for Determining the Friction Drag of the Downstream Redevelopment

A series of tests were conducted in the supersonic test section in order to determine the influence of the notch on the friction drag force acting on the flat plate portion downstream from the notch. This effect was determined by placing the notch at different locations on the model in the drag force balance. For each test the same notch geometry was used but the notch was placed progressively further upstream for each test.

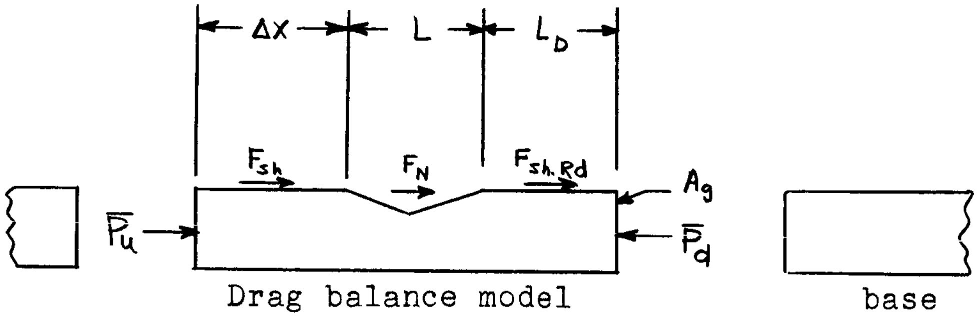

$$F_{sh} = \tfrac{1}{2}\, \rho_e\, u_e^2\, \Delta x\, b\, \bar{c}_f$$

$$F_{\Delta p} = (\bar{P}_u - \bar{P}_d)\, A_g$$

$$F_N = \text{(experimental data)}$$

Diagram 14. Redevelopment Drag Force Correction Terms

Not only were the two corrections $F_{\Delta p}$ and F_{sh} made to the indicated drag force $F_{balance}$ as described in Part B above, but also the correction term for the drag force created by the notch was made. This additional correction term F_N is illustrated in Diagram 14 and its value was determined from the results obtained in the supersonic notch tests. The shear force, F_{shRd}, on the flat surface of the model after the notch is given by

$$F_{shRd} = F_{balance} - F_{sh} - F_N - F_{\Delta p}.$$

The results from this test are given in Table 9.

Table 9. Downstream Redevelopment Drag Force Results

Notch Length = 0.375", $\Omega = 7^\circ$; $M_e = 1.96$, $Re_\theta = 10000$.

Notch Position from Downstream Edge of Model (inches)	Drag/Drag of Flat Plate without Notch	$\frac{\text{Length of Plate}}{\text{Length of Notch}}$
0.330	2.45	0.91
0.700	1.94	1.86
1.125	0.95	3.0
1.50	0.87	4.0
2.15	0.88	5.73
2.5	0.93	6.67

VI. DISCUSSION OF RESULTS

The discussion of the experimental results of this investigation and the comparisons with existing theoretical analyses and proposed flow models has been separated into categories determined by the physical nature of the results. The primary variables of this investigation, as stated previously, are Mach number, notch angle, Reynolds number, and shear layer thickness. However, the experimental results shown in Figures 29 and 40 indicate that the Reynolds number effect is of minor importance when compared with the other variables. For this reason the results of this investigation are discussed, for any given Mach number, utilizing θ/L as the primary variable indicating the shear layer effect while the momentum thickness Reynolds number will be treated as a secondary variable.

The results have been classified into four categories; v-notch drag force coefficients for thin approaching boundary layers, v-notch drag force coefficients for thick approaching boundary layers, drag forces of rectangular and circular notches, and redeveloping shear layer drag downstream from the notch.

The reason for classification in terms of thick and thin approaching boundary layers is evident in Figures 29 and 40 where the effect of the shear layer on the notch drag coefficient is shown. For the supersonic results shown in

Figure 29 it is clear that the notch angle is a significant factor in the determination of the drag coefficient for $\theta/L < 0.02$ while for $\theta/L > 0.02$ it is independent of the notch angle. A similar trend for transonic flow can be observed in Figure 40, however, the value of θ/L where the drag coefficient becomes independent of notch angle is seen to be a function of Mach number.

For purposes of discussion a thin approaching boundary layer is one in which θ/L is small enough so that the notch angle affects the drag coefficient while a thick approaching boundary layer is one where the notch drag coefficient is independent of the notch angle. From Figures 29 and 40 estimates of the values of θ/L for thin and thick boundary layers can be made. For $1.1 < M_e < 2$,

$$\left(\frac{\theta}{L}\right)_{\text{thin}} < 0.02 < \left(\frac{\theta}{L}\right)_{\text{thick}}$$

while for a subsonic Mach number of 0.6

$$\left(\frac{\theta}{L}\right)_{\text{thin}} < 0.09 < \left(\frac{\theta}{L}\right)_{\text{thick}} \quad .$$

A. Thin Approaching Boundary Layers

For the thin boundary layer regime the boundary layer thickness was at most equal to the notch length.

1. Supersonic Results, $M_e \cong 2$

The effects which are discussed for supersonic external flow with a thin approaching boundary layer are Reynolds number, notch angle, and shear layer thickness.

a. Reynolds Number Effect

All of the v-shaped notches tested in the supersonic ($M_e = 1.95$) regime with thin approaching boundary layers exhibited an effect on the drag force coefficient for a change in the Reynolds number. The notch drag coefficients for supersonic flow are plotted in Figures 25, 26, and 27 with the momentum thickness Reynolds number as the abscissa. The drag coefficients increase with an increase in Reynolds number in these figures, however, this increase in the drag coefficient is not due solely to an increase in Reynolds number. In order to obtain a Reynolds number variation in the wind tunnel the stagnation pressure was varied. The change in stagnation pressure also caused a change in the momentum thickness (see Figure 16) of the boundary layer so that the effect shown in Figures 25, 26, and 27 is a combined Reynolds number effect and shear layer thickness effect. In order to isolate the Reynolds number effect the data was replotted in Figure 29 for constant values of the Reynolds number at various shear layer thicknesses. This figure indicates that for a constant shear layer thickness and notch angle the drag coefficient increases with increasing Reynolds number for thin approach boundary layers. The wind tunnel used in obtaining these results did not have a large enough range in stagnation pressure to determine precisely the Reynolds number effect, however, for the range tested ($10000 < Re_{\theta} < 15000$) this effect can be estimated by utilizing the linear approximations shown in Figure 29.

b. Notch Angle Effect

The change in drag coefficient caused by a change in the notch angle can be most easily observed in Figure 28. In the range of variables considered here (L = 3.5", 2.25", and 0.375 in. for thin boundary layers) the notch drag coefficient increased with increasing notch angle for a given notch length. Also shown in Figure 28 are the drag coefficients estimated by using inviscid linearized supersonic theory for half-diamond-shaped profiles. Comparison of the actual drag coefficients with the half-diamond-profile drag coefficients illustrates how the flow separation from the notch walls (Chapter III) alters the gas dynamic solution (Figure 6) to this drag problem.

For the 7° half-diamond-profile the linearized supersonic theory yields a value of 0.0175 for c_d at $M_e = 1.95$. The values of notch drag coefficient for 7° notches ranges from 0.012 to 0.014 indicating that a small separated region was present in the 7° v-shaped notch (Figures 2 and 4a). For 10° half-diamond profiles the linearized theory yields a value for drag coefficient of 0.0355 while the values of the notch drag coefficients for 10° notches range from 0.018 to 0.022 indicating a more extensive geometry change for 10° notches than was present with the 7° notches. For the 13° half-diamond profiles the linearized theory drag coefficient was not even close to the measured notch drag coefficients. This progressive deviation of the drag coefficient from the linearized theory solution as the notch angle was increased demonstrated how the changing flow geometry reduced the drag coefficient from the theoretical solution based on the wall geometry.

A comparison of the experimental results with the solution obtained by using the model proposed in Chapter III Part E.3 for supersonic flow is shown in Figure 31. The solid lines in Figure 31 represent solutions of equation (42) using the proposed model and experimentally determined penetration depth ratios. The solid points in Figure 31 are the experimental results for the drag coefficient for various notch lengths and angles. The agreement between the proposed model solution and the experimental results is satisfactory considering the assumptions which are made in the proposed model. The characteristic trends of the solution are interesting to note. For a given notch length the increase of the drag coefficient for an increase in notch angle above 13° is negligible because the flow separates close to the leading edge of the notch making the wave drag contribution small in comparison to the shear drag in the developing shear layer region. The effect of decreasing the notch angle for a given notch length is also demonstrated in Figure 31. For very thin boundary layers ($\theta/L \approx 0.003$ or L = 3.5") the theoretical solution could be extrapolated to a maximum penetration depth ($d/r \rightarrow 1$) indicating that for a long (3.5") notch this would occur for a 6° notch angle. The results however are inconclusive in regard to extrapolation of any of the other notch length curves. The relation to flat plate friction drag ($\Omega \rightarrow 0$) and to fully separated flow past a rectangular cutout (see Figure 30) is shown in Figure 31a.

c. Shear Layer Effect

For thin boundary layers there is an effect on the drag coefficient as the geometry of the notch is changed. These effects are depicted in Figure 29. Figure 29 indicates that for each notch angle as the shear layer thickness was reduced the drag coefficient approached a constant value. This is clearly demonstrated for the 7° notch where C_d approached the linearized theory solution. For the deeper notches the maximum value for the drag coefficient was not reached in this experimental investigation however it would be reached if θ/L were decreased to a sufficiently low value.

2. Transonic Results, $M_e = 0.6$ to 1.18

For the results obtained from the transonic flow regime the basic experimental parameters are different than they were in the supersonic regime. For these tests there was no direct control over the Reynolds number so that in this range of flow variables it was not possible to isolate the Reynolds number effect. However, this inability to establish the Reynolds number effect was not critical since as can be seen in Figure 19, Re_θ had only a small variation between 7800 at $M_e = 0.6$ and 9100 at $M_e = 0.9$. The three basic effects considered in the transonic regime for thin boundary layers are notch angle, shear layer thickness, and Mach number.

a. Notch Angle Effect

For the case of a thin approaching boundary layer an increase in notch angle resulted in an increase in the drag coefficient for the range of values of Mach number tested. This was indicated by the results shown in Figure 35 for a 2.25 inch long notch. The same results can be observed in Figures 32, 33, and 34 for the 3.5 inch and 1 inch notches which are long enough to be in the thin boundary layer classification. For the lower Mach number range (0.6 to 0.8) the shorter notches (0.625" and 0.375") are also in the thin approaching boundary layer classification (Figure 40) and the same effect on the drag coefficient for a change in the notch angle is noted in Figures 32, 33, and 34.

In Chapter III the transonic similarity parameters $\mathcal{K}$ and $\mathcal{J}$ were introduced as correlating parameters for drag force coefficients. The experimental results from this investigation were plotted in terms of the parameters κ and $\mathcal{J}$ in Figures 37, 38, and 39. It can be noted from these figures that κ and $\mathcal{J}$ are reasonable correlating parameters for thin approaching boundary layers.

b. Shear Layer Effect

For the transonic flow regime the same qualitative effect of the approaching shear layer thickness on the notch drag coefficient was observed, however, the results also indicated that the value of the momentum boundary layer thickness for which the drag coefficient becomes independent of the notch angle increases for subsonic Mach numbers. For a Mach number between 1.1 and 2 some of the v-notch results were in the thin boundary layer classification (see Figure 40) while in the subsonic range (0.6 → 0.8) of the transonic regime all of the notches tested fell into the thin boundary layer classification. Again, a maximum value of the drag coefficient was indicated for a given value of notch angle. It can be seen in Figure 40 that for $M_e = 0.6$ and $\Omega = 7^\circ$ the maximum value of the drag coefficient is about 0.004, while for $\Omega = 10^\circ$ and $M_e = 0.6$, the maximum value of C_d is about 0.007. A maximum value of C_d was not obtained in this investigation for $\Omega = 13^\circ$. It can also be seen in Figure 40 that for the subsonic Mach number range the notch angle effect is stronger than in the supersonic range. For $M_e = 0.6$ and $\theta/L = 0.006$ the drag coefficient for a 13° notch is more than twice that of a 7° notch while for $M_e = 1.1$ the drag coefficient for a 13° notch was only about 20% greater than that for a 7° notch.

c. Mach Number Effect

The Mach number effect observed in this investigation was the most pronounced effect and is illustrated in Figures 32, 33, 34, and 35. The increase in the drag coefficient as M_e is increased from a subsonic value through the transonic regime is typical, although for most profiles (References 5, 43), a maximum value for C_d occurs for M_e slightly less than one. It is obvious in Figures 32, 33, and 34 that for v-notches a maximum value in C_d is going to occur for a Mach number greater than one and that the value of M_e where this maximum of C_d occurs is going to be dependent on the notch angle.

A model was proposed in Chapter III which qualitatively accounts for this shift in the maximum value of the drag coefficient near Mach number one. This model used plane shock theory and Prandtl-Meyer expansion theory to calculate the drag force coefficient from $M_e = 2$ down to the Mach number where the shock wave at the vertex of the notch becomes detached from the vertex and moves upstream as the Mach number is decreased. The Mach number at which the shock detaches in the v-notch is dependent upon the notch angle and this relationship is shown in Figure 36. The significance of $(M_e)_{detach}$ will be discussed later on. After the shock detaches from the vertex the Mach freeze concept proposed by Bryson (Section E.3.c) has been used to calculate the drag coefficient. The results from this calculation were shown in Figure 7 for a 7° notch without separation and this curve has been replotted in Figure 35 along with the experimental drag coefficients for a notch length of 2.25". The qualitative agreement between the theory and experiment is good.

If the experimental results could be completed in the Mach number range of 1.2 to 1.9 a maximum C_d would probably occur at about the same Mach number as the theory estimates. For the 7° notch this maximum should be at $M_e = 1.33$ according to the flow model theory.

The theory and the experimental results do not agree quantitatively because in the actual flow case the flow separates from the surface causing the effective notch depth to decrease thus reducing the drag force coefficient. This change in the location of the separation point in passing through the transonic regime was shown in Figures 4 and 5 for a 7° notch. The location of the separation points for 7°, 10°, and 13° notches is shown in Figure 24 as a function of the Mach number. Using the separation point location at $M_e = 1$ it is seen that the flow separates about midway down into the notch. This location of separation would cause the actual drag force coefficient to be reduced by about one-half which is the case shown in Figure 35. However, as the Mach number is increased the separation point moves farther down into the notch (see

Figure 24) making the effective notch depth closer to the actual depth and causing the measured drag coefficient to be closer to the theoretical drag coefficient.

In summary then, the notch drag coefficient in the transonic flow regime can be estimated by using the proposed flow model (Chapter III, Section E.3.c) and multiplying this result by the ratio of the penetration depth to the notch depth obtained from Figure 24. That this concept gives reasonable results well into the transonic flow regime is shown by the dashed curve in Figure 35.

The value of the Mach number where the maximum drag coefficient occurs is estimated in Figure 36. The quantity $(M_e)_{detach}$ is the theoretical Mach number in the free stream when the shock detaches from the vertex of the notch.

B. Thick Approaching Boundary Layers

The definition of this classification was given before and represents approximately the regime where the approaching boundary thickness is greater than the notch length.

1. Supersonic Results, $M_e \approx 2$

The supersonic results in this category are divided into the same three effects that were considered for the thin boundary layers, Reynolds number, notch angle, and shear layer thickness.

a. Reynolds Number Effect

For the thick boundary layer case (L = 0.375" and 0.625") there was still an increase in C_d for an increase in Re_θ, however, the change was not as great as for the thin boundary layer case. The reason that this change is less is that the thicker approach boundary layer mollifies the effect of the notch on the free stream. The thicker layer acts as a buffer region between the solid boundaries and the free stream so that the velocity and pressure changes are not so great in this region. This effect is shown in Figure 29.

b. Notch Angle Effect

The results of this investigation show that for thick approach boundary layers the notch angle has very little effect on the drag coefficient, in fact, the method of classification used assumes C_d to be independent of the notch angle in this regime.

c. Shear Layer Effect

For the thick shear layers, as stated before, the boundary layer acted as a buffer region between the free stream and the solid boundaries with the net effect of reducing the drag coefficient. This reduction is quite obvious in Figure 28 where, as θ/L was increased, the drag force coefficient was reduced. Any theoretical estimate of the drag coefficient in this region would be very difficult because detailed information about the shear layer and its interaction with the solid walls would be necessary.

2. Transonic Results, $M_e = 0.6$ to 1.18

The results of the transonic flow regime tests for thick approaching boundary layers are also divided into the same categories as were the thin boundary layer results.

a. Notch Angle Effect

The thick approaching boundary layer in the transonic flow regime eliminates the notch angle effect as can be noted in Figures 32, 33, and 34 for L = 0.37", and 0.625". For these two lengths and for all of the notch angles tested there was only a small difference in the drag coefficient at each Mach number. Similar results were observed in Figures 37, 38, and 39 where the data were plotted in terms of $\mathcal{J}$ and $\mathcal{K}$. For the thick boundary layers the transonic similarity parameters $\mathcal{J}$ and $\mathcal{K}$ also correlated the drag force coefficient data satisfactorily.

b. Shear Layer Effect

For the supersonic Mach number range ($M_e > 1.1$) in the transonic flow regime the shear layer effects on the drag coefficient for the thick approaching boundary layers were identical to those for the thin boundary layers and were discussed in Section A.2.b of this chapter. For the subsonic range of the transonic regime the results for the thick approach boundary layer category are inconclusive.

c. Mach Number Effect

The Mach number effect for transonic thick approaching boundary layers was qualitatively the same as for the transonic thin approaching boundary layers. However, the quantitative effect was less intense for the thicker boundary layers as expected.

C. Drag Forces of Rectangular and Circular Cavities

Drag coefficients were measured for rectangular notches and circular cavities and these results are presented in Figure 30. The drag coefficients for rectangular notches were strongly dependent upon the notch length and only slightly dependent upon the Reynolds number. The values of the drag coefficient measured here do not agree with those given by Charwat, Roos, Dewey, and Hitz (Reference 9), (Diagram 6) which can only be partly explained by the fact that δ/r for these results was smaller by a factor of two than δ/r for their results.

A circular cavity was likewise tested in the drag balance and also a theoretical calculation of the drag force was made using equation (41). The agreement is shown to be very good.

D. Redeveloping Shear Layer Drag Downstream from the Notch

As described in Chapter V tests were conducted to measure the effect that the v-notch has on the shear layer drag downstream from the notch. The test procedure and results were given in Chapter V. Experimental data representing the ratio of the measured drag force to the drag force on a flat surface equal to the redevelopment length at the same tunnel location but without the notch upstream are plotted in Figure 41. Also shown in Figure 41 is a theoretical estimate of the redeveloping shear layer drag assuming that the effective velocity at the start of the redevelopment region is 75% of the free stream velocity. The method of calculation of this curve and the meaning of effective velocity was described in Chapter V. The experimental results exhibit the predicted trend and show reasonable quantitative agreement. The important conclusion from this series of tests is that there is a region of high frictional drag immediately behind the notch as a new boundary layer is developed within the shear flow layer present near the downstream corner of the v-notch, but that this high frictional drag decays to a fully developed boundary layer value within about four notch lengths downstream of the notch.

VII. CONCLUSIONS AND RECOMMENDATIONS

From the analytical and experimental results of this investigation the following conclusions may be made about the drag coefficients for v-shaped notches.

1) The drag force on two-dimensional models can be accurately determined by direct force measurements using a newly developed balance employing strain gages. In particular, the effect of the notch angle at given values of Mach number and Reynolds number is shown to produce a continuous variation from flat plate friction drag values through combined wave drag and free jet mixing contribution to the shear drag in fully separated flow regions.
2) The influences of the major experimental variables, namely notch geometry, flow Mach number and viscous effects (Reynolds number and boundary layer thickness ratio) could be established.
3) A strong effect due to flow separation from the walls of v-shaped notches on the over-all flow configuration and drag forces (form drag and friction drag) was observed.
4) The effect of the approaching boundary layer can be discussed in two categories, namely, thin or thick, depending on the degree to which the notch angle influences the value of the drag coefficient.

5) Reynolds number effects were generally small due to the large contribution of the free shear layer phenomena.
6) Supersonic flow past v-notches with relatively thin approaching boundary layers can be analyzed on the basis of a simplified flow model accounting for the reduction in form drag by introducing information on the penetration depth ratio.
7) Drag values obtained for transonic flow show an anomolous behavior near Mach number of unity in as much as they reach maximum values at slightly supersonic Mach numbers. This was found however, to be rationally explained by the "self adjusting" configuration of the separation region.
8) Theoretical analysis of the drag of shallow v-notches in the transonic flow regime using empirical information on the penetration depth ratio resulted in good quantitative agreement with measured values.
9) The transonic parameters $\mathcal{J}$ and $\mathcal{K}$ are reasonable correlating quantities in the transonic flow regime for v-shaped notches.
10) The separation point inside of the v-shaped notch adjusts itself near Mach number equal to one resulting in an effective geometry change which reduces the expected notch drag coefficient.

Recommendations for future investigations in this area include the following:

1) Conduct drag coefficient investigations in the Mach number range between one and two, including further investigation of notch angle effects in this region.
2) Extend investigation of the effect of the ratio of the momentum thickness to notch length to smaller values.
3) A more complete investigation of the downstream effects on the drag coefficient for v-shaped notches.
4) Extend the objectives of the present investigation to non-symmetrical v-shaped notches.
5) Extend the range of the Reynolds number investigation by an order of magnitude.
6) Utilize the drag balance for a large variety of direct force measurements, such as those related to intakes with non-zero flow rates.

LIST OF SYMBOLS

a = velocity of sound

A = area or empirical boundary layer coefficient

$\bar{A}$ = total clearance area around perimeter of model

b = width of plate

B = bending moment

C = Crocco number, velocity/maximum velocity

C_d = drag force/ $\frac{1}{2}\rho_e u_e^2 bL$

C_f = wall shear stress/ $\frac{1}{2} u_e^2 \rho_e$

C_F = drag force/ $\frac{1}{2}\rho_e u_e^2 A$

C_{wave} = partial drag component in supersonic flow

C_{trav} - partial drag component in subsonic and supersonic flow

d = vertical distance to separation point

$\bar{d}$ = flat plate clearance between plate and base

D = drag force

DF = drag function

E = modulus of elasticity

F = drag force on plate of finite length

G = leakage flow rate

h = notch depth

H = boundary layer shape parameter, δ^*/θ

I_{2j} = integral of a function of ϕ with respect to η

I = moment of inertia

J = shear stress function

$\mathcal{J}$ = transonic similarity parameter

$\mathcal{K}$ = transonic similarity parameter
k = ratio of specific heats
$\bar{K}$ = calibration constant
L = plate length or notch length
l = length of strain beam
M = Mach number
N = empirical boundary layer exponent
p = pressure
P = pressure
r = depth of the notch or cavity
R = specific gas constant
Re_θ = momentum thickness Reynolds number
Re_x = length Reynolds number
s = stress at outer fiber
t = thickness of the strain beam
$\bar{t}$ = time
T = temperature
U = free stream velocity in x-direction
u = velocity component in x-direction
$\bar{V}$ = volume
V = voltage
v = velocity component in y-direction
w = width of the strain beam
x = coordinate along the plate or notch surface
y = coordinate normal to the plate or notch surface

$\bar{y}$ = deflection of cantilever beam

z = coordinate in direction of force on a cantilever beam

$\alpha(N)$ = empirical boundary layer constant

β = exponent in viscosity temperature relation, 0.75 for air

δ = boundary layer thickness

δ^* = boundary layer displacement thickness

δ_z = boundary layer thickness at separation

ϵ = strain

η_P = position parameter

Ω = notch angle

ψ = dimensionless x-distance

ν = kinematic viscosity

μ = dynamic viscosity

ϕ = velocity ratio, u/u_e

ρ = density

τ = shear stress

θ = boundary layer momentum thickness

$\Delta\theta$ = difference in boundary layer momentum thickness

Subscripts

e = free stream condition

1 = first point along a flat plate

2 = second point along a flat plate

o = stagnation conditions

i = incompressible fluid

d = downstream

u = upstream

n = notch

j = dividing streamline

$\Omega = 10°$ $M_e = 1.96$ $\delta_1 = 0.18''$

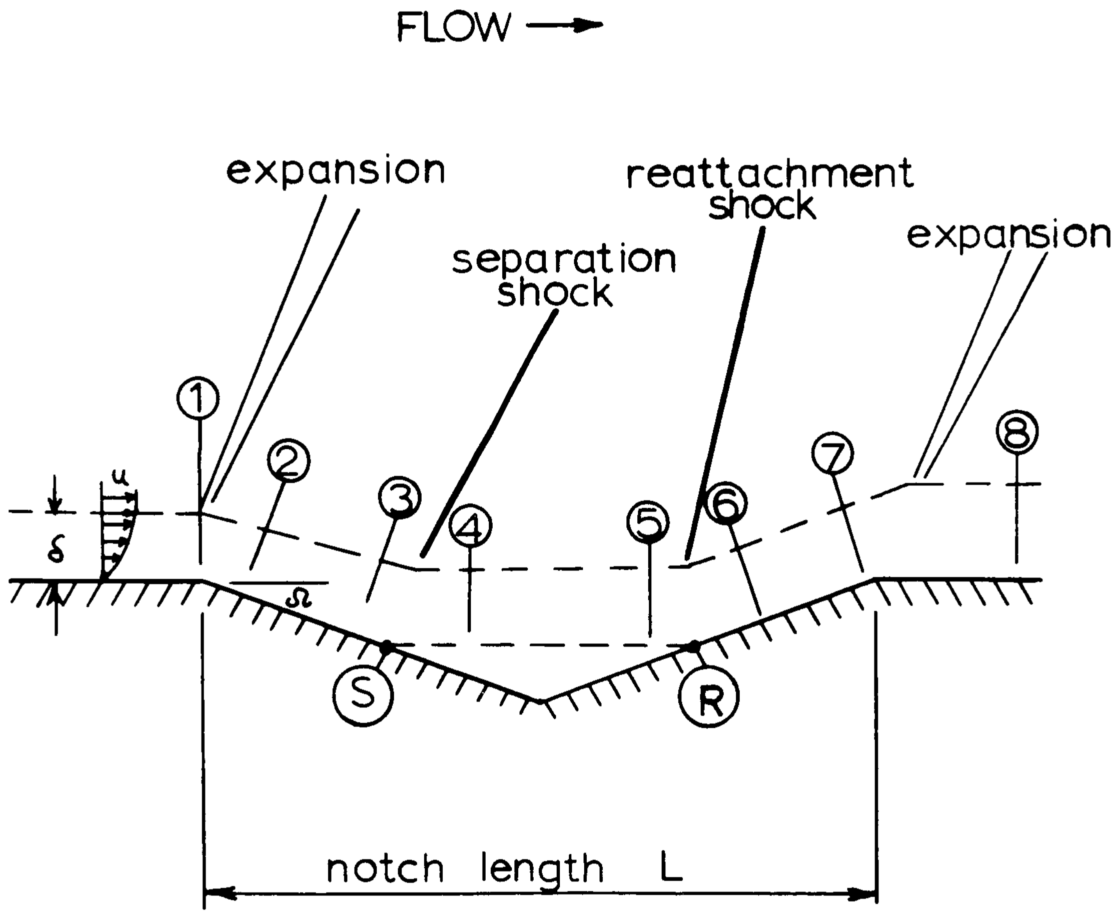
FLOW →
expansion
reattachment shock
separation shock
expansion
u
δ
Ω
①
②
③
④
⑤
⑥
⑦
⑧
Ⓢ
Ⓡ
notch length L

Figure 1. Theoretical Supersonic Flow Model

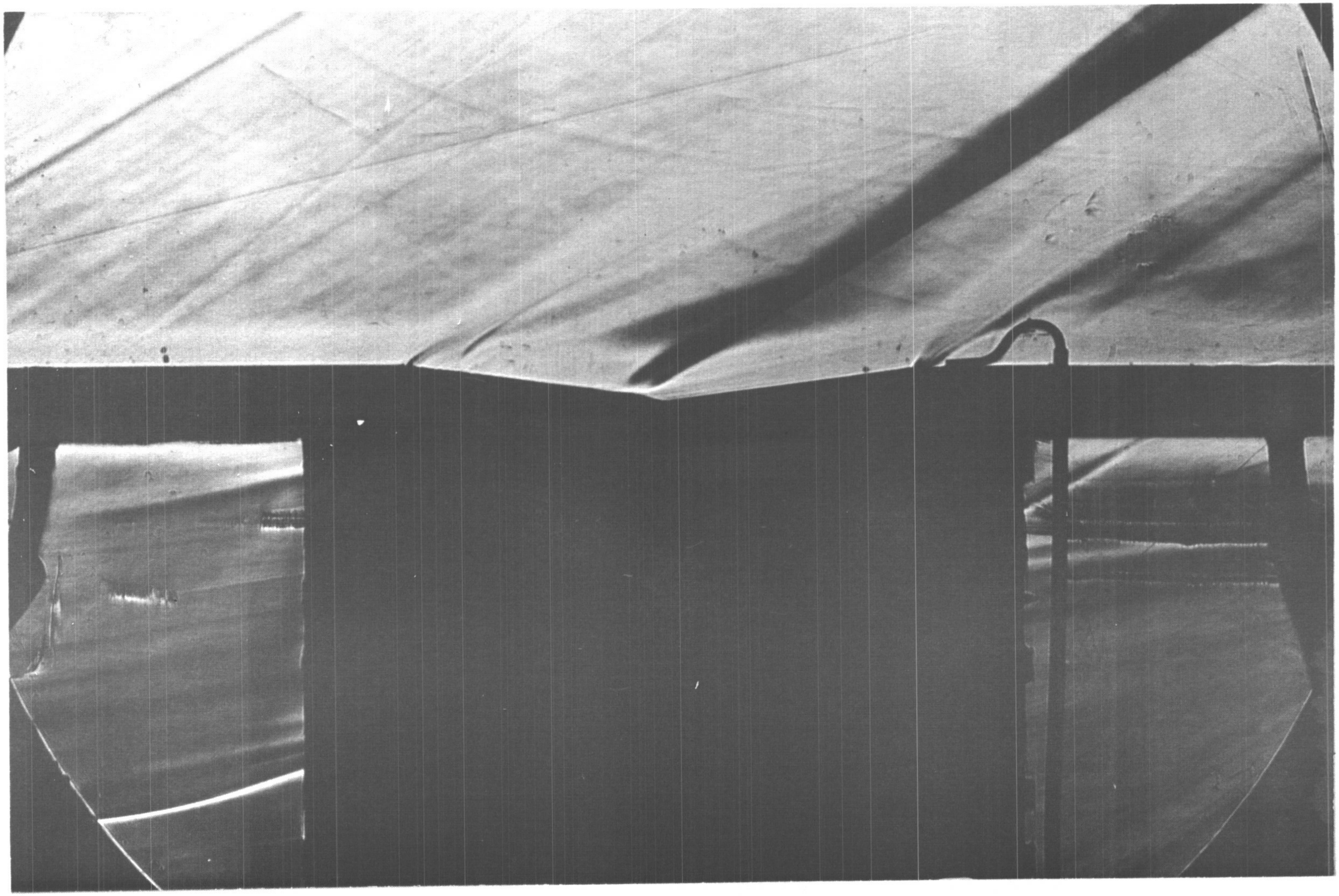

Figure 2. Supersonic Notch Flow (M_e=1.96, Ω = 7° , L = 2")

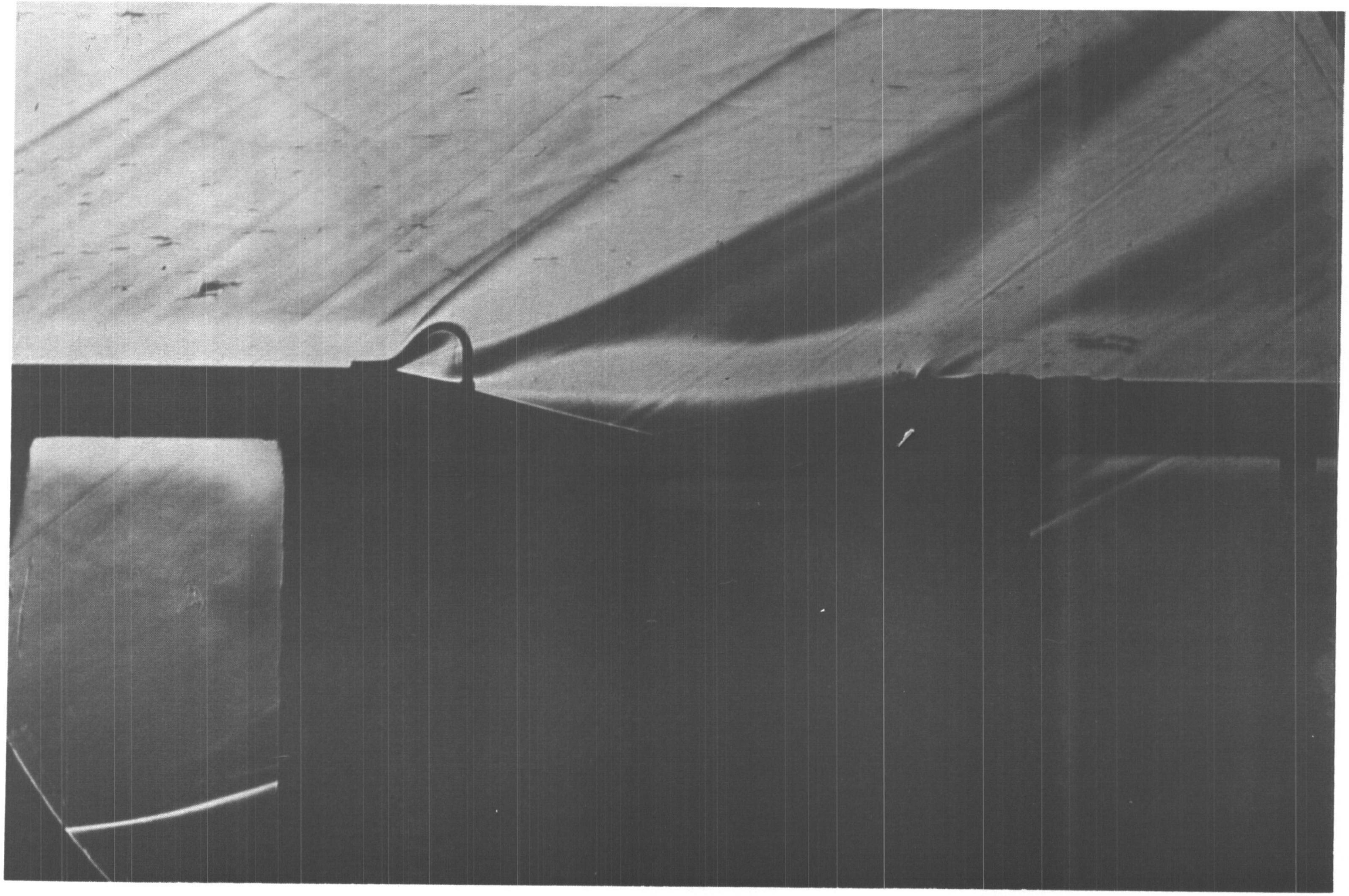

Figure 2. (continued.) ($M_e = 1.96$, $\Omega = 13°$, $L = 2''$)

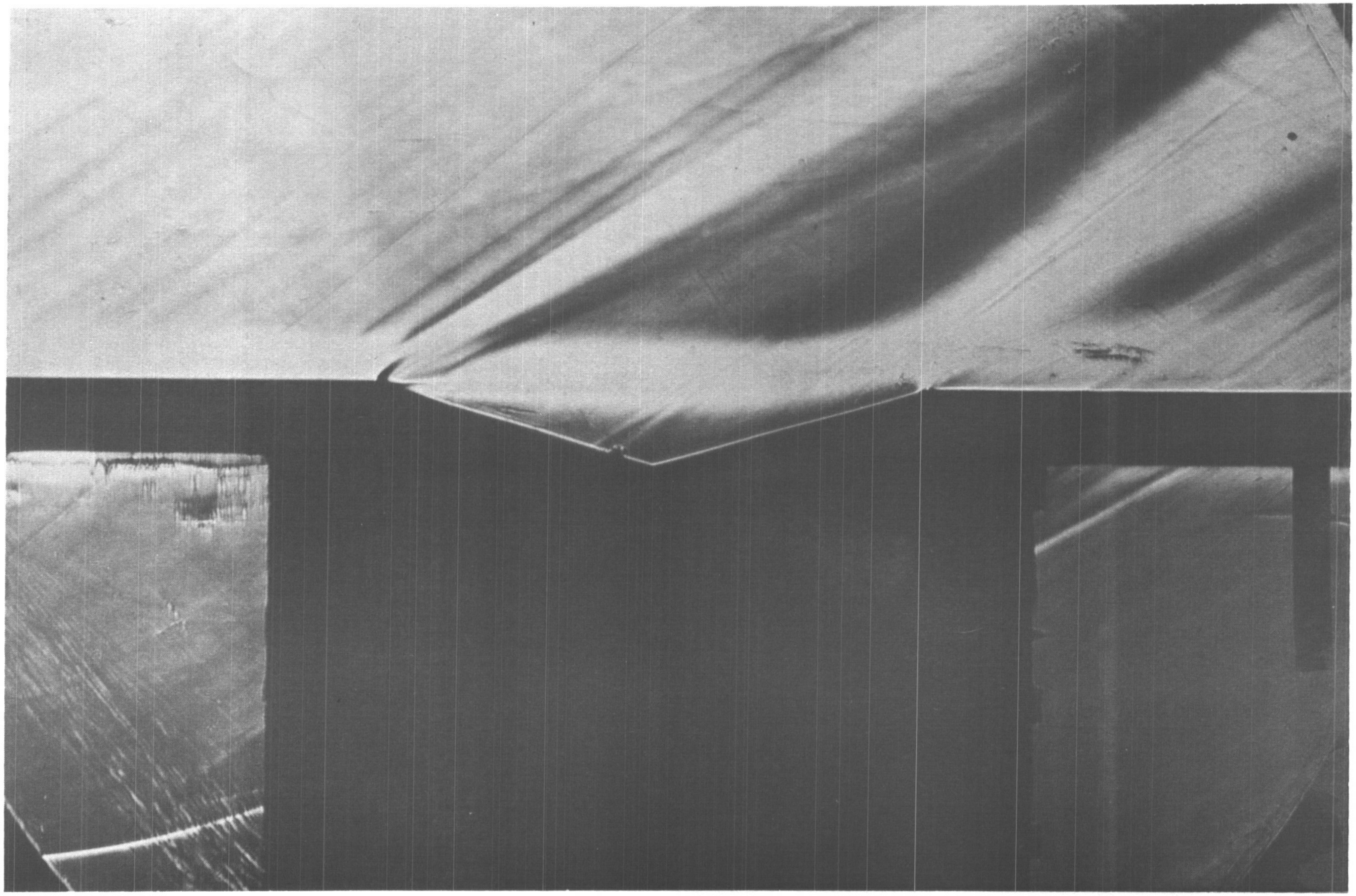

Figure 2. (concluded.) (M_e=1.96, Ω=16°, L=2")

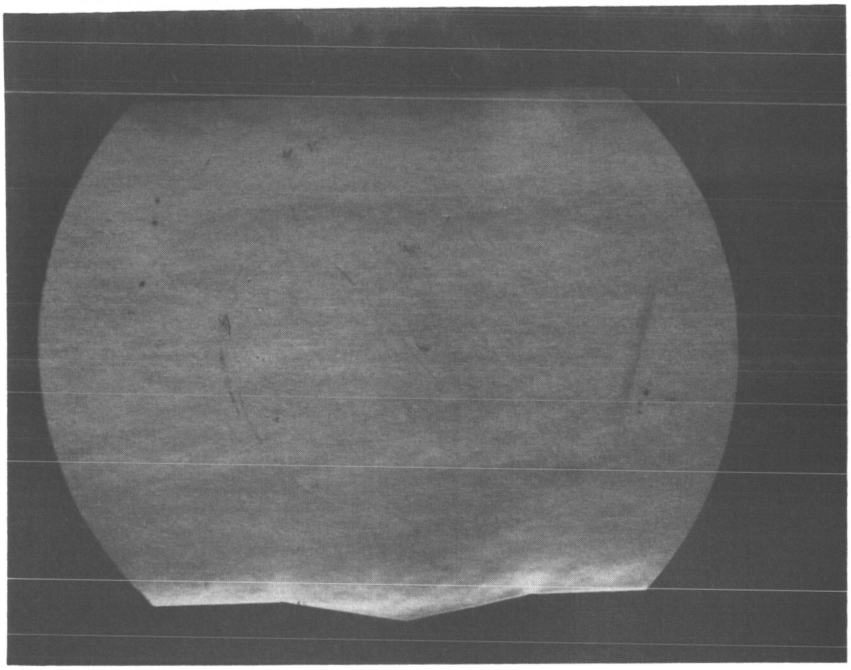

(a) $M_e = 0.6$, $L = 2''$, $\Omega = 10°$

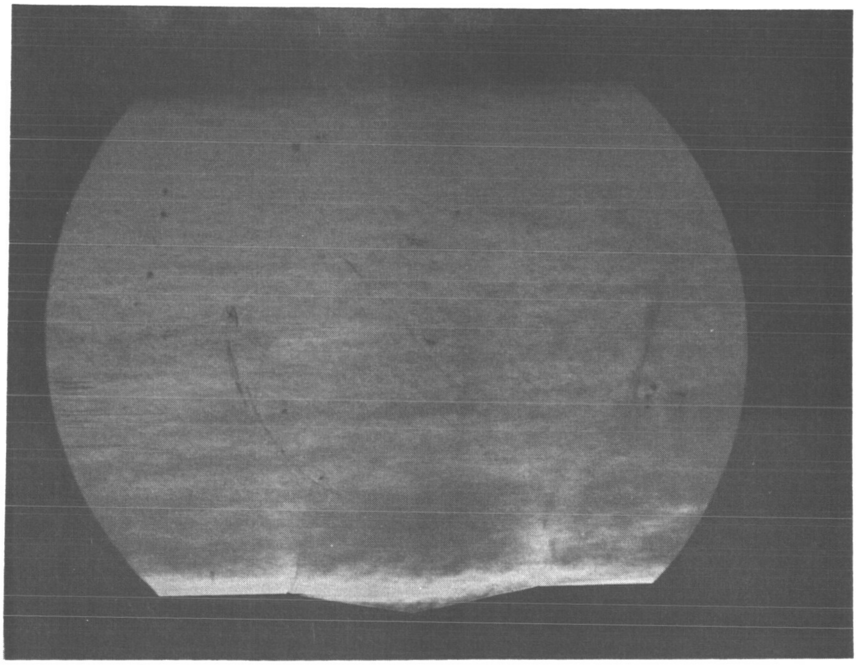

(b) $M_e = 0.9$, $L = 2''$, $\Omega = 10°$

Figure 3. Transonic Flow Over Notch

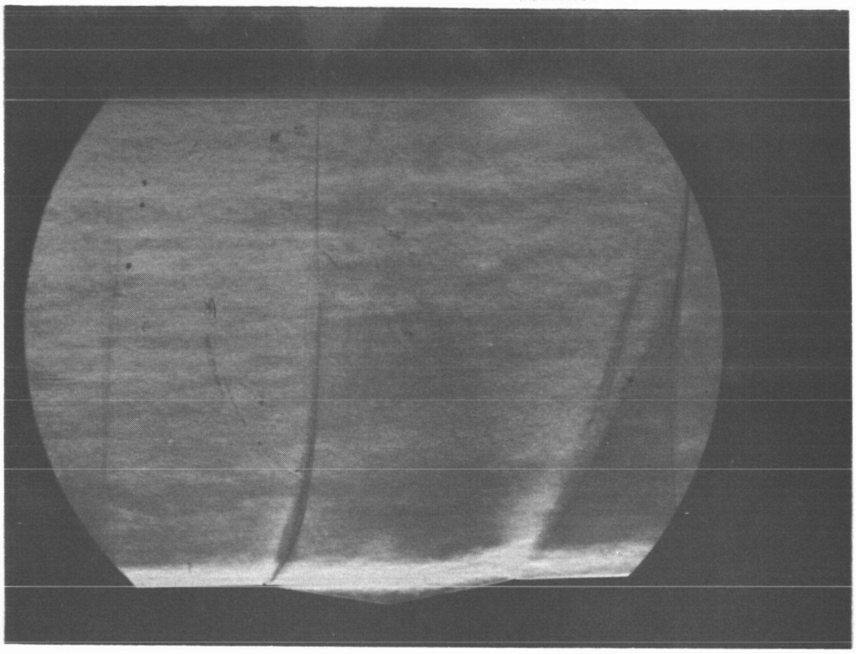

(c) $M_e = 0.98$, $L = 2''$, $\Omega = 10°$

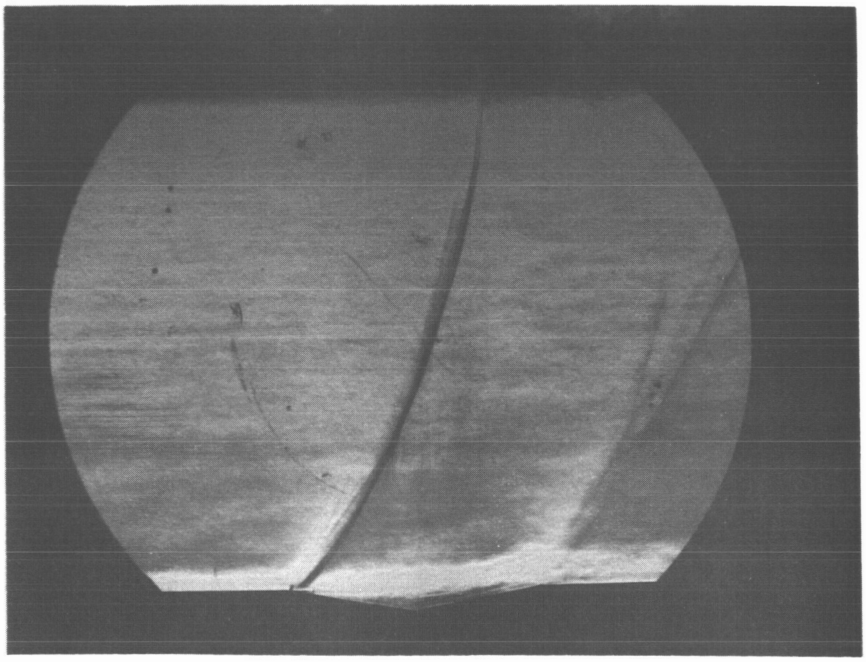

(d) $M_e = 1.09$, $L = 2''$, $\Omega = 10°$

Figure 3. (concluded.)

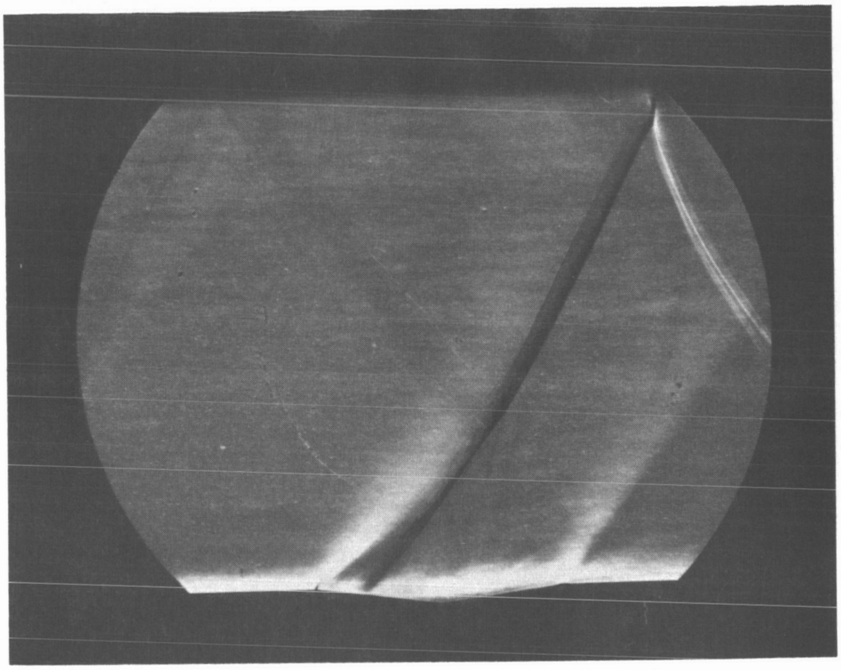

(a) $M_e = 1.14$, $L = 2''$, $\Omega = 7°$

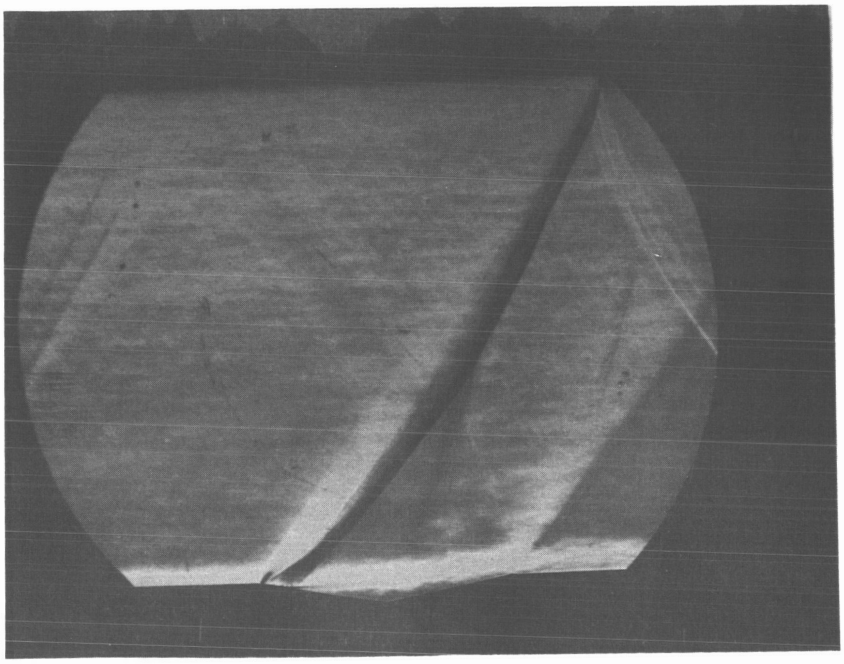

(b) $M_e = 1.14$, $L = 2''$, $\Omega = 10°$

Figure 4. Transonic Flow Over Notch

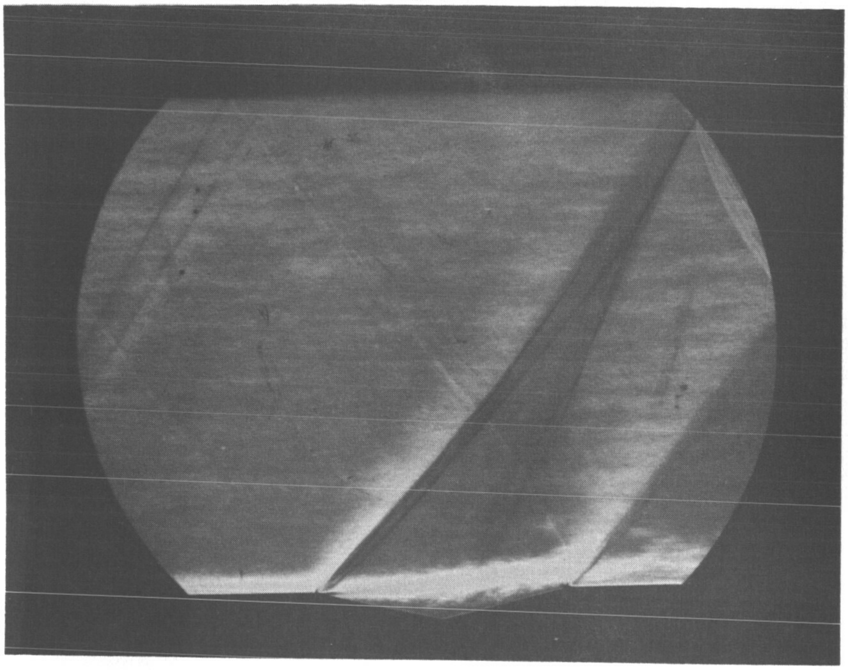

(c) $M_e = 1.14$, $L = 2''$, $\Omega = 13°$

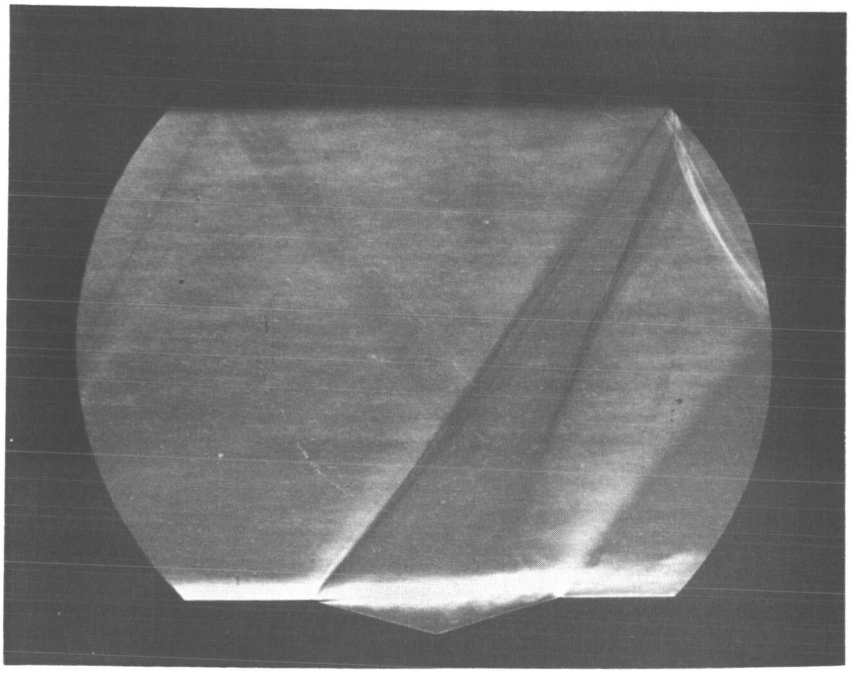

(d) $M_e = 1.14$, $L = 2''$, $\Omega = 16°$

Figure 4. (concluded.)

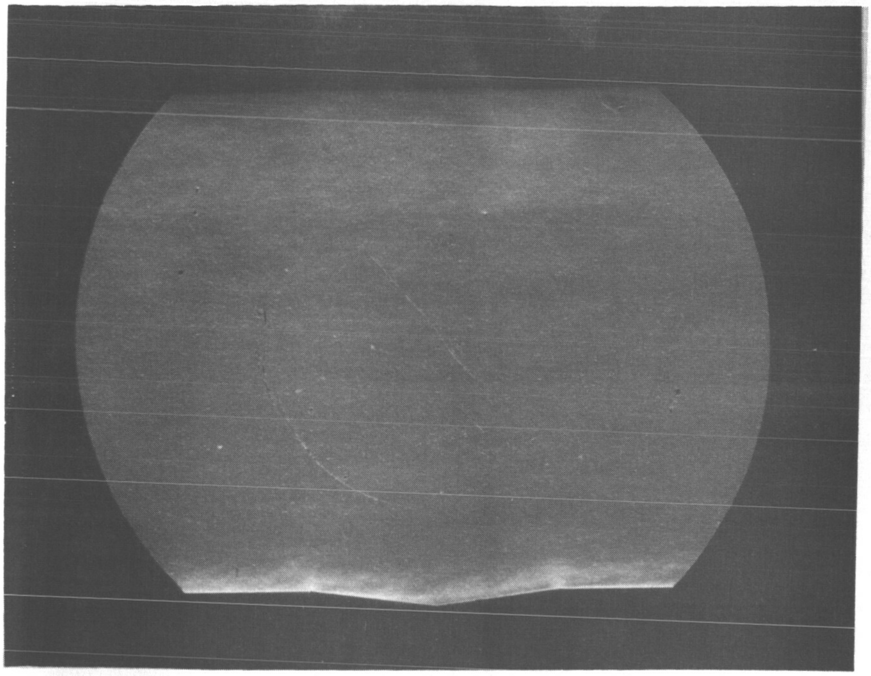

(a) $M_e = 0.61$, $L = 2''$, $\Omega = 7°$

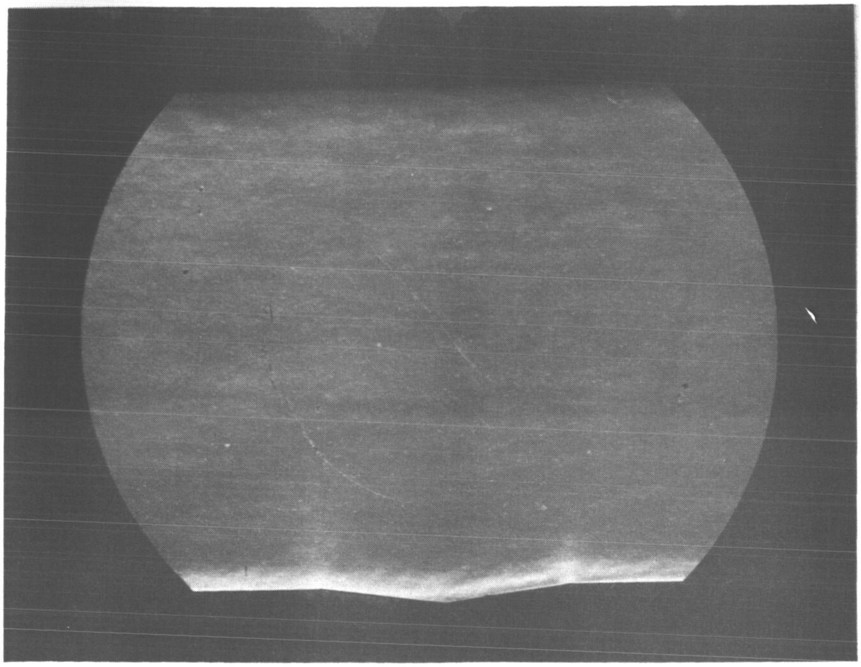

(b) $M_e = 0.83$, $L = 2''$, $\Omega = 7°$

Figure 5. Transonic Flow Over Notch

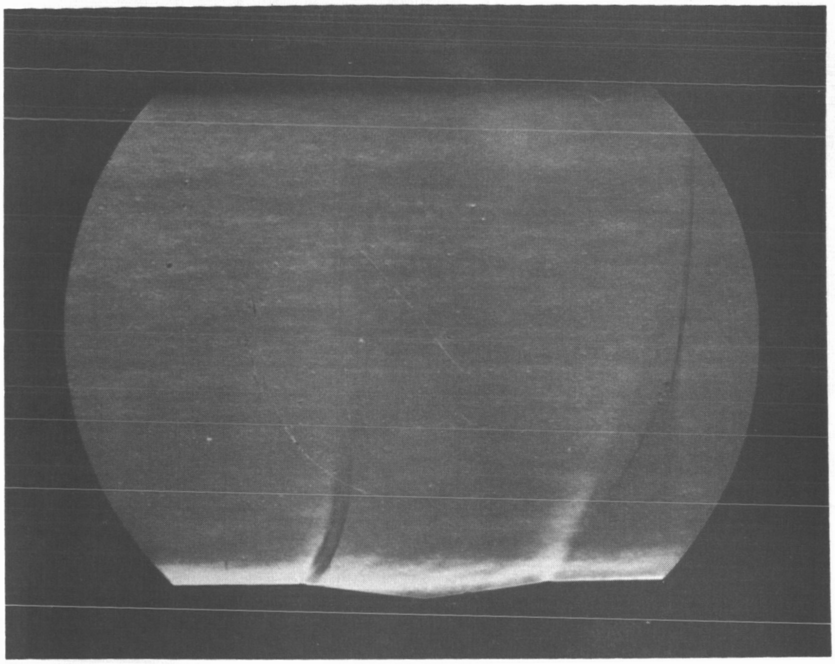

(c) $M_e = 0.99$, $L = 2''$, $\Omega = 7°$

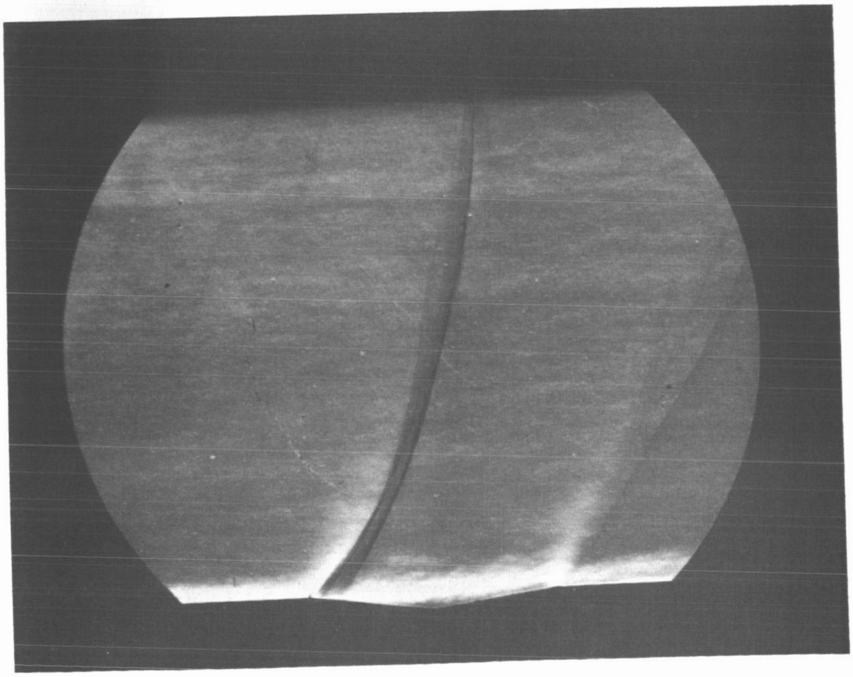

(d) $M_e = 1.09$, $L = 2''$, $\Omega = 7°$

Figure 5. (concluded.)

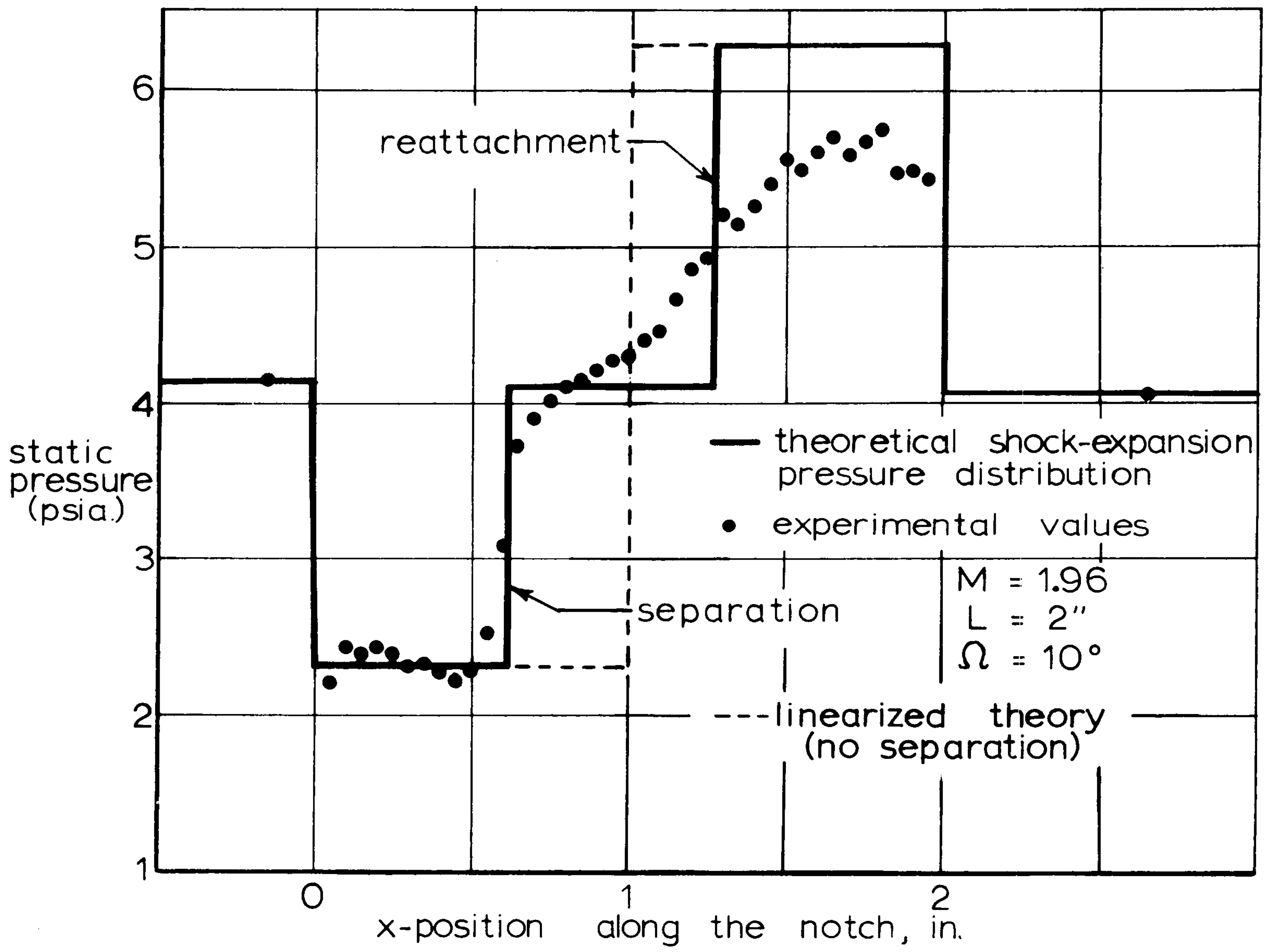

Figure 6. V-Notch Pressure Distribution

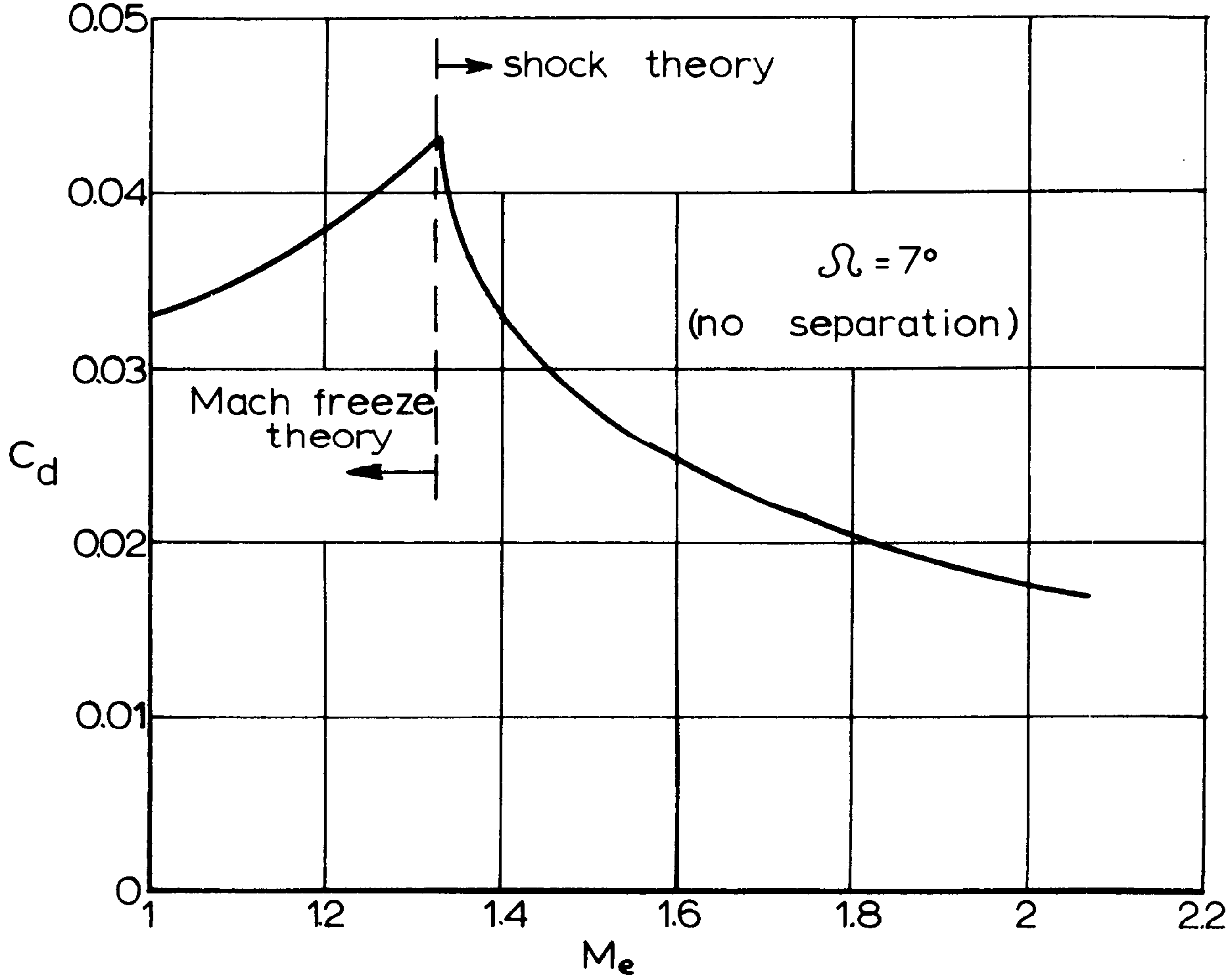

Figure 7. Transonic Flow Model C_d Variation

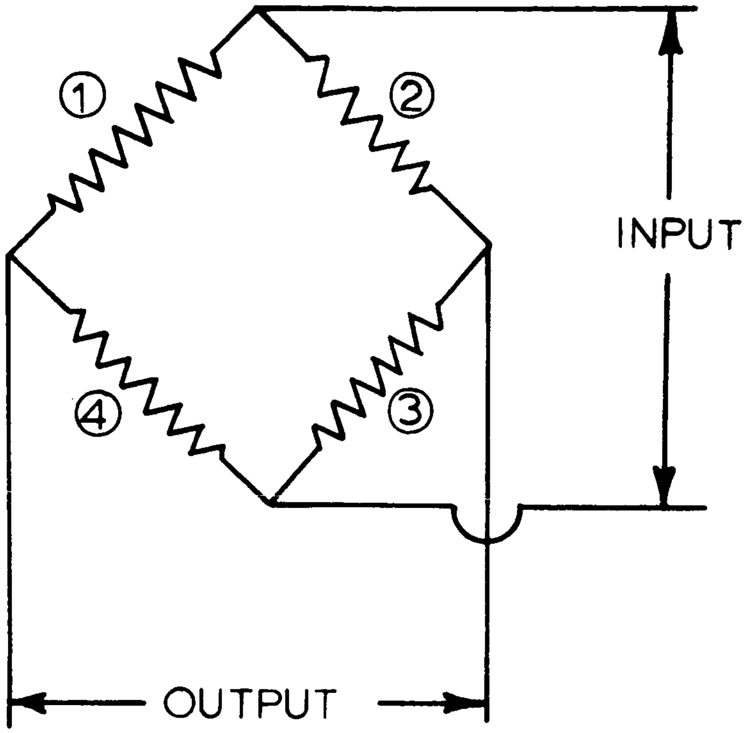
①
②
INPUT
④
③
OUTPUT

BRIDGE CIRCUIT

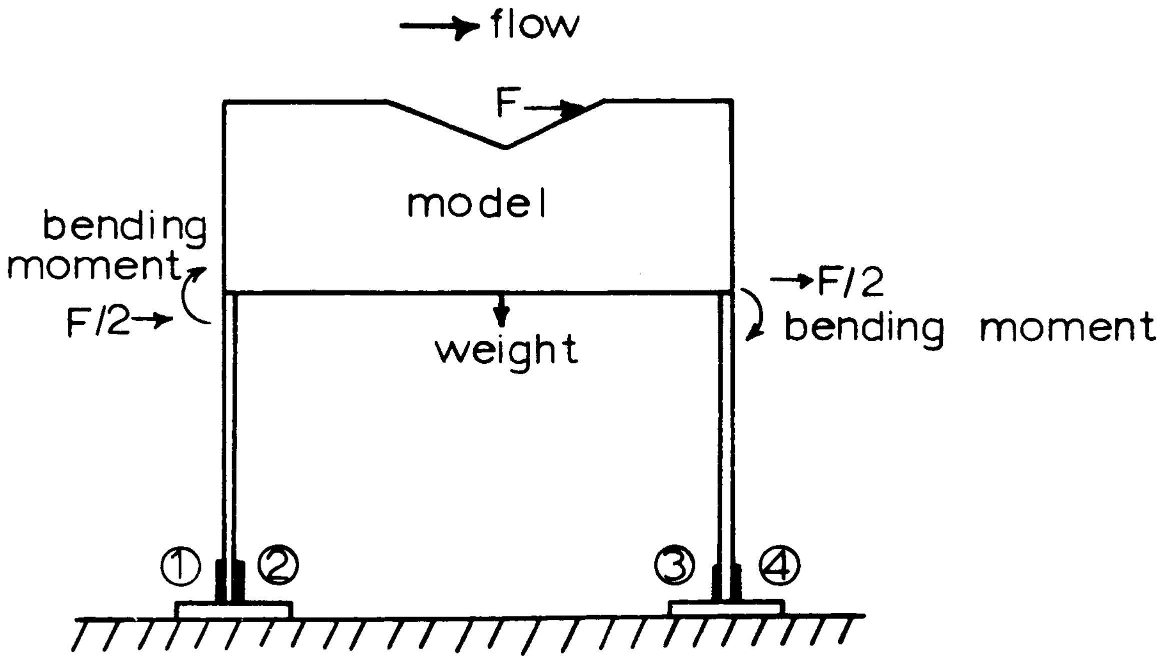
flow
F
model
bending moment
F/2
weight
F/2
bending moment
①
②
③
④

Figure 8. Drag Force Measurement Device

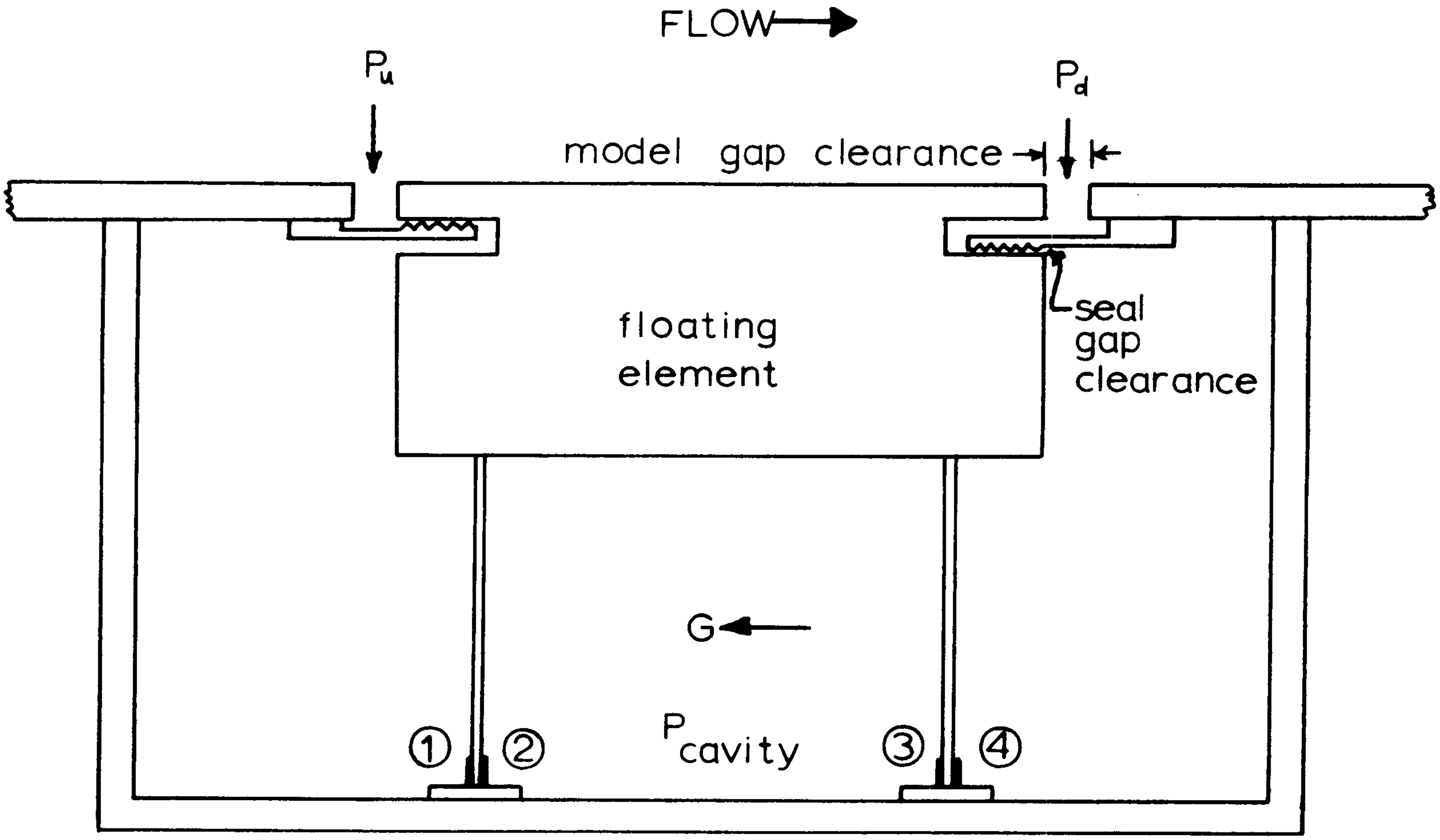
FLOW
P_u
P_d
model gap clearance
seal gap clearance
floating element
G
P_{cavity}
①
②
③
④

Figure 9. Diagrammatic Drawing of Drag Force Balance

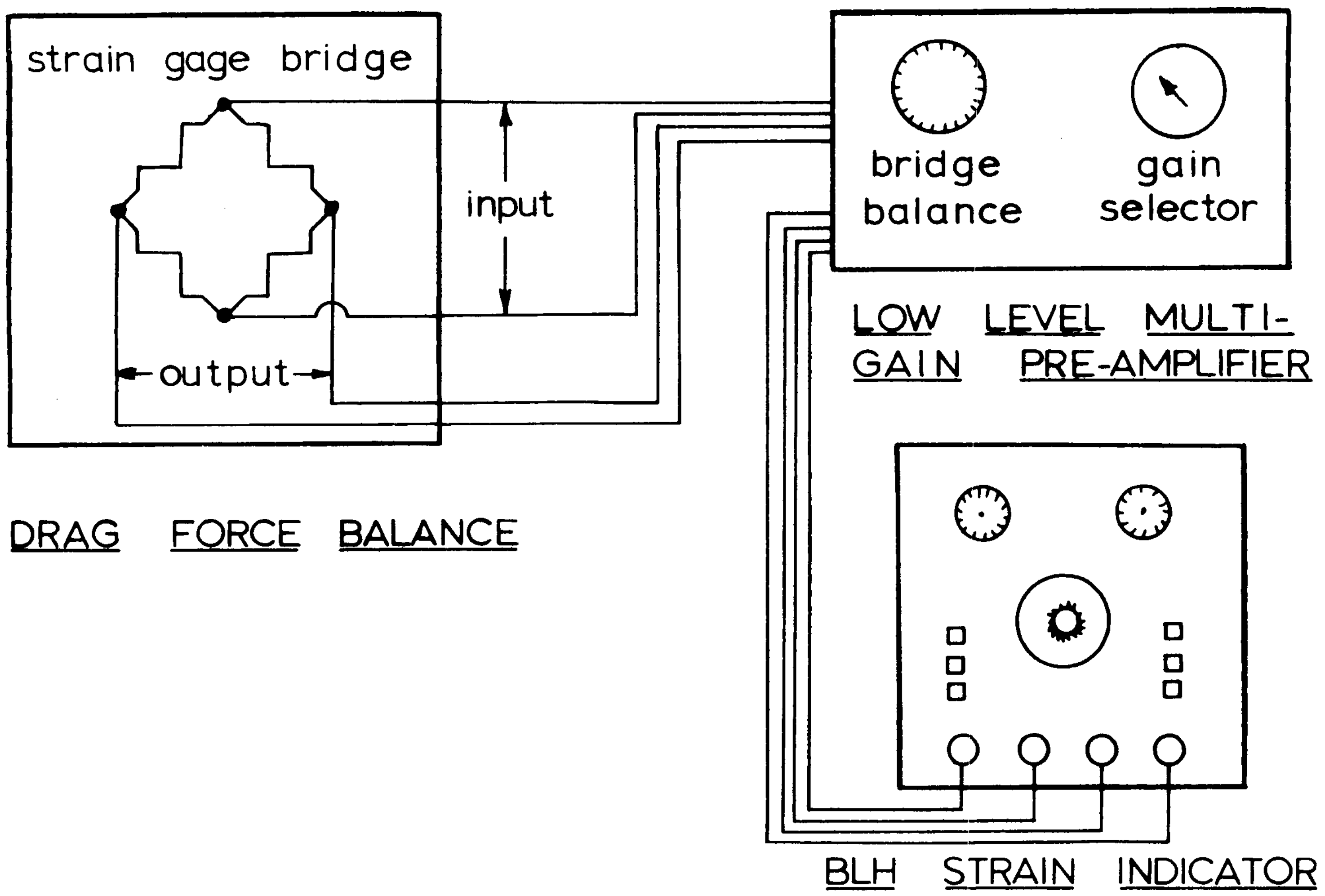
strain gage bridge
input
output
DRAG FORCE BALANCE
bridge balance
gain selector
LOW LEVEL MULTI-GAIN PRE-AMPLIFIER
BLH STRAIN INDICATOR

Figure 10. Drag Force Measurement System

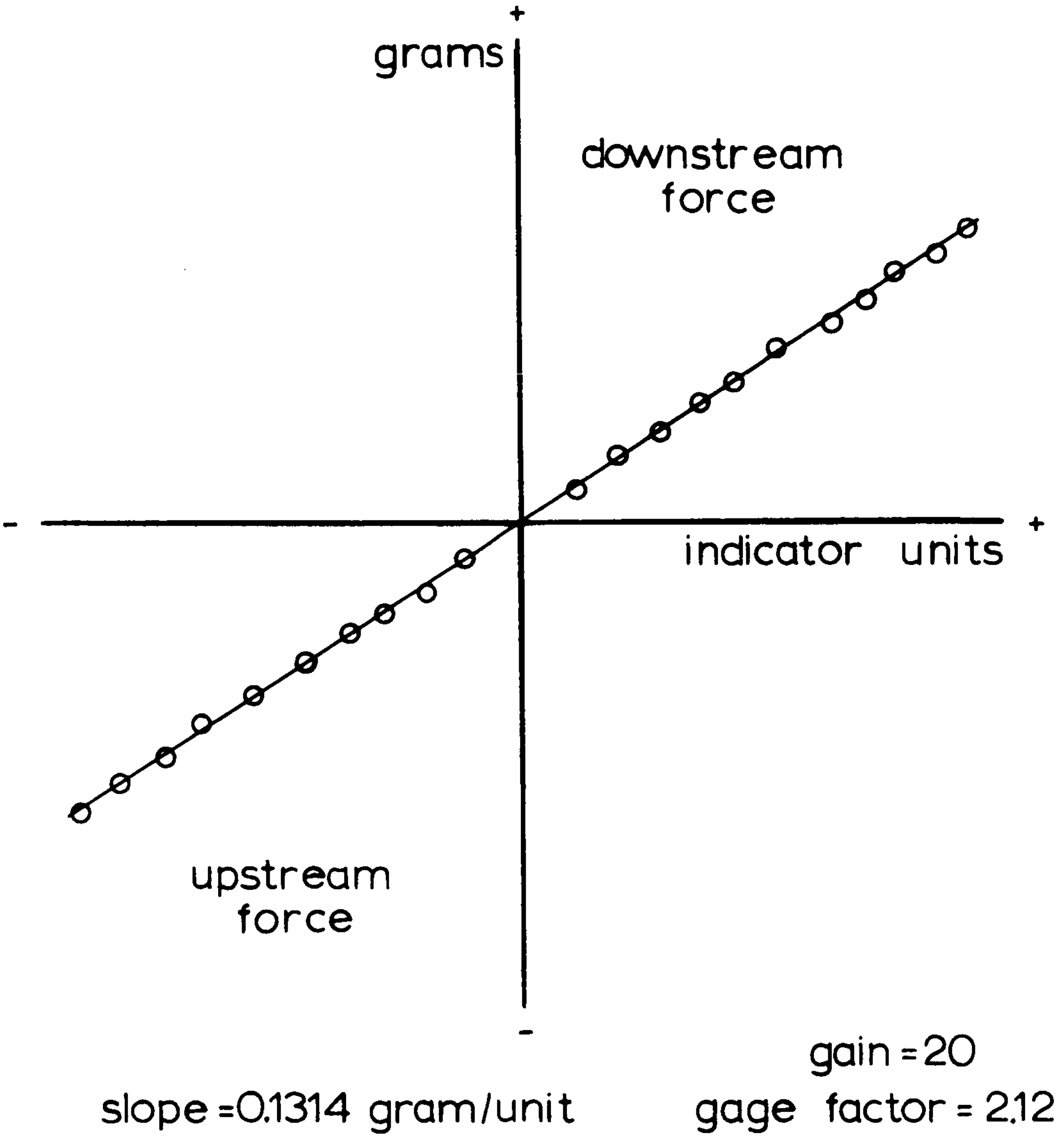

Figure 11. Drag Balance Calibration

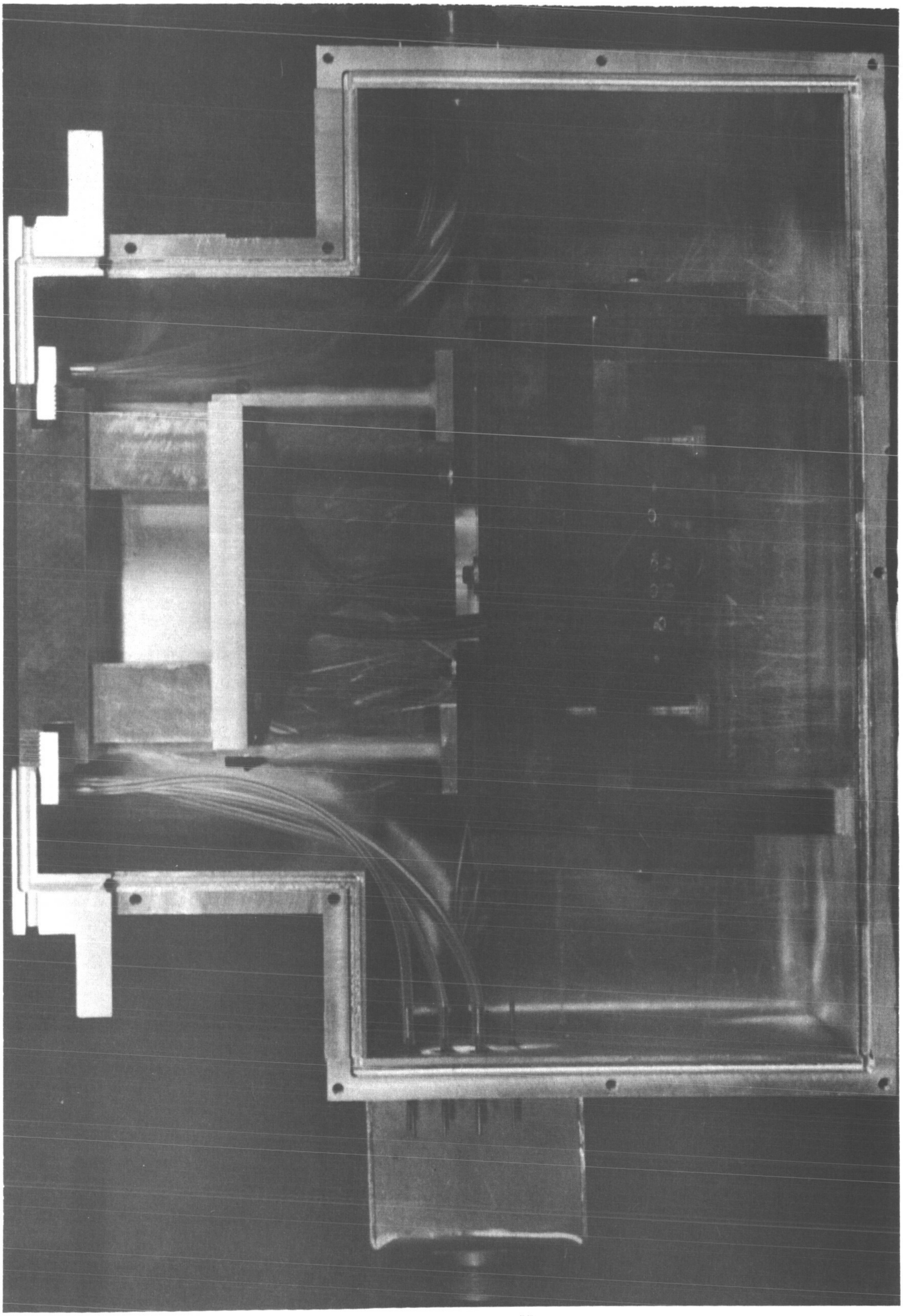

Figure 12. Drag Force Balance

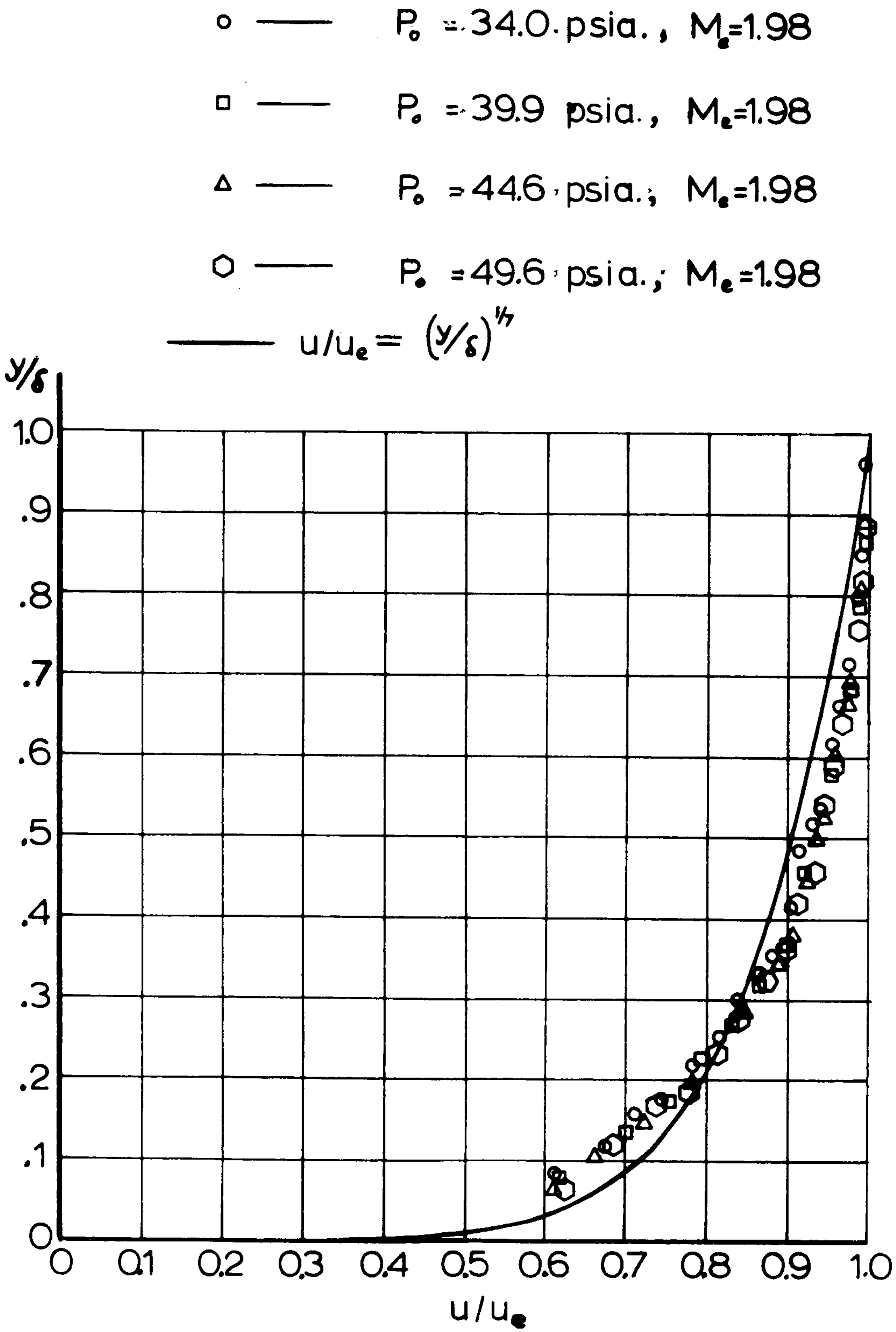

Figure 13. Turbulent Velocity Profiles

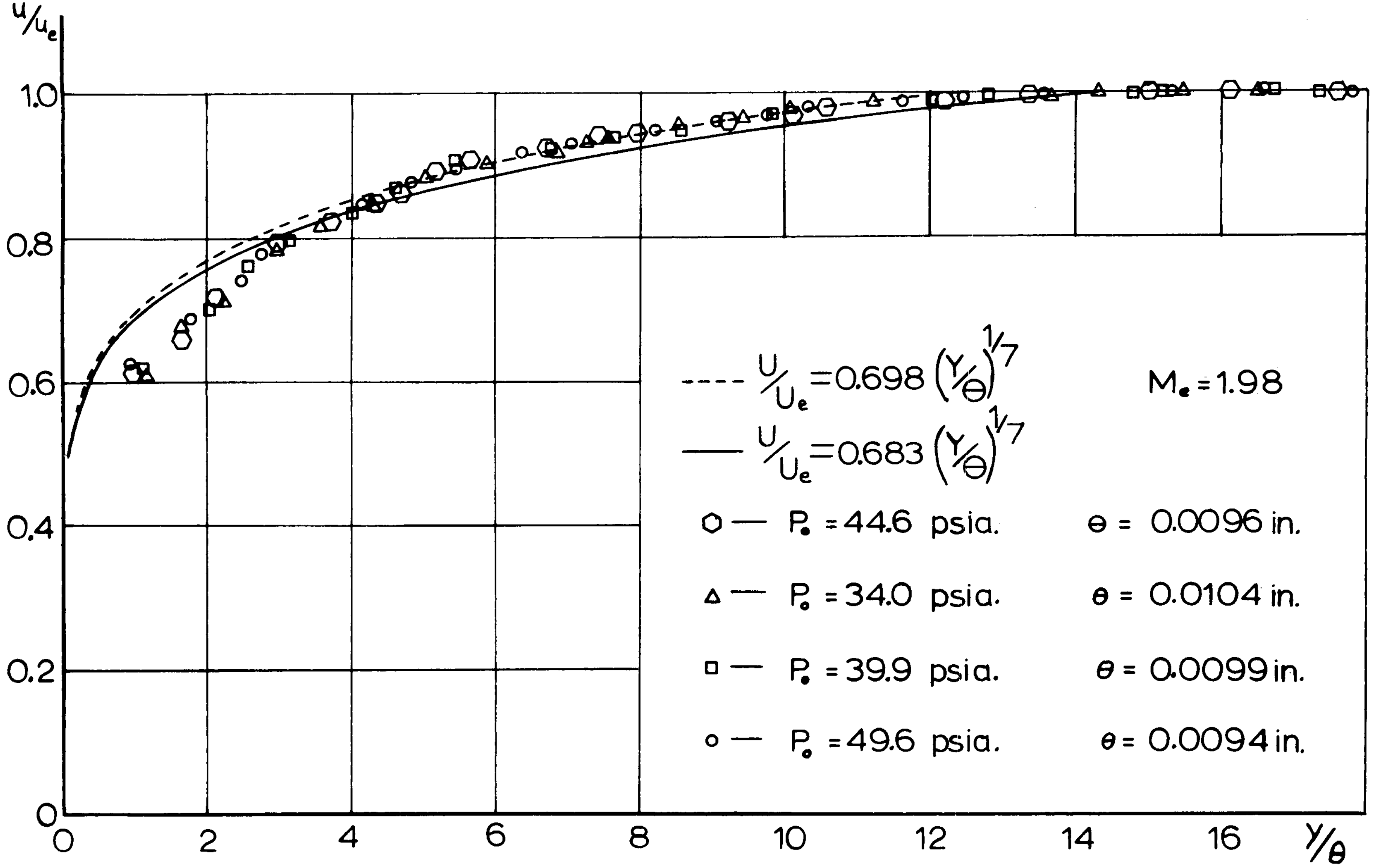

Figure 14. Supersonic Turbulent Velocity Traverses

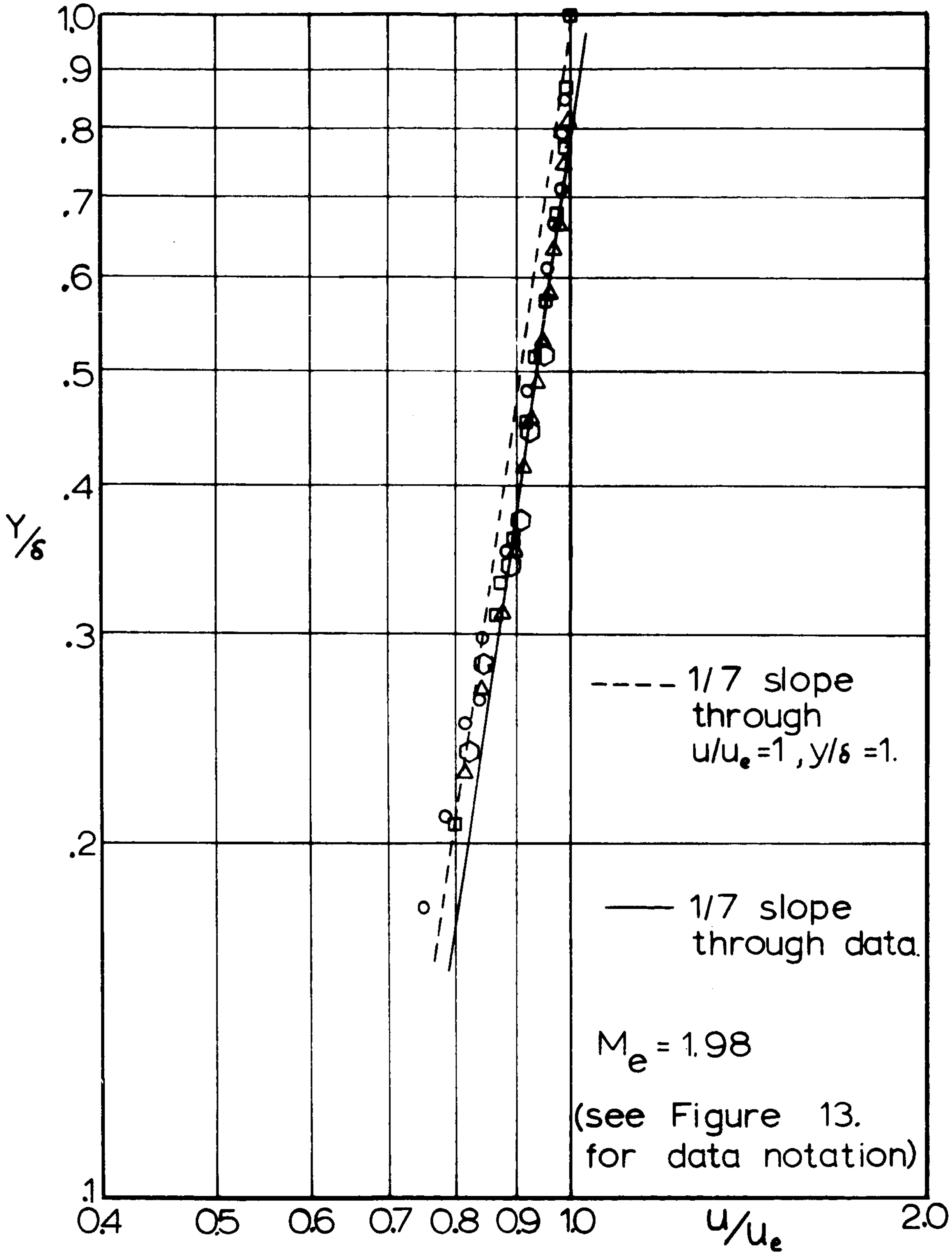

Figure 15. Supersonic Velocity Traverse Results

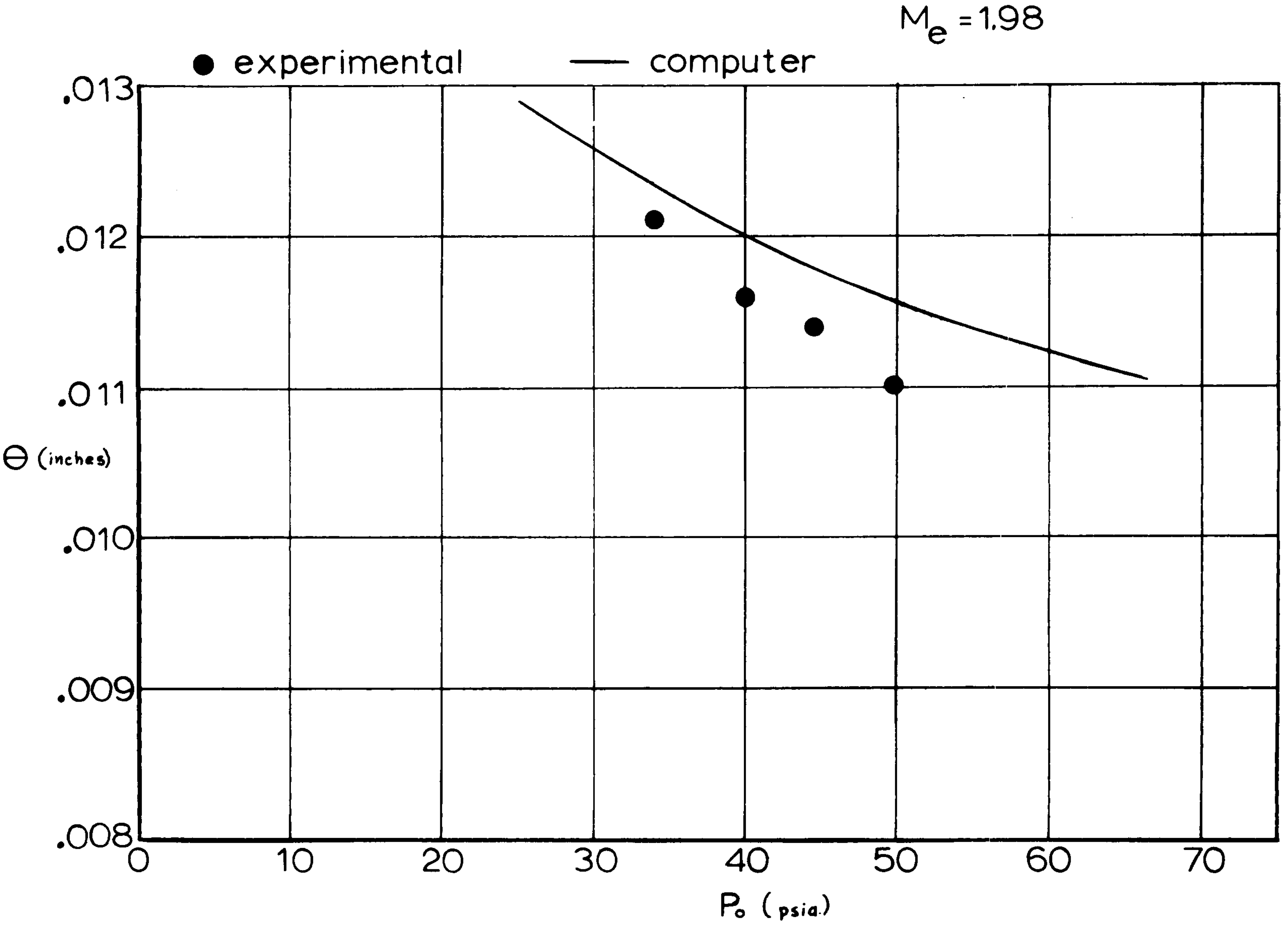

Figure 16. Supersonic Momentum Thickness

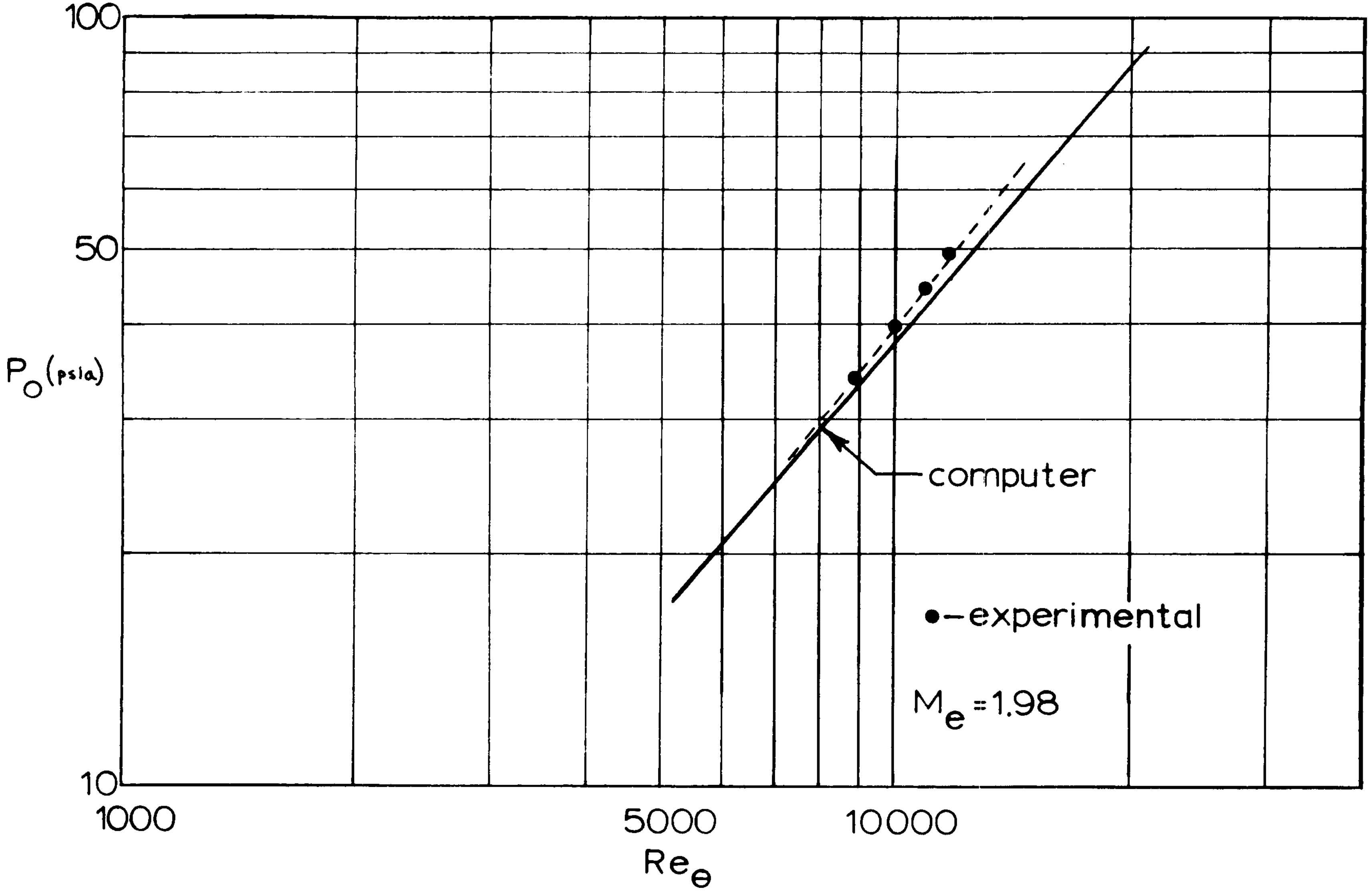

Figure 17. Momentum Thickness Reynolds Number

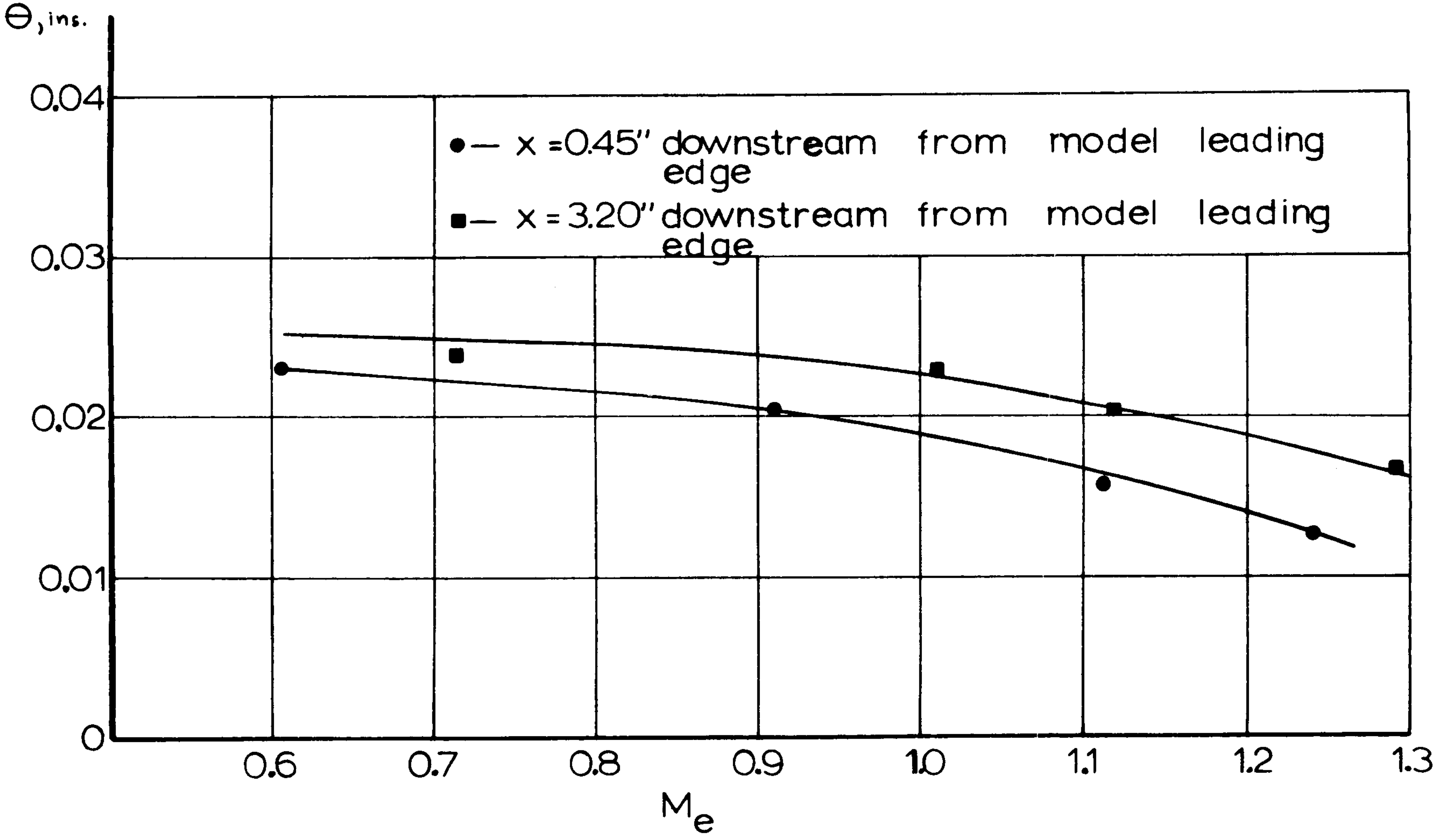

Figure 18. Transonic Momentum Thickness

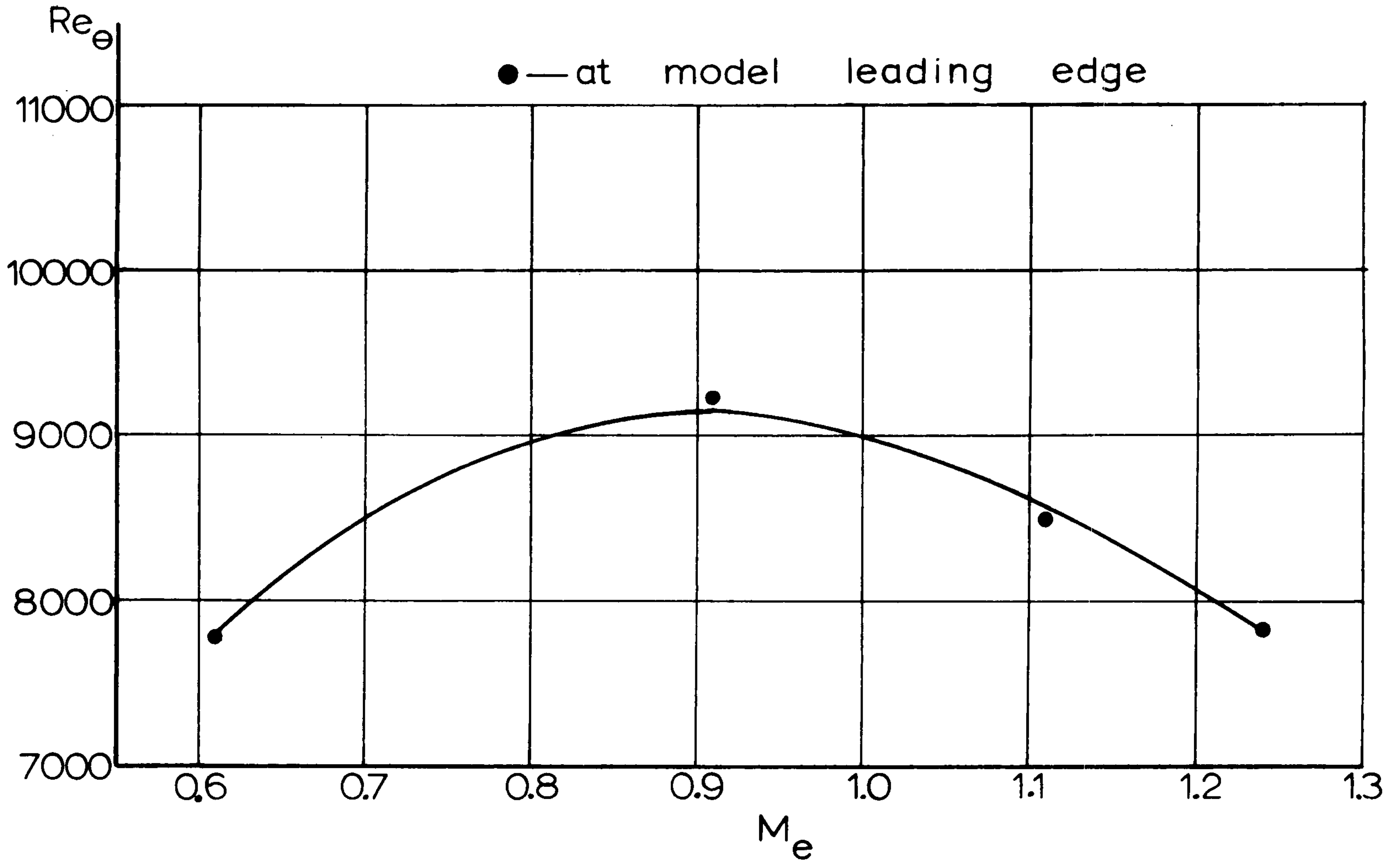

Figure 19. Transonic Momentum Thickness Reynolds Number

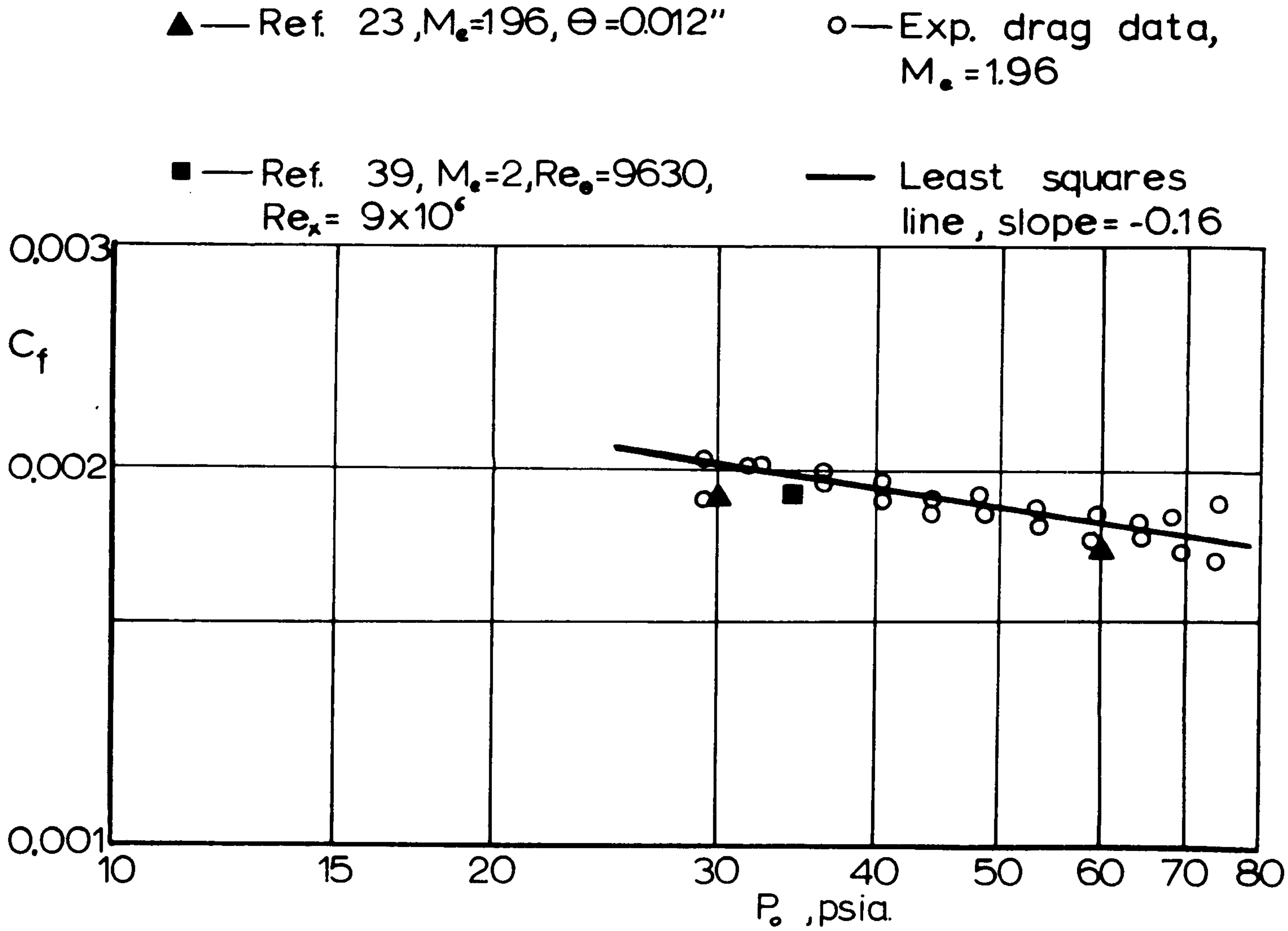

Figure 20. Local Flat Plate Friction Coefficient

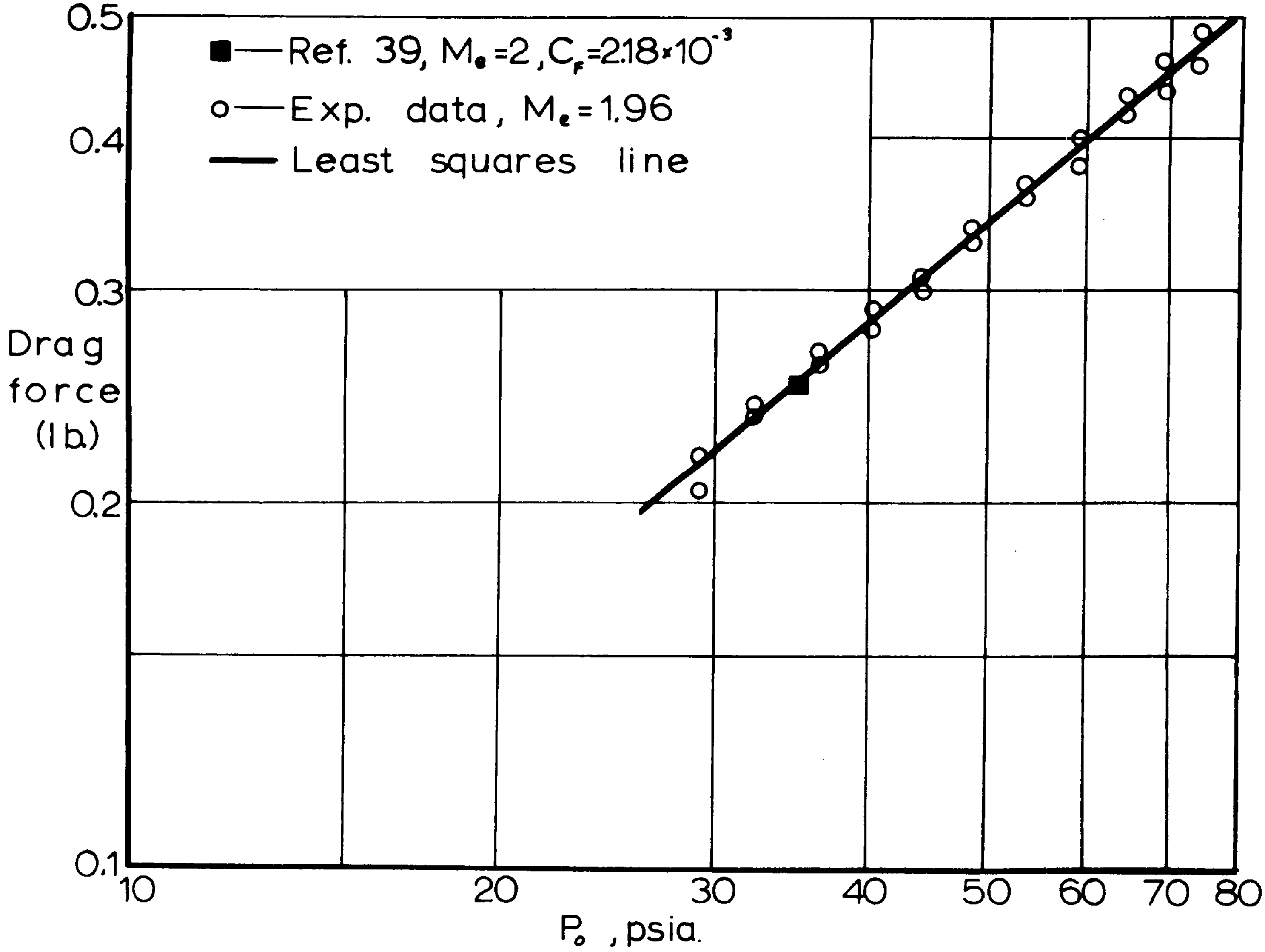

Figure 21. Total Drag on a Flat Plate

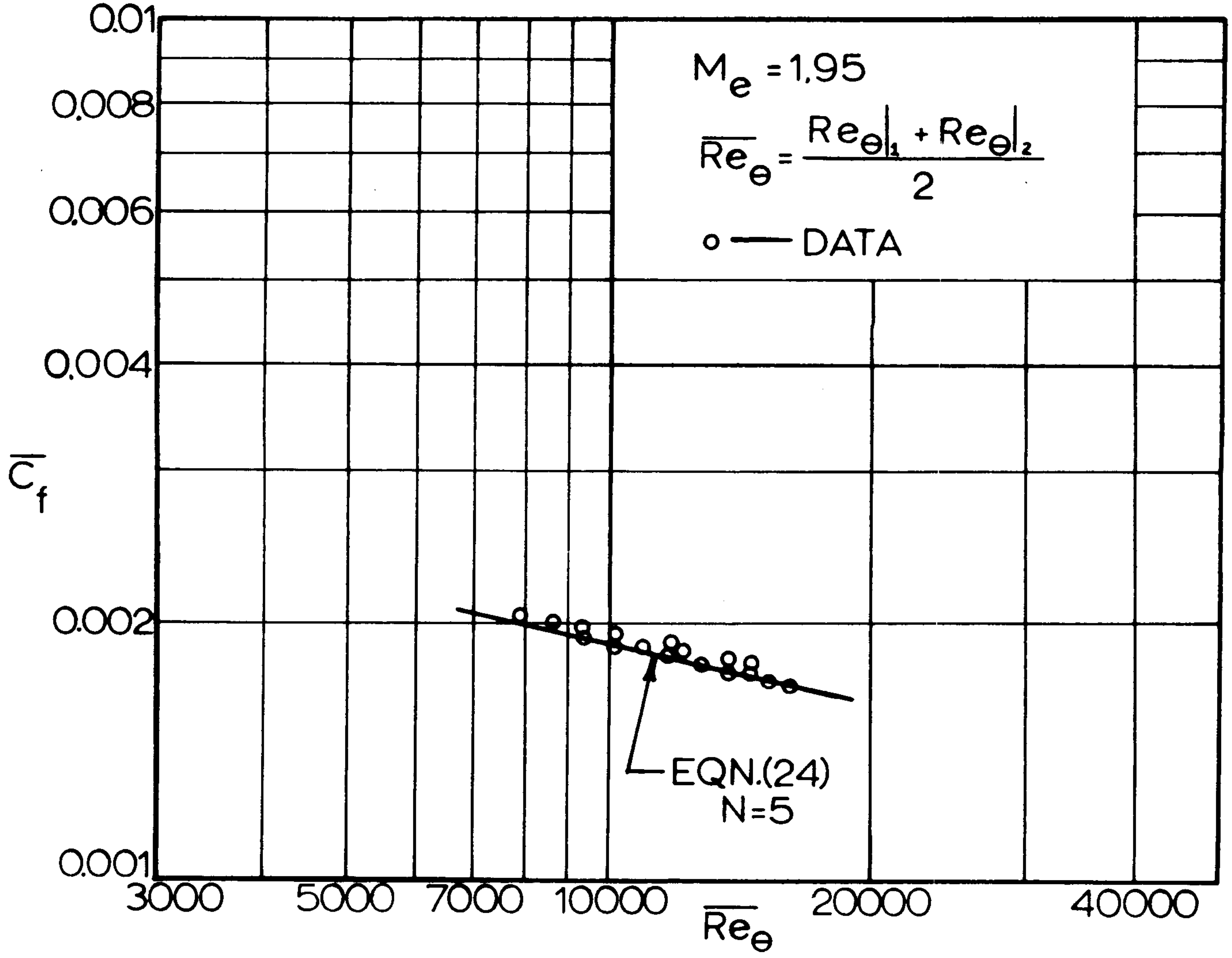

Figure 22. Average Drag Coefficient on a Flat Plate

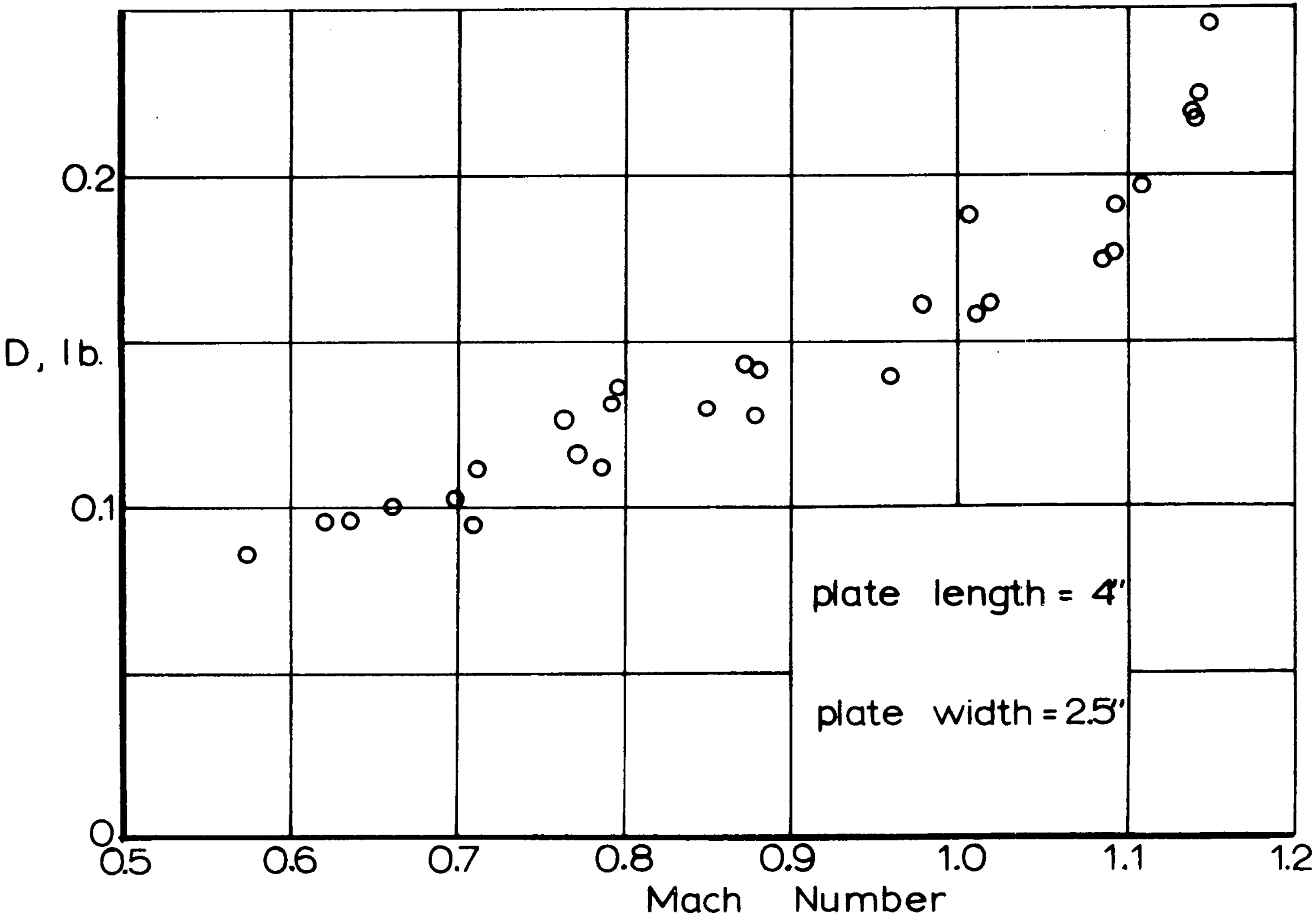

Figure 23. Experimental Transonic Drag Force on a Flat Plate

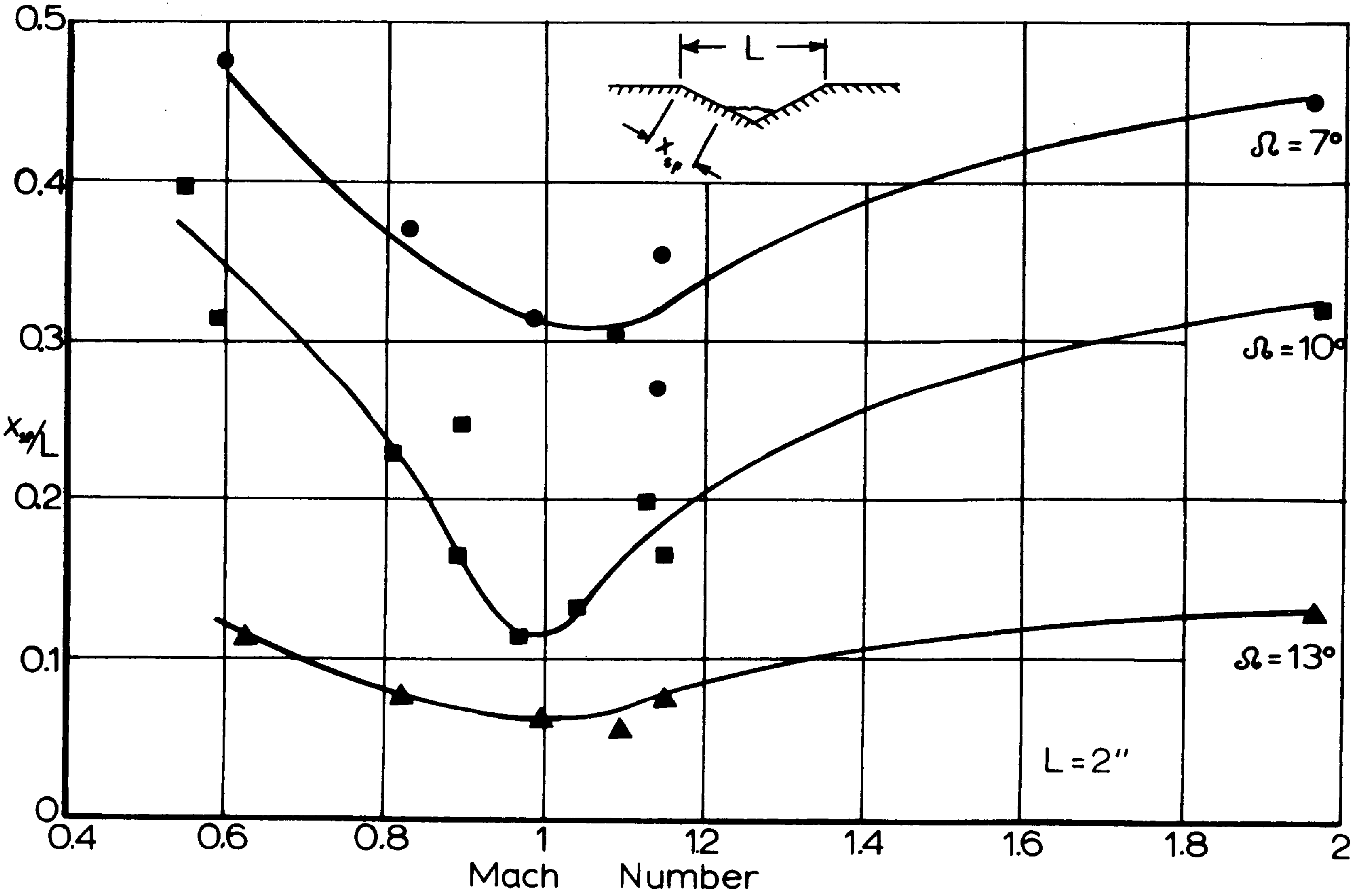

Figure 24. Self Adjustment of the Separation Point

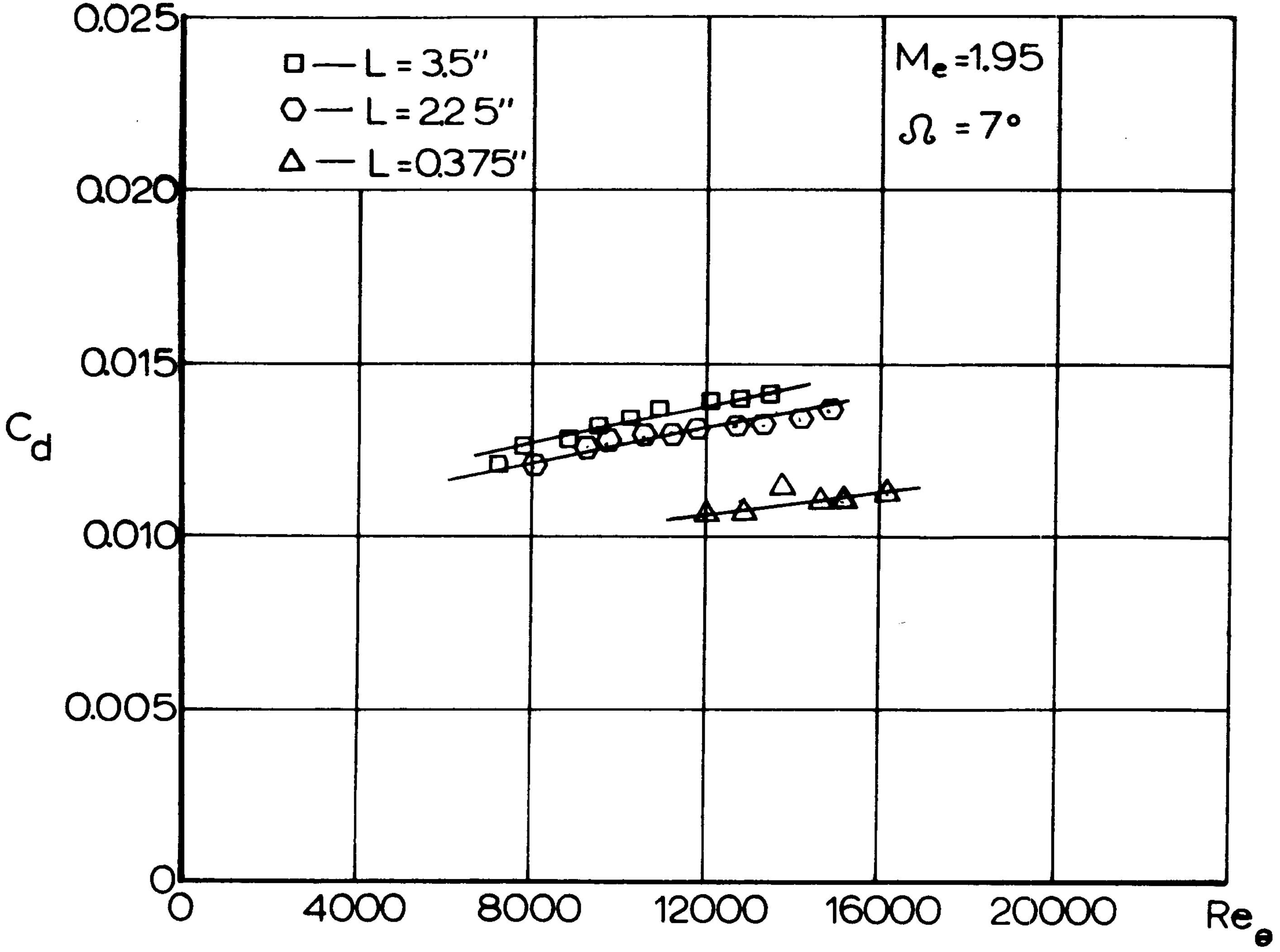

Figure 25. Supersonic Notch Drag Coefficients

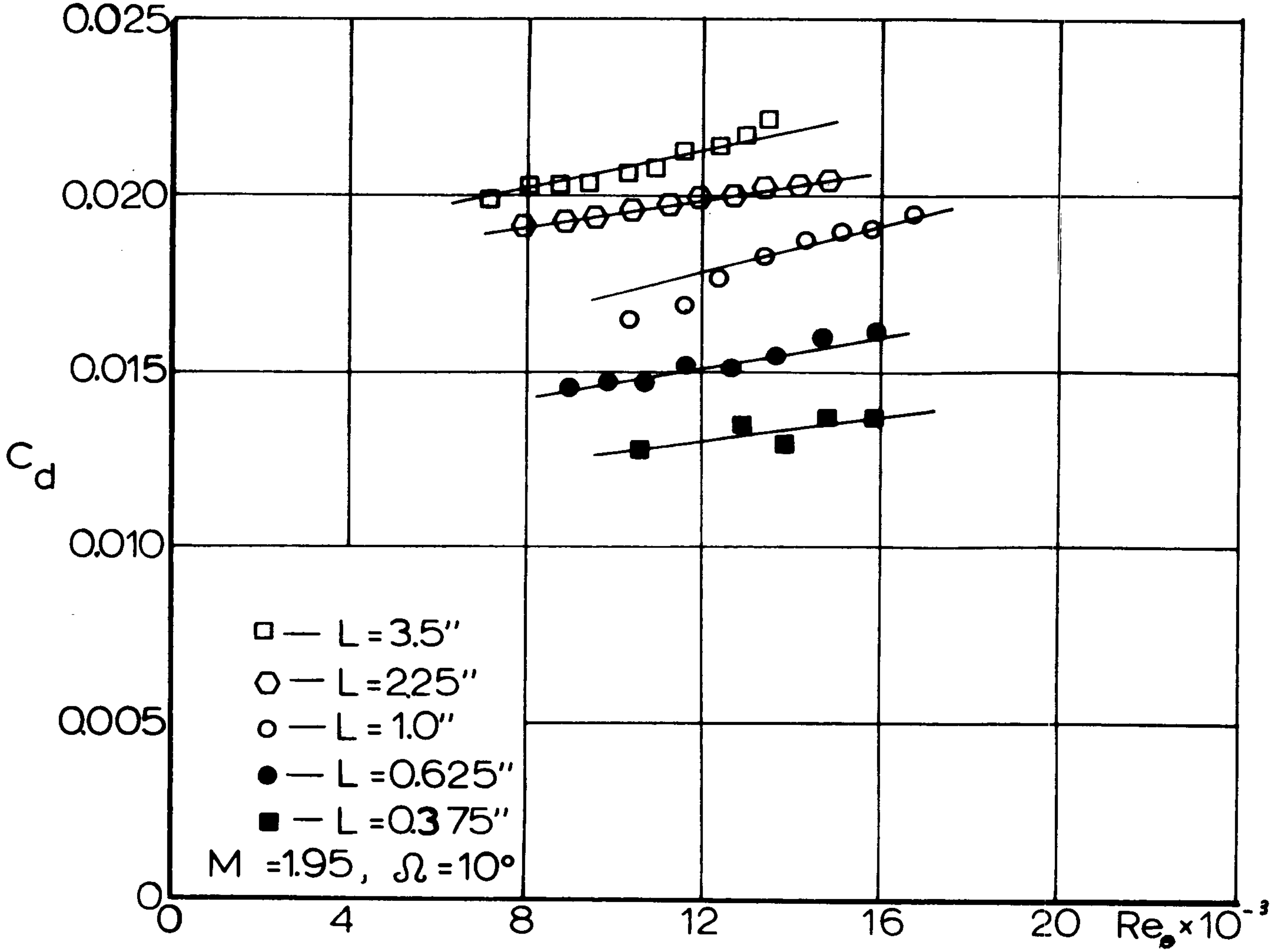

Figure 26. Supersonic Notch Drag Coefficients

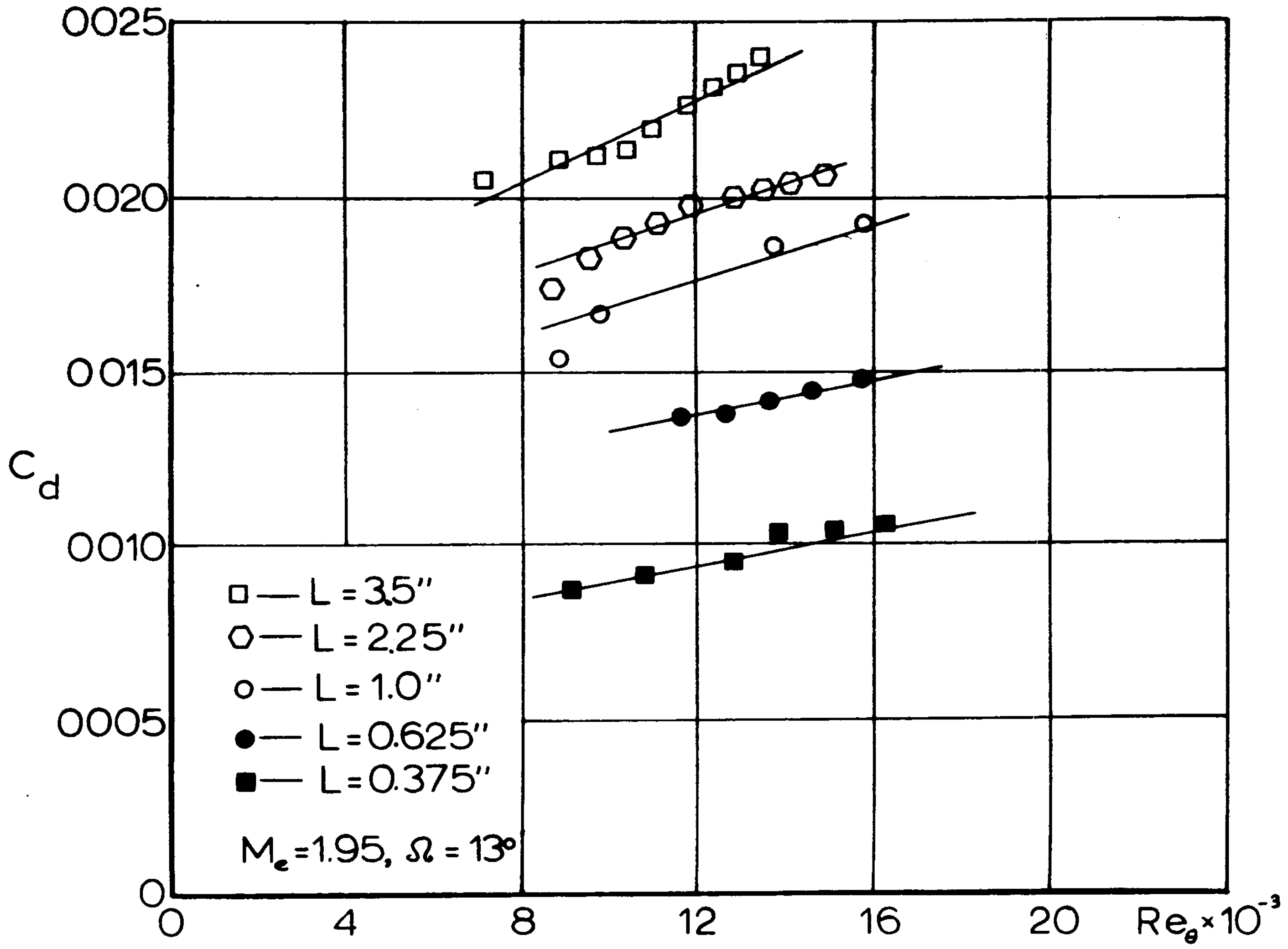

Figure 27. Supersonic Notch Drag Coefficients

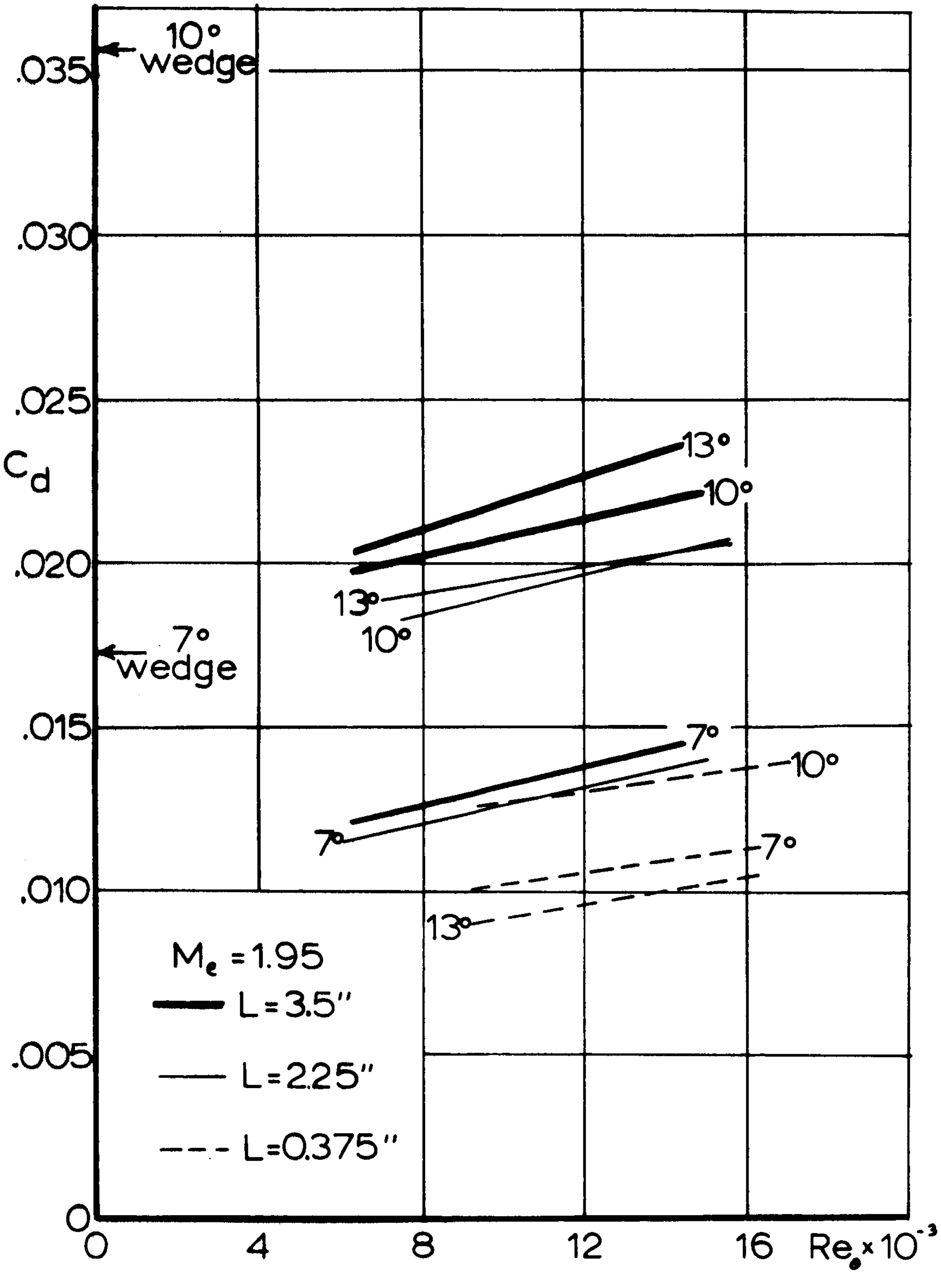

Figure 28. Summary of Supersonic C_d

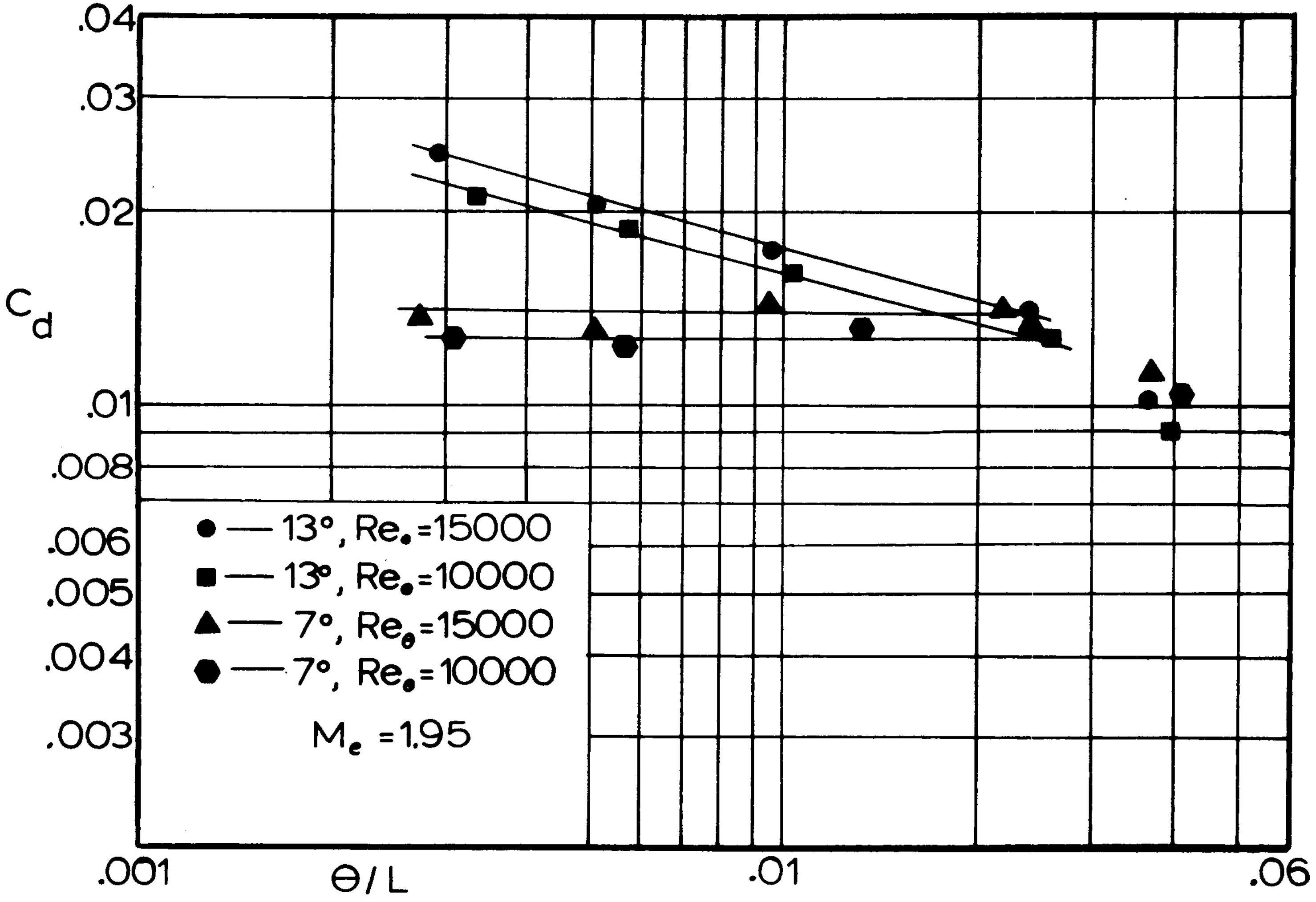

Figure 29. Shear Layer and Re_θ Effect on C_d

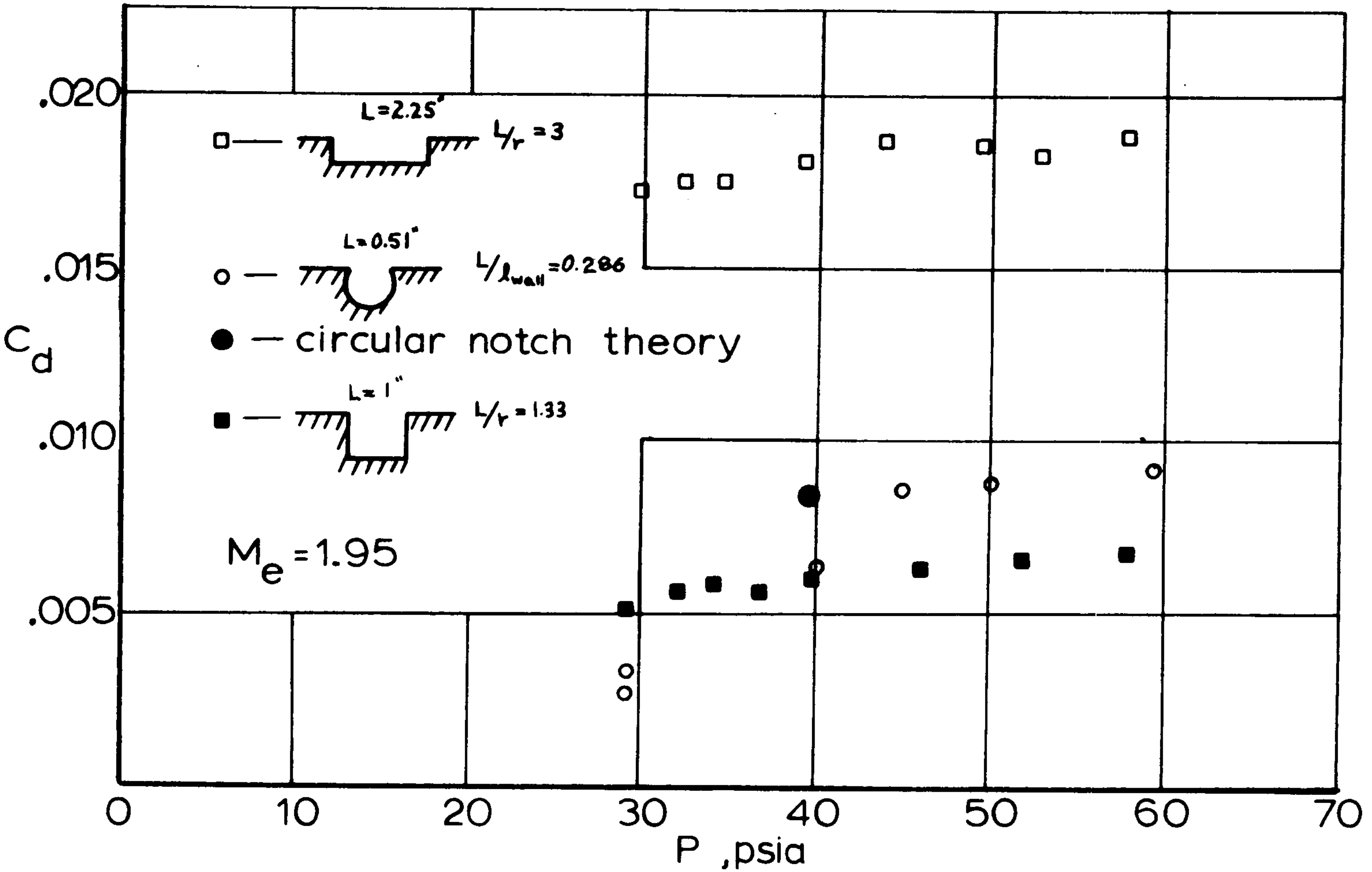

Figure 30. C_d for Rectangular and Circular Notches

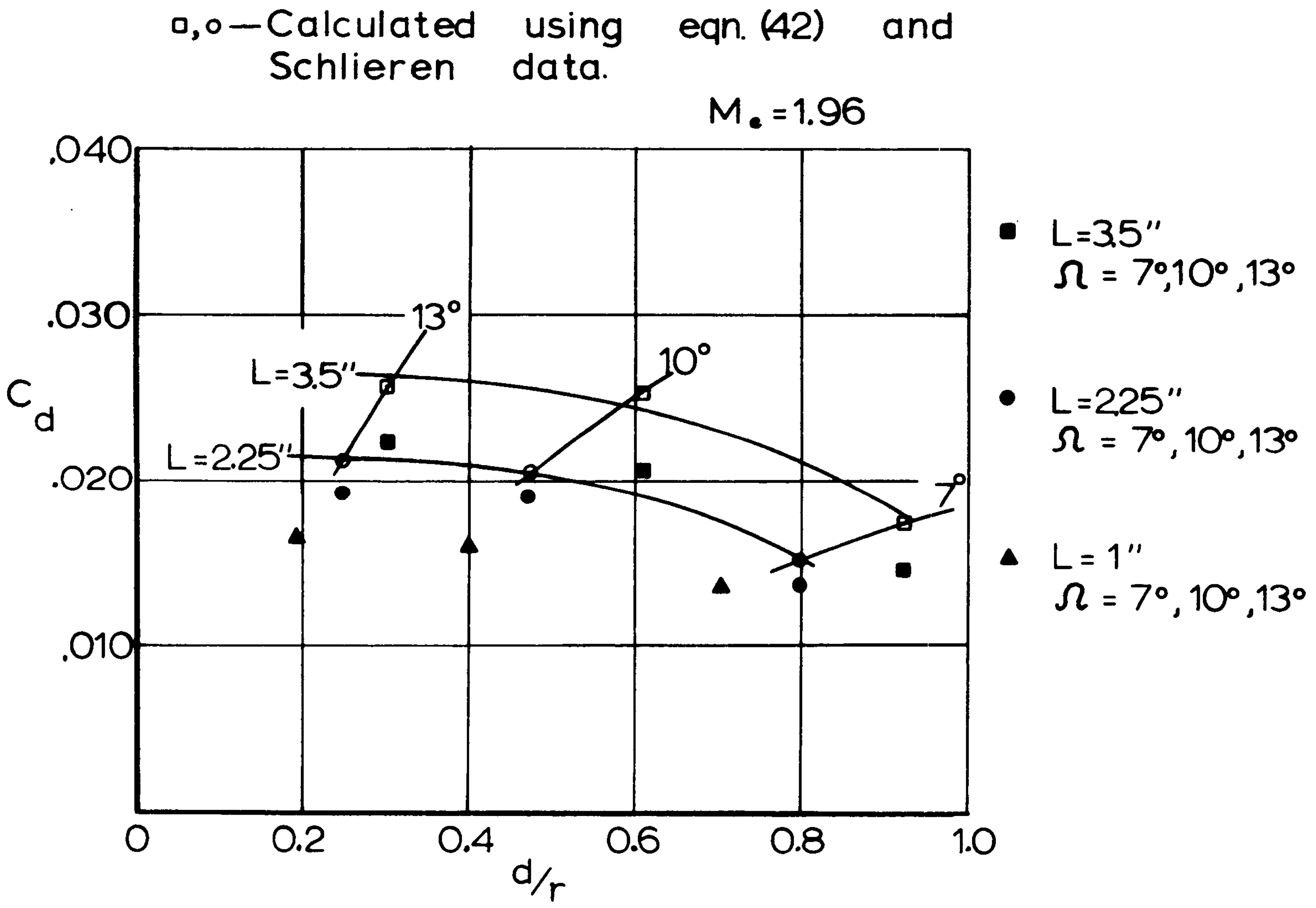

Figure 31. Theoretical and Experimental C_d

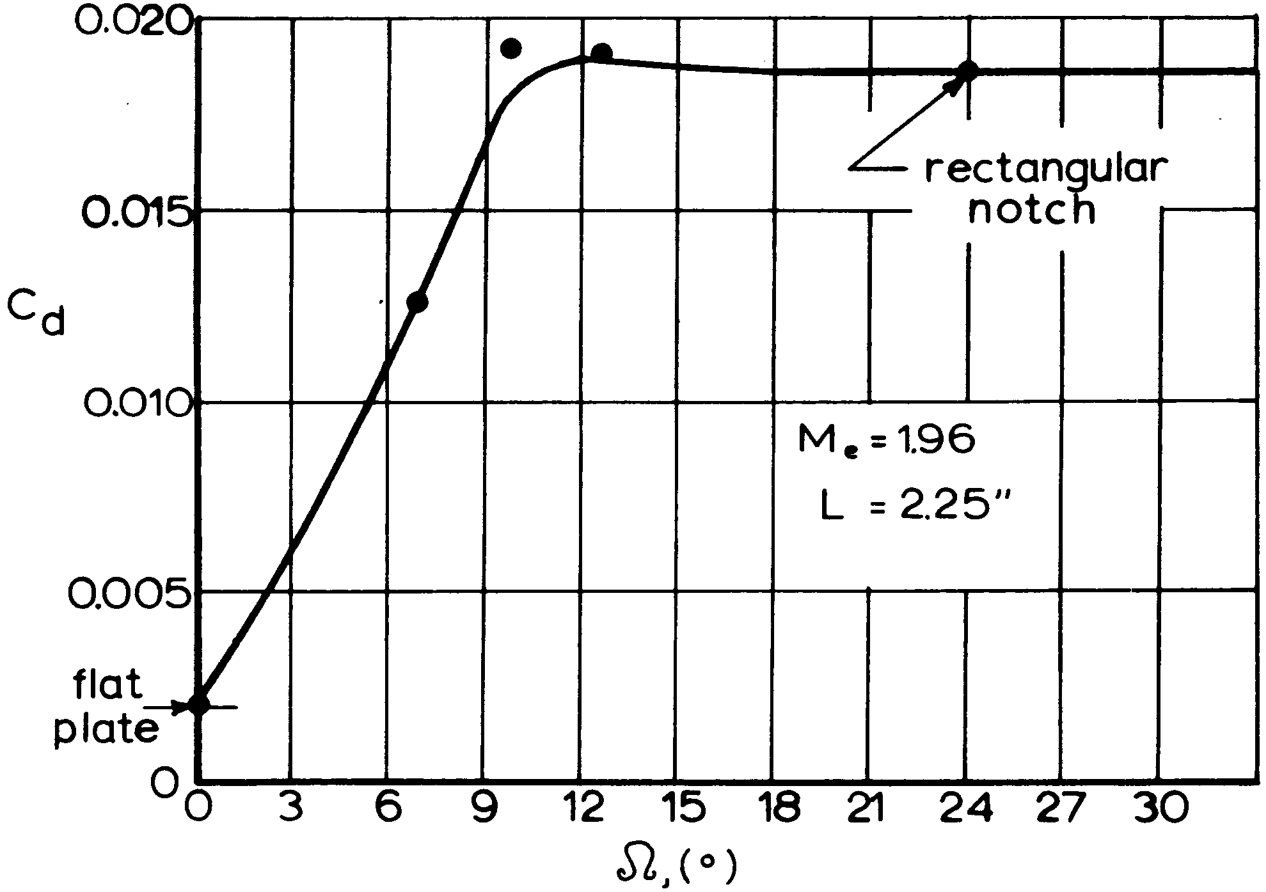

Figure 31a. C_d Variation with Notch Angle

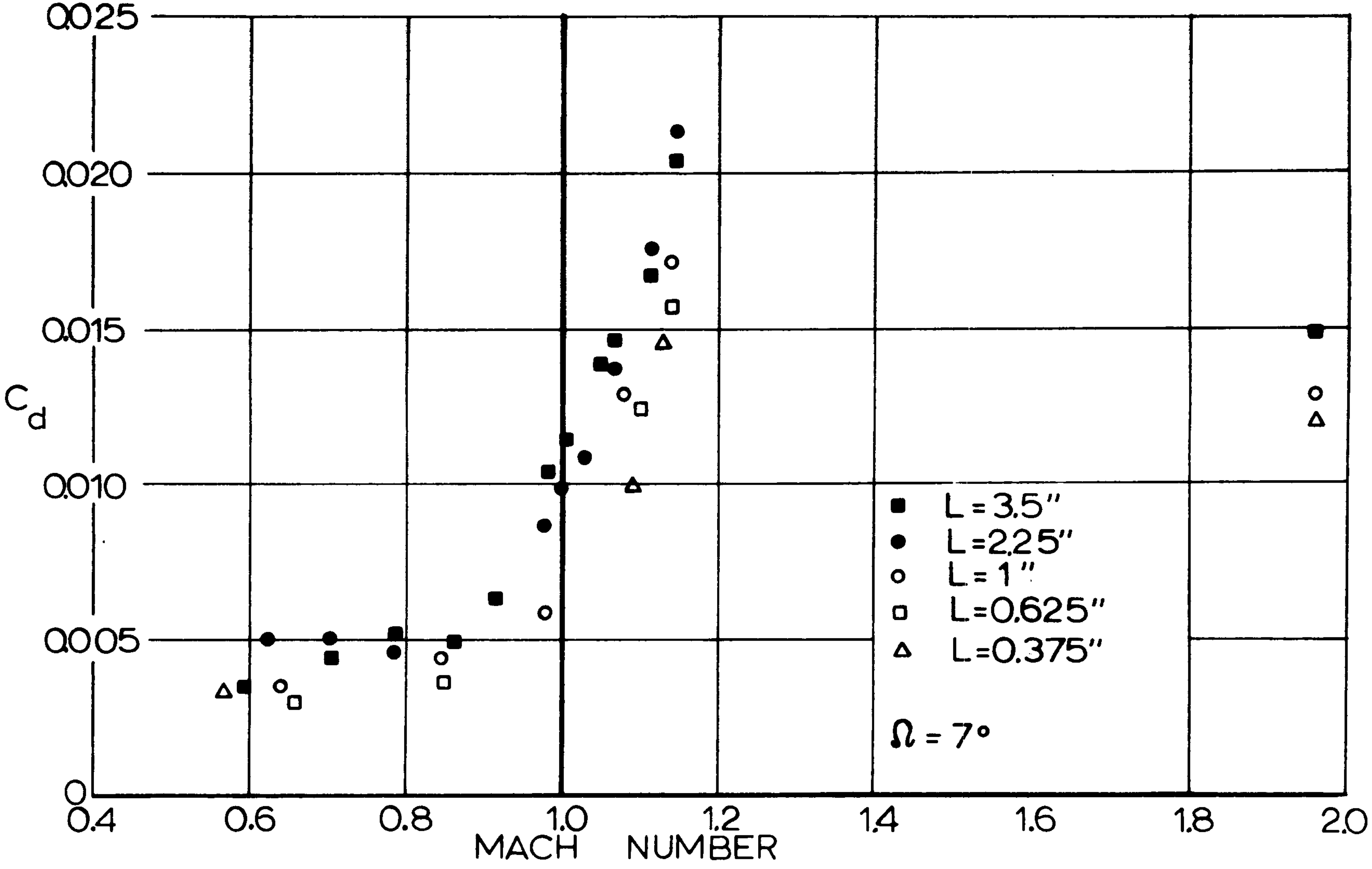

Figure 32. Transonic Notch Drag Coefficients

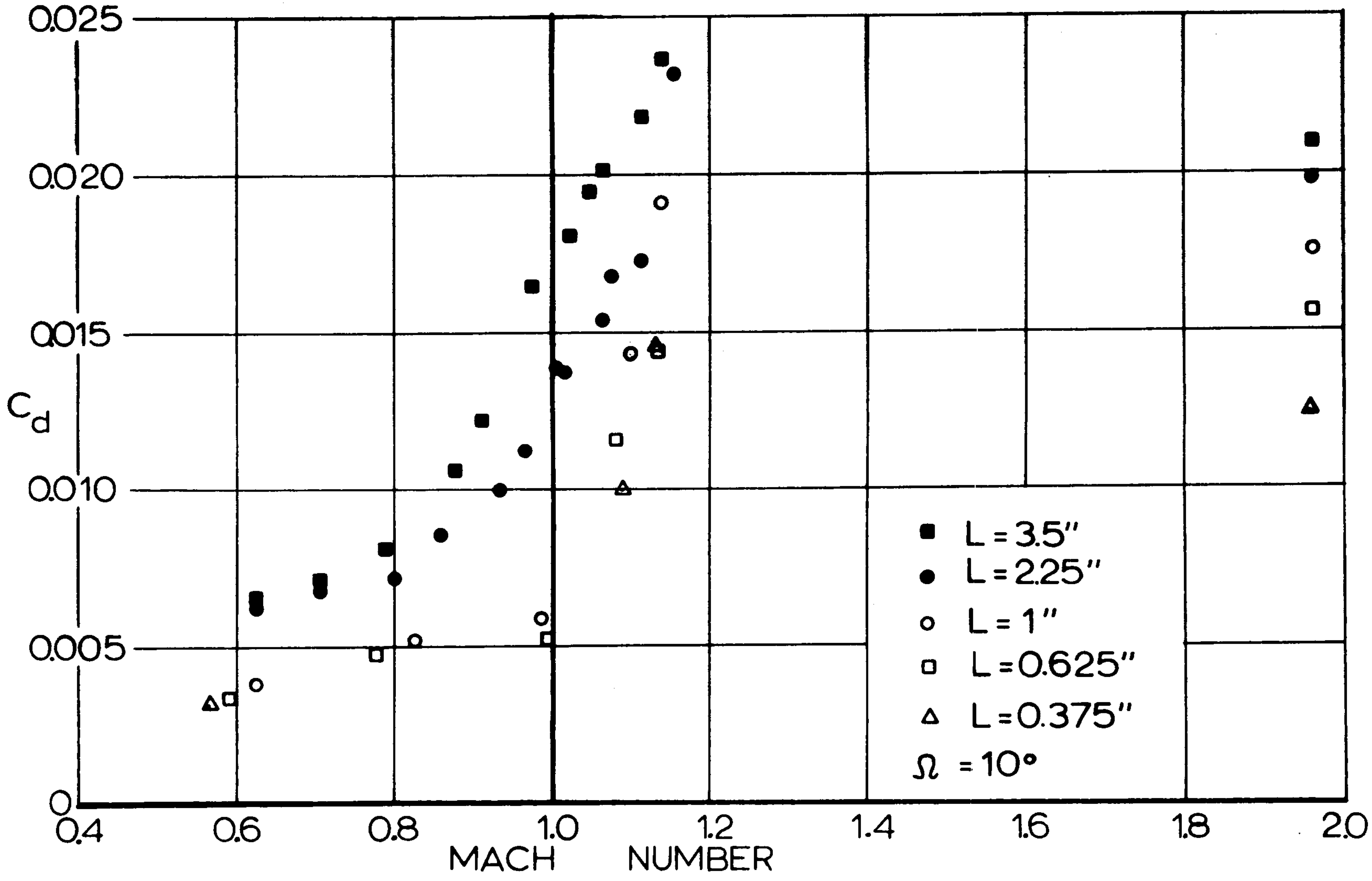

Figure 33. Transonic Notch Drag Coefficients

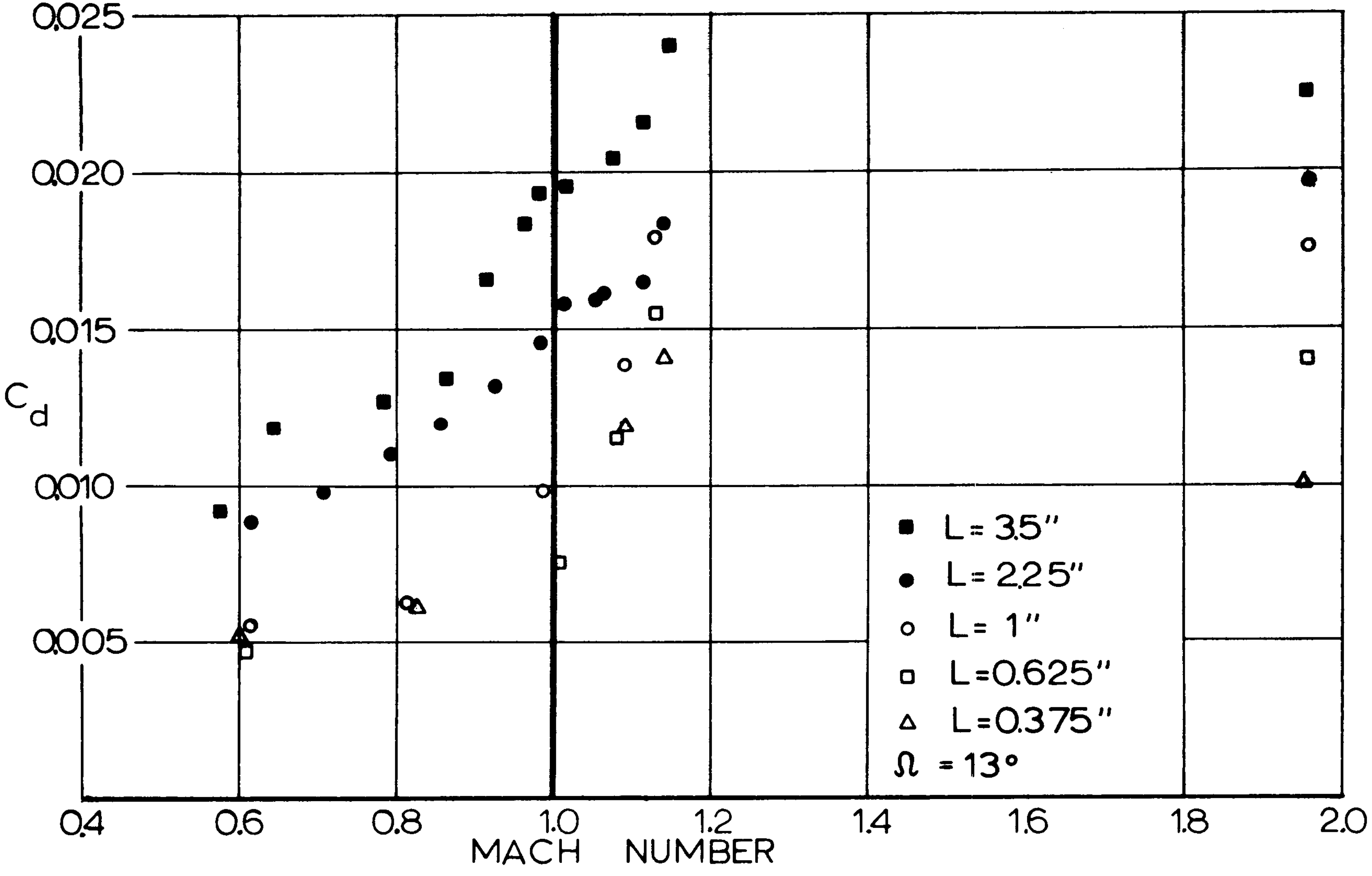

Figure 34. Transonic Notch Drag Coefficients

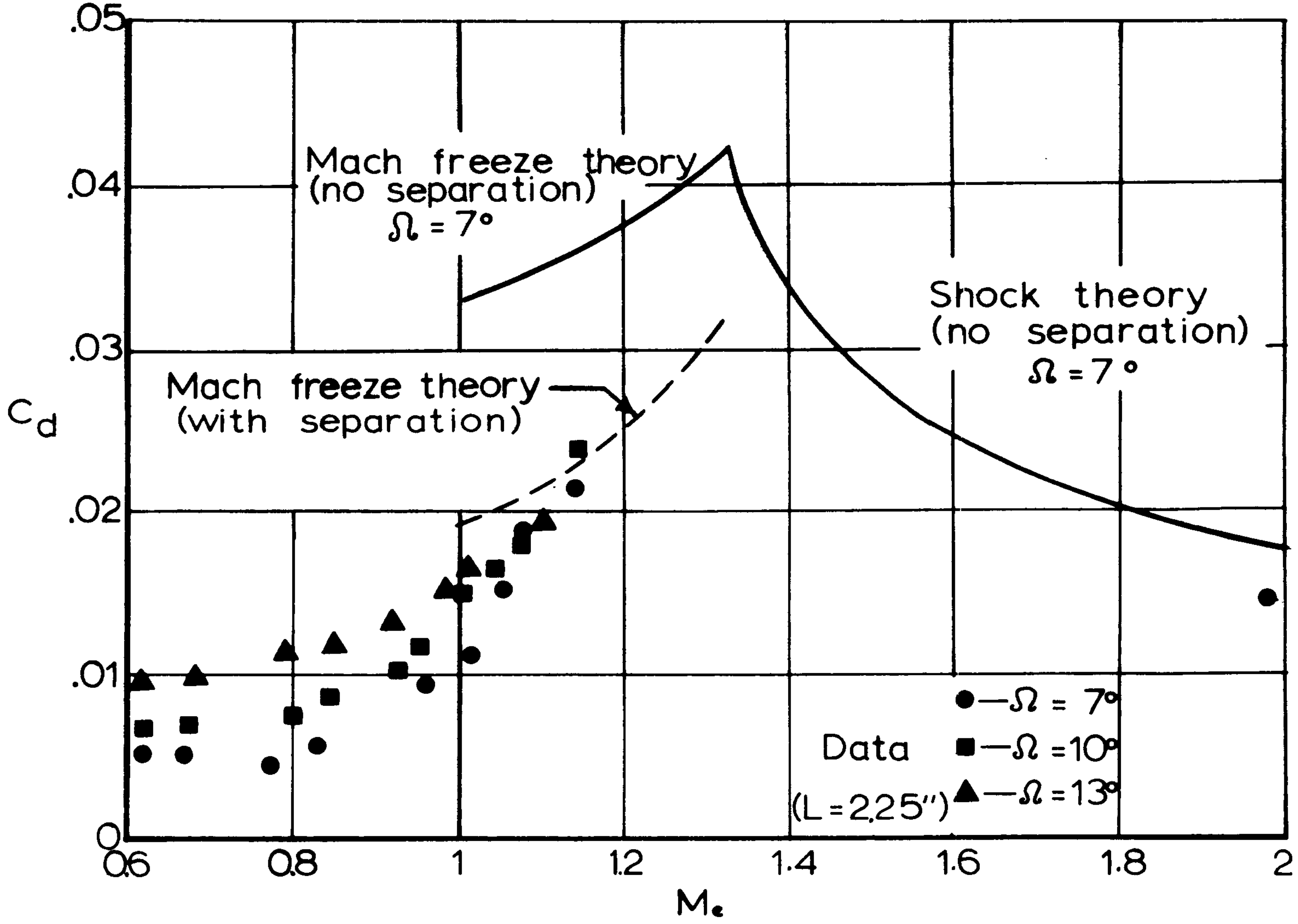

Figure 35. Comparison of C_d with Flow Model

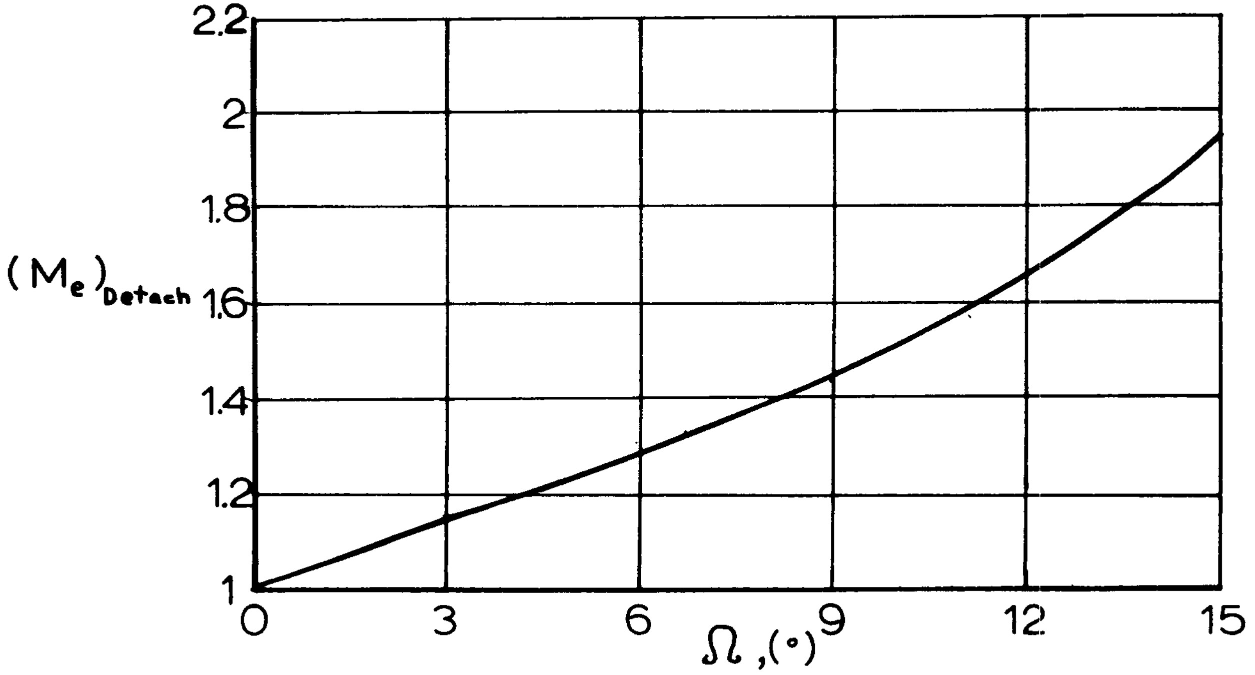

Figure 36. Detaching Mach Number

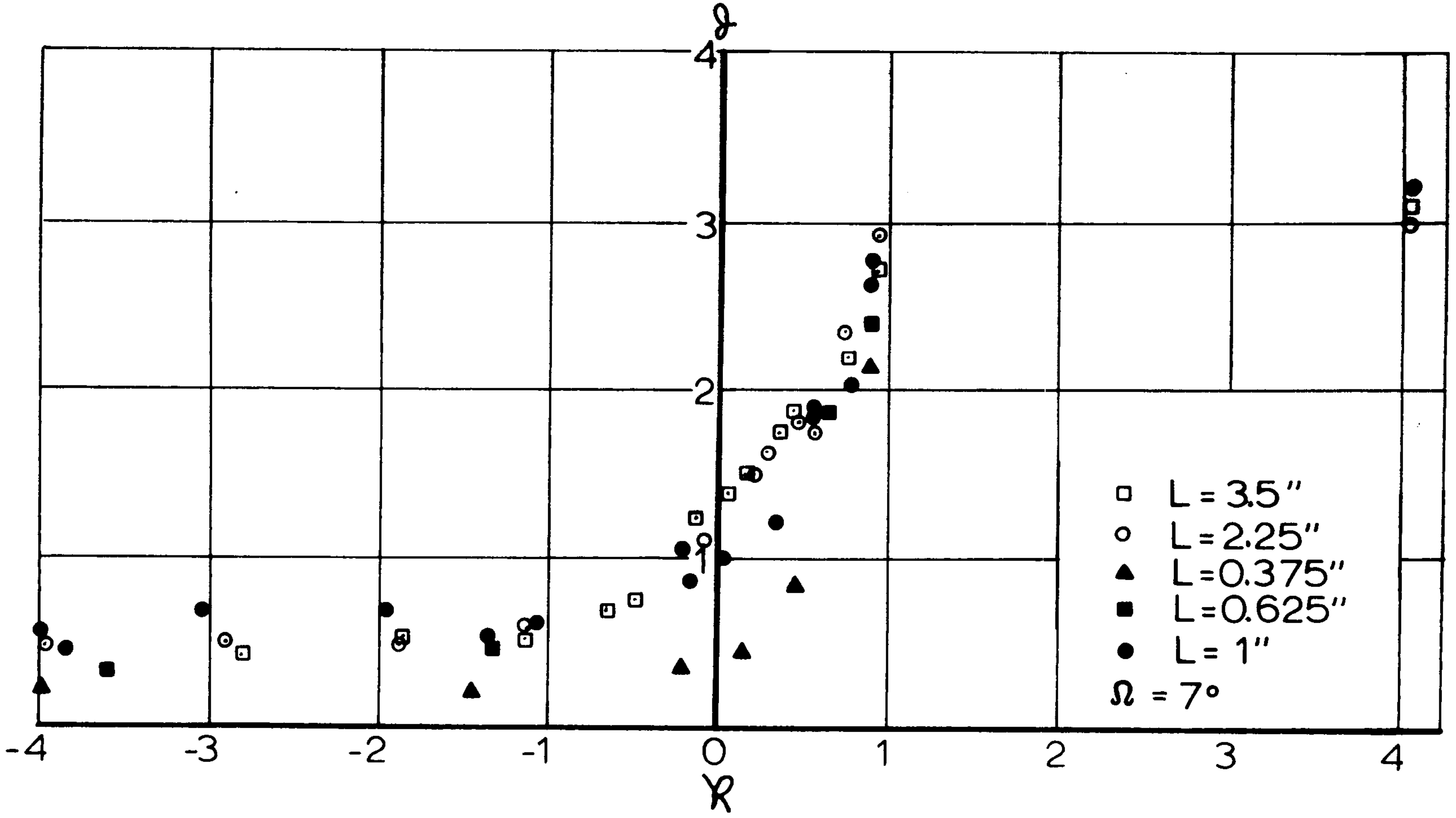

Figure 37. Transonic Similarity Parameters

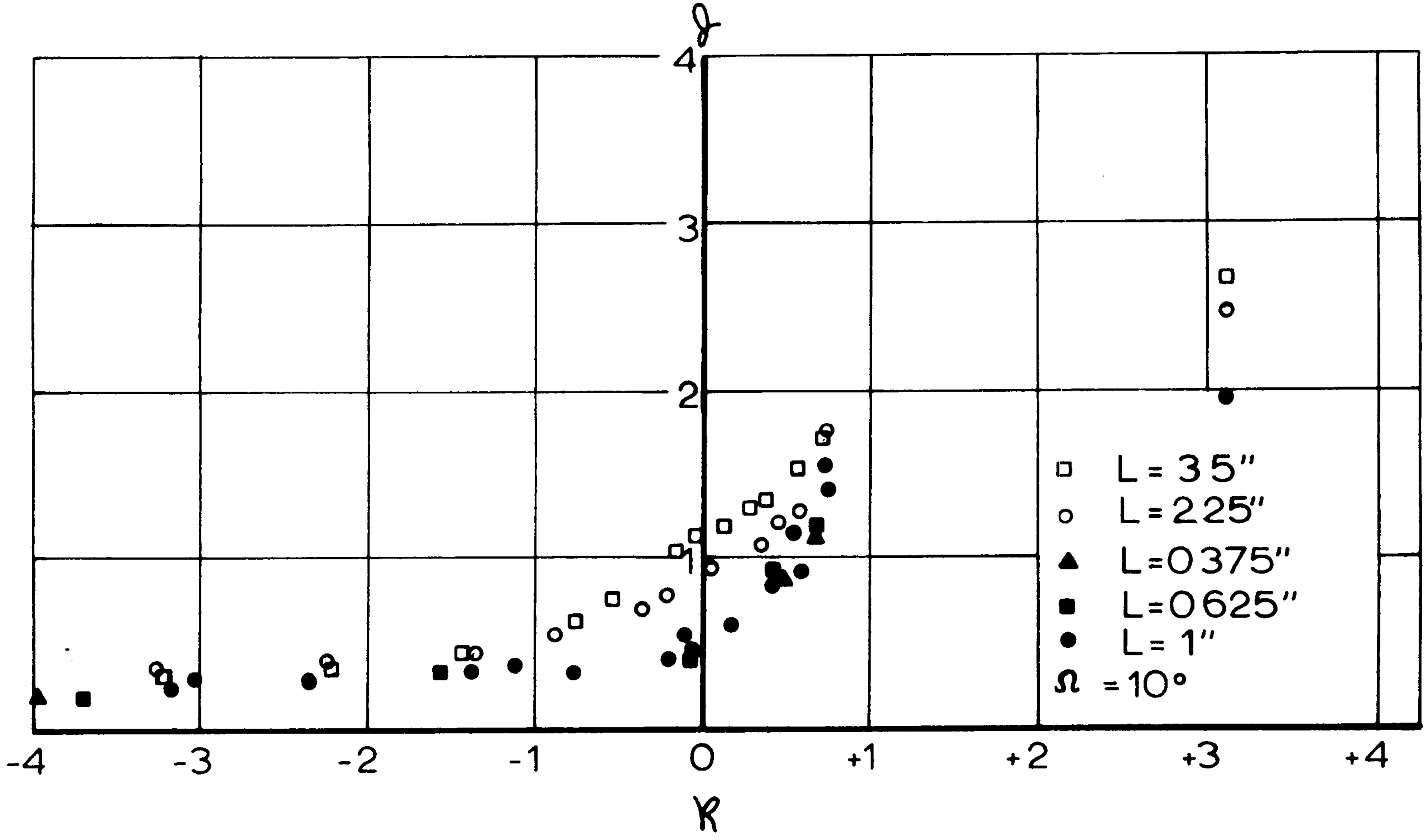

Figure 38. Transonic Similarity Parameters

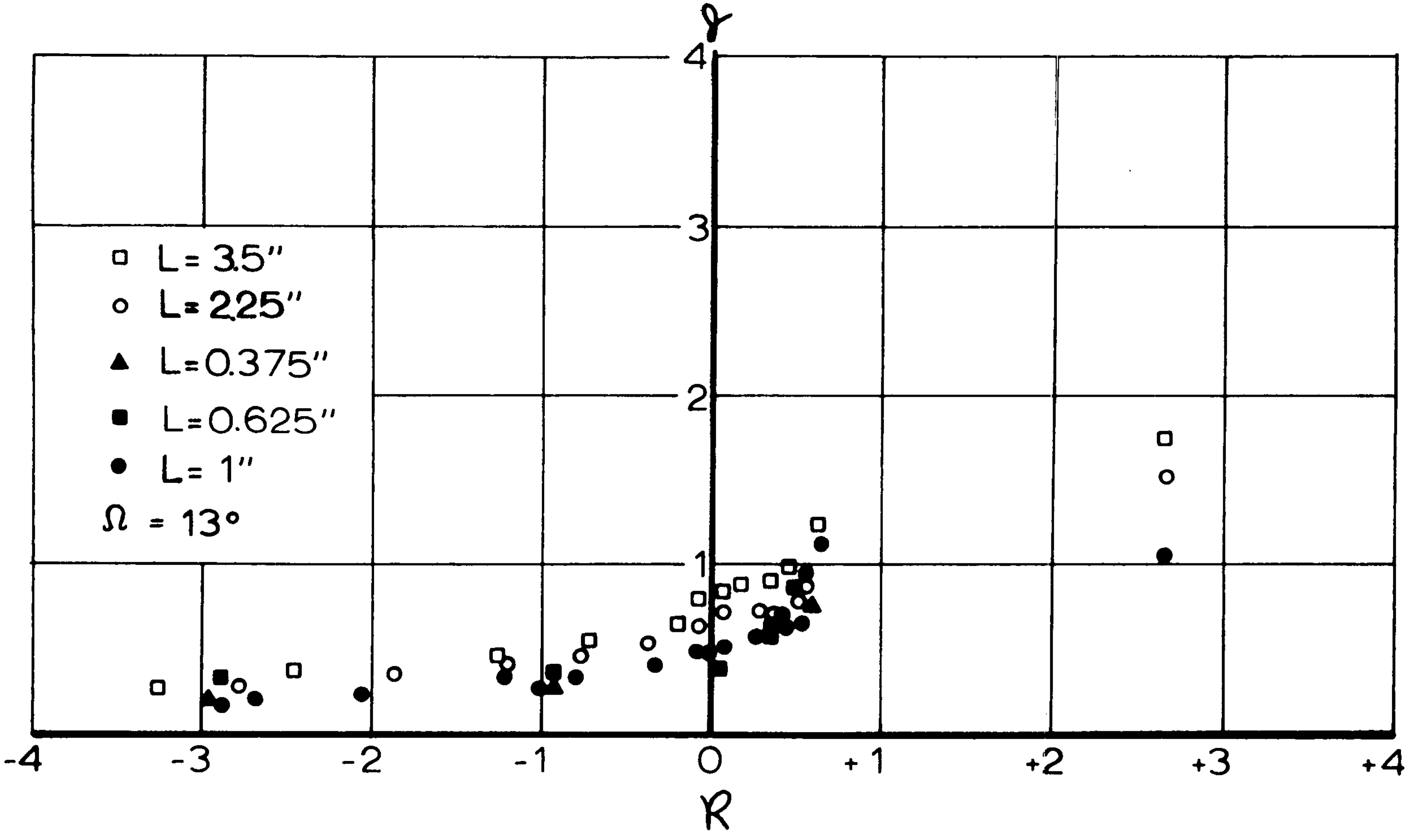

Figure 39. Transonic Similarity Parameters

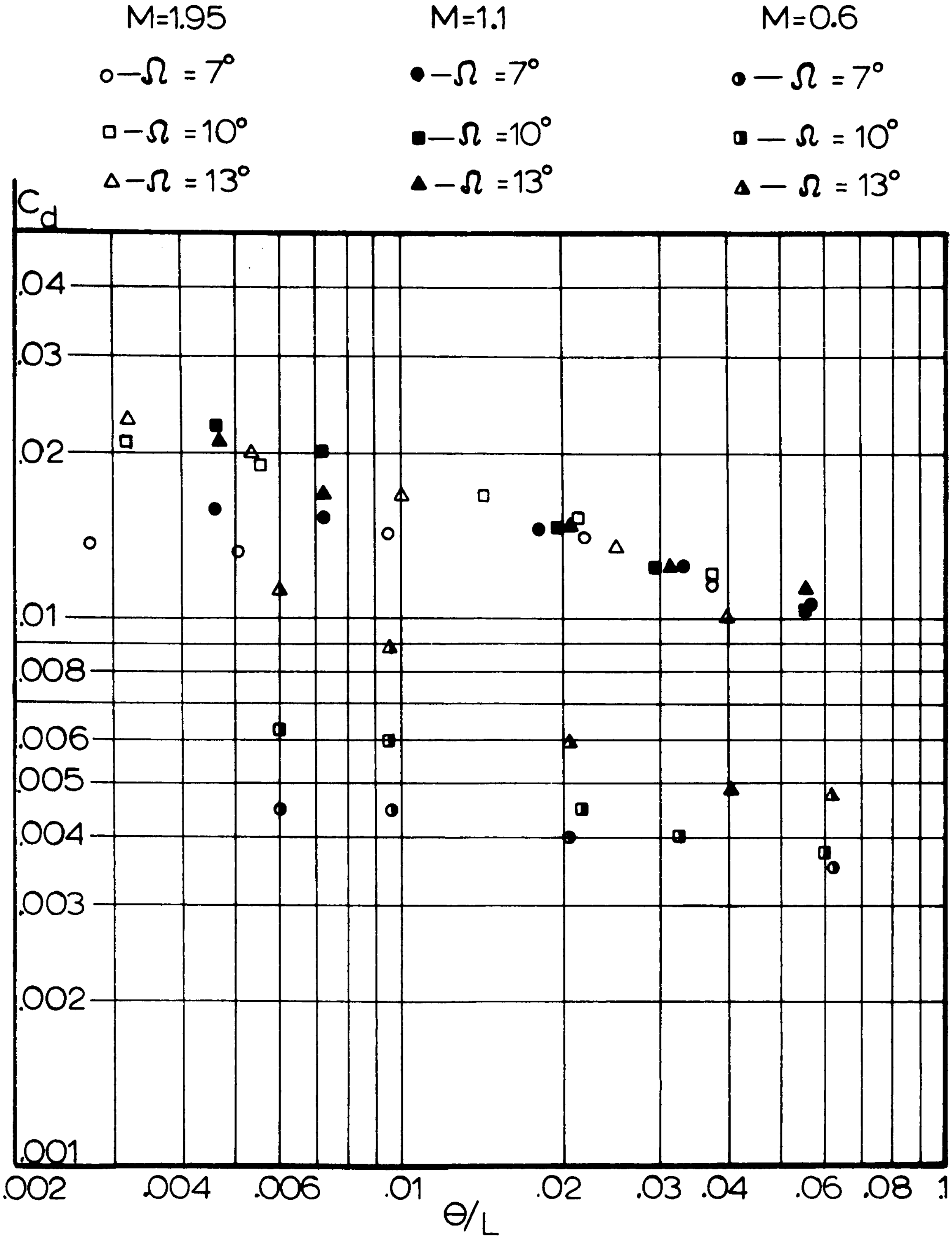

Figure 40. M_e and θ/L Effect on C_d

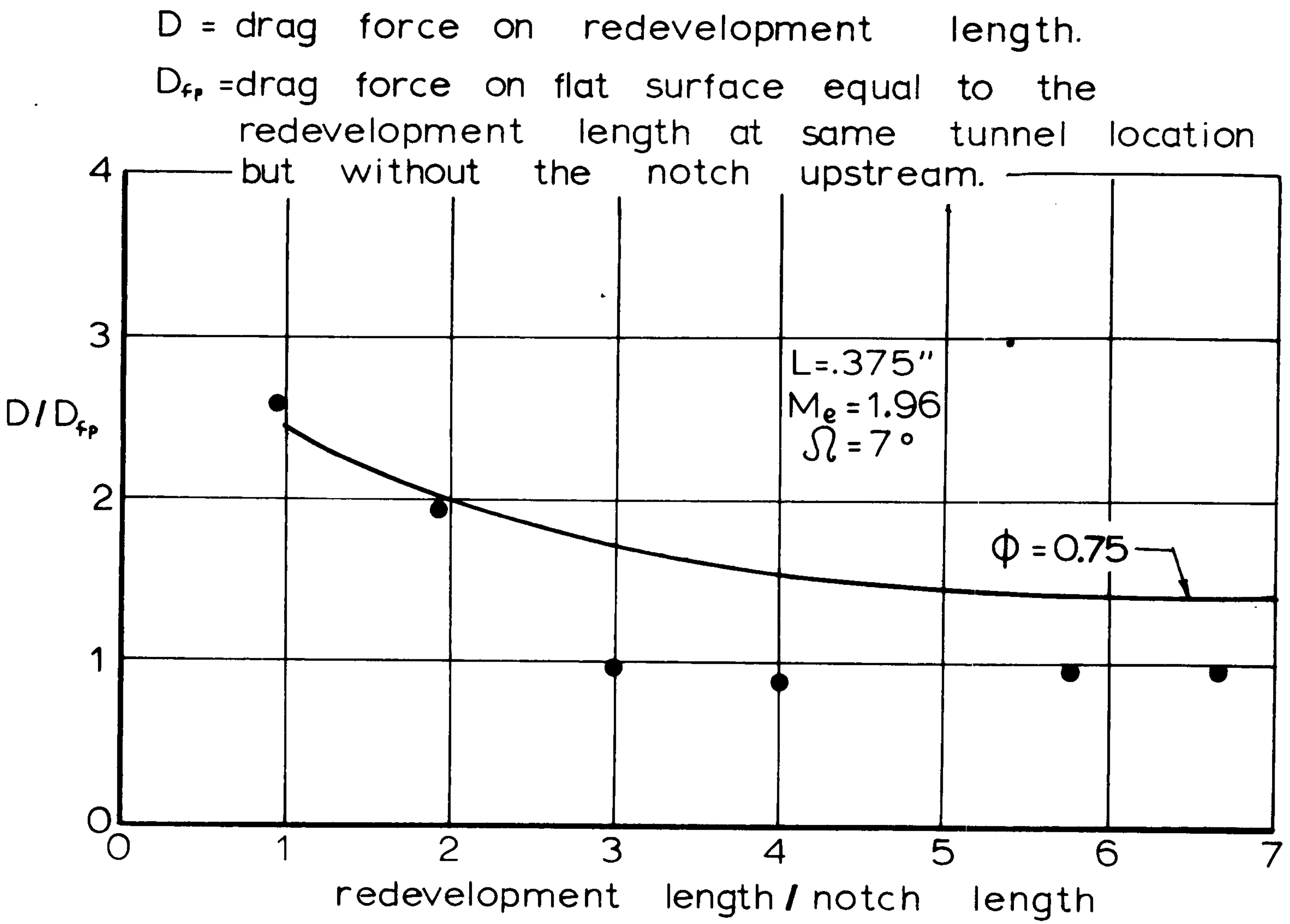

Figure 41. Redevelopment Drag Force

BIBLIOGRAPHY

1. Anandamurthy, K. R., and Hammit, A. G., "Investigation of the Interaction of a Turbulent Boundary Layer with Prandtl-Meyer Expansion Fans at M = 1.88," Princeton University, AFOSR TN-58-839, Report No. 434, 1958.

2. Baronti, P. O., and Libby, P. A., "Velocity Profiles in Turbulent Compressible Boundary Layers," AIAA Journal, February, 1966, p. 193.

3. Bloom, M. H., and Rubin, S., "High Speed Viscous Corner Flow," JAS, Vol. No. 28, February 1961, p. 145.

4. Brinich, P. F., and Diaconis, N. S., "Boundary Layer Development and Skin Friction at Mach Number 3.05," NACA TN-2742, 1952.

5. Bryson, A. E., "An Experimental Investigation of Transonic Flow Past Two-Dimensional Wedge and Circular Arc Sections Using a Mach Zehnder Interferometer," NACA TN-2560, November, 1951.

6. Carrière, P., and Sirieix, M., "Facteurs D'influence du Recollement d'un Ecoulement Supersonique," ONERA Memo Technique No. 20, 1961.

7. Chapman, A. J., "Mixing Characteristics of a Free Jet Boundary with Consideration of Initial Boundary Layer Configuration," Ph.D. Thesis, Department of Mechanical Engineering, University of Illinois, 1953.

8. Chapman, D. R., Kuehn, D. M., and Larson, H. K., "Investigation of Separated Flows in Supersonic and Subsonic Streams with Emphasis on the Effect of Transition," NACA TN-3869, 1957.

9. Charwat, A. F., Roos, J. M., Dewey, F. C., and Hitz, J. A., "An Investigation of Separated Flows--Part I: The Pressure Field, and Part II: Flow in the Cavity and Heat Transfer," JAS, June 1961, July 1961, pp. 457, 513.

10. Chuan, R. L., "On the Supersonic Flow of a Viscous Fluid Over a Compression Corner," 1956 Heat Transfer and Fluid Mechanics Institute (pre-print), 1956, p. 185.

11. Coles, D., "Direct Measurement of Supersonic Skin Friction," JAS, Vol. 19, 1952, p. 717.

12. Coles, D., "Measurements of Turbulent Friction on a Smooth Flat Plate in Supersonic Flow," JAS, Vol. 21, 1954, p. 433.

13. Crocco, L., and Lees, L., "A Mixing Theory for the Interaction Between Dissipative Flows and Isentropic Streams," JAS, Vol. 19, 1952, p. 649.

14. Culick, F. E. C., and Hill, J. A. F., "A Turbulent Analog of the Stewartson-Illingworth Transformation," JAS, April 1958, p. 259.

15. Dailey, C. L., and Wood, F. C., Computation Curves for Compressible Fluid Problems, John Wiley & Sons, Inc., 1949.

16. Davies, P., Dyke, R. W., and Marchaj, C. A., "The Wind Tunnel Balances in the Large Low Speed Tunnel at Southampton University," University of Southampton Department of Aeronautics and Astronautics, Report No. 208, 1960.

17. Dhawan, Satish, "Direct Measurement of Skin Friction," NACA TN-2567, 1952.

18. Drougge, G., "An Experimental Investigation of the Influence of Strong Adverse Pressure Gradients on Turbulent Boundary Layers at Supersonic Speed," The Aeronautical Research Institute of Sweden, Report No. 46, 1953.

19. Erdos, J., and Pallone, A., "Shock-Boundary Layer Interactions and Flow Separation," Proceedings of the 1962 Heat Transfer and Fluid Mechanics Institute, pp. 239-255, 1962.

20. Golik, R. J., "On the Dissipative Mechanisms Within Separated Flow Regions," Ph.D. Thesis, Department of Mechanical Engineering, University of Illinois, 1962.

21. Hakkinen, R. J., "Measurements of Turbulent Skin Friction on a Flat Plate at Transonic Speeds," NACA TN-3486, 1955.

22. Hoerner, S. F., Fluid Dynamic Drag, Published by the author, 1958.

23. Jackson, M. W., Czarnecki, K. R., and Monta, W. J., "Turbulent Skin Friction at High Reynolds Numbers and Low Supersonic Velocities," NASA TN-2687, 1965.

24. Kaye, J., "Survey of Friction Coefficients, Recovery Factors, and Heat Transfer Coefficients for Supersonic Flow," JAS, Vol. 21, 1954, p. 117.

25. Korst, H. H., "Approximate Calculations of Two-Dimensional Compressible Turbulent Boundary Layers with Pressure Gradient in the Free Stream," unpublished, 1958.

26. Korst, H. H., Page, R. H., and Childs, M. E., "Compressible Two-Dimensional Jet Mixing at Constant Pressure," University of Illinois, Engineering Experimental Station, M. E. Technical Note 392-1, 1954.

27. Korst, H. H., Chow, W. L., and Zumwalt, G. W., "Research on Transonic and Supersonic Flow of Real Fluids at Abrupt Increases in Cross Section," University of Illinois, ME Technical Report 392-5, Second Edition, October 1964.

28. Korst, H. H., and Chow, W. L., "Non-Isoenergetic Turbulent ($Pr_t = 1$) Jet Mixing Between Two Compressible Streams at Constant Pressure," University of Illinois, ME TN-393-2, April 1965.

29. Korst, H. H., "Dynamics and Thermodynamics of Separated Flows," Reprint from Single and Multi-Flow Processes (Symposium of Rutgers Engineering Centennial), Rutgers University Press, 1965.

30. Krishnamurty, K., "Acoustic Radiation from Two-Dimensional Rectangular Cutouts in Aerodynamic Surfaces," NACA-TN-3487, 1955.

31. Lamb. J. P., "The Development of Free Turbulent Shear Layers," Rocket Test Facility, Arnold Engineering Development Center, AEDC-TR-65-184, 1965.

32. Lees, L., and Reeves, B. L., "Supersonic Separated and Reattaching Laminar Flows: I. General Theory and Application to Adiabatic Boundary-Layer/ Shock-Wave Interactions," AIAA Journal, Vol. 2, 1964, p. 1907.

33. Liepmann, H. W., and Bryson, A. E., "Transonic Flow Past Wedge Sections," JAS, December 1950, p. 745.

34. Mager, A., "On the Model of the Free, Shock-Separated, Turbulent Boundary Layer," Journal of the Aeronautical Sciences, Vol. 23, 1956, pp. 181-184.

35. Murray, W. M., and Stein, P. K., Strain Gage Techniques, Massachusetts Institute of Technology Press, 1958.

36. O'Donnel, R. M., "Experimental Investigation at a Mach Number of 2.41 of Average Skin Friction Coefficients and Velocity Profiles for Laminar and Turbulent Boundary Layers and an Assessment of Probe Effects," NACA TN-3122, 1954.

37. O'Donnel, F. B., and Westkaemper, J. C., "Measurement of Errors Caused by Misalignment of Floating Element Skin Friction Balances," AIAA Journal, Vol. 3, 1963.

38. Perry, C. C., and Lissner, H. R., The Strain Gage Primer, McGraw-Hill Book Co., Inc., 1955.

39. Peterson, J. B., "A Comparison of Experimental and Theoretical Results for the Compressible Turbulent Boundary Layer Friction with Zero Pressure Gradient," NASA TN-D-1795, 1963.

40. Roshko, A., "Some Measurements of Flow in a Rectangular Cutout," NACA TN-3488, 1955.

41. Schick, W. F., "A Floating Element Wind Tunnel Balance," University of California Institute of Engineering Research Series No. 20, Technical Report H. E.-150-159, 1958.

42. Schlichting, H., Boundary Layer Theory, McGraw-Hill Book Company, Inc., Fourth Edition, 1960.

43. Shapiro, A. H., The Dynamics and Thermodynamics of Compressible Fluid Flow, Volumes I and II, The Ronald Press Company, 1954.

44. Sommer, S. C., and Short, B. J., "Free Flight Measurements of Turbulent Boundary Layer Skin Friction in the Presence of Severe Aerodynamic Heating at Mach Numbers from 2.8 to 7.0," NACA TN-3391, 1955.

45. Spreiter, J. R., "On the Application of Transonic Similarity Rules," NACA TN-2726, 1952.

46. Steiger, M. H., and Bloom, M. H., "Linearized Viscous Free Mixing with Streamwise Pressure Gradients," AIAA Journal, Vol. 2, February 1964, p. 263.

47. Thomke, G. J., "Separation and Reattachment of Supersonic Turbulent Boundary Layers Behind Downstream Facing Steps and Over Cavities," Douglas Report SM-43062, Douglas Aircraft Co., 1964.

48. Truckenbrodt, E., "A Method of Quadrature for Calculation of the Laminar and Turbulent Boundary Layer in the Case of Plane and Rotationally Symmetrical Flow," NACA TN-1379, 1955.

49. Vollus, R. J., Handbook of Supersonic Aerodynamics--Section 20--Wind Tunnel Instrumentation and Operation, NAVORD Report 1488, Volume 6, 1961.

50. White, R. A., "Turbulent Boundary Layer Separation from Smooth-Convex Surfaces in Supersonic Two-Dimensional Flow." Ph.D. Thesis, University of Illinois, Department of Mechanical Engineering, 1963.

51. Wilson, R. E., "Turbulent Boundary Layer Characteristics at Supersonic Speeds--Theory and Experiment," JAS, Vol. 17, 1960, p. 585.

52. Wuerer, J. E., and Clayton, F. I., "Flow Separation in High Speed Flight A Review of the State of the Art," Douglas Aircraft Company, Inc., Douglas Report SM-46429, 1965.

53. Holden, M. S., "An Analytical Study of Separated Flows Induced by Shock-Wave Boundary Layer Interaction," Cornell Aeronautical Report AI-1972-A-2, November 1965.

APPENDIX

Table 7

Supersonic Notch Drag Results ($M_e = 1.96$)

Notch length (ins.)	Notch angle (°)	Notch Shape	C_d	Re_θ	θ/L
3.5	7	V	0.01225	7270	0.00358
			0.01268	7960	0.00352
			0.01285	8830	0.00343
			0.01298	9510	0.00337
			0.01325	10150	0.00332
			0.01338	10880	0.00326
			0.01348	11530	0.00318
			0.01352	12200	0.00312
			0.01350	12830	0.00313
			0.01367	13350	0.00298
3.5	10	V	0.0197	7100	0.00358
			0.0201	8020	0.00352
			0.0204	8750	0.00343
			0.0206	9430	0.00337
			0.0209	10280	0.00329
			0.0213	10920	0.00326
			0.0217	11530	0.00318
			0.0219	12300	0.00312
			0.0221	12800	0.00303
			0.0223	13400	0.00298
3.5	13	V	0.0206	7170	0.00358
			0.0212	8750	0.00343
			0.0212	9660	0.00337
			0.0217	10220	0.00329
			0.0221	10930	0.00326
			0.0227	11650	0.00318
			0.0231	12180	0.00312
			0.0234	12800	0.00303
			0.0239	13400	0.00298
2.25	7	V	0.0127	8070	0.0061
			0.0128	8740	0.0060
			0.0128	9540	0.00588
			0.0127	10480	0.00574
			0.0127	11160	0.00565
			0.0128	11780	0.00556
			0.0129	12700	0.00543
			0.0129	13420	0.00534
			0.0132	14100	0.0052
			0.0134	14880	0.00516

Table 7 (continued)

Notch length (ins.)	Notch angle (°)	Notch Shape	C_d	Re_θ	θ/L
2.25	10	V	0.0189	7930	0.0061
			0.0193	8740	0.0060
			0.0193	9620	0.0058
			0.0195	10400	0.0057
			0.0197	11280	0.0056
			0.0199	11970	0.0055
			0.0201	12620	0.0054
			0.0202	13370	0.0054
			0.0203	14100	0.0052
			0.0205	14830	0.0051
2.25	13	V	0.0165	7980	0.0061
			0.0174	8830	0.0060
			0.0183	9570	0.0058
			0.0190	10320	0.0057
			0.0194	11180	0.0056
			0.0198	11900	0.0055
			0.0199	12820	0.0054
			0.0201	13500	0.0053
			0.0203	14100	0.0052
			0.0205	14900	0.0051
1.0	7	V	0.0138	8600	0.0136
			0.0141	9630	0.0135
			0.0142	10570	0.0132
			0.0143	11500	0.0130
			0.0147	12600	0.0128
			0.0149	13250	0.0126
			0.015	14170	0.0124
			0.0158	14980	0.0122
			0.0156	15800	0.0119
			0.0158	16650	0.0117
1.0	10	V	0.0156	9600	0.0148
			0.0165	10480	0.0145
			0.0168	11600	0.0143
			0.0176	12300	0.0141
			0.0181	13400	0.0138
			0.0188	14300	0.0136
			0.0191	15100	0.0133
			0.0190	15720	0.0131
			0.0194	16700	0.0129
1.0	13	V	0.0152	8770	0.0150
			0.0169	10800	0.0144
			0.0181	13900	0.0137
			0.0186	15800	0.0131

Table 7 (continued)

Notch length (ins.)	Notch angle (°)	Notch Shape	C_d	Re_θ	θ/L
0.625	7	V	0.0128	9150	0.0240
			0.0134	9730	0.0238
			0.0140	10600	0.0235
			0.0136	11420	0.0231
			0.0146	12600	0.0227
			0.0141	13780	0.0223
			0.0138	14830	0.0218
			0.0143	15800	0.0213
0.625	10	V	0.0146	8900	0.0220
			0.0147	9770	0.0217
			0.0147	10680	0.0213
			0.0155	11580	0.0210
			0.0151	12580	0.0207
			0.0156	13700	0.0203
			0.0163	14750	0.0198
			0.0160	15900	0.0192
0.625	13	V	0.0141	10400	0.0260
			0.0134	11680	0.0256
			0.0134	12680	0.0252
			0.0136	13610	0.0248
			0.0139	14670	0.0242
			0.0146	15780	0.0237
0.375	7	V	0.0092	10900	0.0394
			0.0110	12050	0.0396
			0.0110	12820	0.0384
			0.0120	13700	0.0376
			0.0112	14730	0.0371
			0.0112	15120	0.0365
			0.0115	16300	0.0357
0.375	10	V	0.0132	15670	0.0362
			0.0133	14820	0.0368
			0.0123	13800	0.0376
			0.0131	12800	0.0381
			0.0126	10860	0.0394
0.375	13	V	0.0106	16050	0.0357
			0.0103	15100	0.0365
			0.0103	13800	0.0376
			0.0092	12960	0.0384
			0.0086	9880	0.0402
			0.0081	9150	0.0405

Table 7 (concluded)

Notch length (ins.)	Notch shape	C_d	Stagnation Pressure (psia)
2.25	rectangular	0.0172	29.98
		0.0174	34.59
		0.0181	39.29
		0.0188	43.89
		0.0185	49.49
		0.0183	52.49
		0.0185	57.99
		0.0175	32.29
1.0	rectangular	0.00511	29.11
		0.00578	34.21
		0.00594	39.91
		0.00625	45.91
		0.00651	51.91
		0.00656	57.81
		0.00556	36.81
		0.00558	32.11
0.512	circular	0.0031	29.0
		0.00598	39.6
		0.00828	44.9
		0.00881	50.0
		0.00928	59.0

Table 8

Transonic Notch Drag Results

Notch length (ins.)	Notch angle (°)	Notch shape	C_d	Mach number
3.5	7	V	0.0202	1.145
			0.0167	1.114
			0.0147	1.07
			0.0138	1.05
			0.0121	1.026
			0.0113	1.004
			0.0104	0.982
			0.0062	0.917
			0.0049	0.862
			0.0050	0.0079
			0.0044	0.712
			0.0035	0.006
3.5	10	V	0.0236	1.14
			0.0218	1.113
			0.0201	1.066
			0.0194	1.049
			0.0180	1.022
			0.0178	0.99
			0.0164	0.975
			0.122	0.911
			0.106	0.879
			0.0081	0.79
			0.0071	0.707
			0.0065	0.623
3.5	13	V	0.024	1.143
			0.0216	1.115
			0.0203	1.077
			0.0205	1.038
			0.0196	1.016
			0.0193	0.979
			0.0183	0.963
			0.0165	0.914
			0.0133	0.864
			0.0127	0.782
			0.0118	0.643
			0.00923	0.578
2.25	7	V	0.0213	1.146
			0.0141	1.082
			0.0087	0.981
			0.0053	0.863
			0.0046	0.788

Table 8 (continued)

Notch length (ins.)	Notch angle (°)	Notch shape	C_d	Mach number
2.25	7	V	0.0050	0.704
			0.0051	0.626
			0.0129	1.041
			0.0175	1.116
			0.0098	0.995
			0.0108	1.031
			0.01375	1.069
2.25	10	V	0.0233	1.152
			0.0165	1.085
			0.0112	0.965
			0.0085	0.860
			0.0071	0.80
			0.0067	0.705
			0.0064	0.62
			0.017	1.115
			0.0153	1.066
			0.0138	1.007
			0.0135	1.016
			0.0099	0.935
2.25	13	V	0.0183	1.14
			0.0164	1.118
			0.0153	1.085
			0.0161	1.063
			0.0159	1.056
			0.0158	1.016
			0.0146	0.985
			0.0132	0.924
			0.012	0.857
			0.0109	0.792
			0.0099	0.706
			0.0087	0.617
1.1	7	V	0.0172	1.14
			0.0128	1.08
			0.0058	0.979
			0.0044	0.836
			0.0044	0.64
1.0	10	V	0.0191	1.14
			0.0143	1.10
			0.0058	0.987
			0.0051	0.827
			0.0037	0.626

Table 8 (concluded)

Notch length (ins.)	Notch angle (°)	Notch shape	C_d	Mach number
1.0	13	V	0.0179 0.0138 0.0098 0.00613 0.0055	1.13 1.09 0.989 0.819 0.615
0.62	7	V	0.0157 0.0125 0.0035 0.0029	1.14 1.10 0.846 0.656
0.69	10	V	0.0143 0.0115 0.0051 0.0048 0.0033	1.135 1.08 0.993 0.774 0.590
0.56	13	V	0.0155 0.0115 0.0074 0.008 0.0047	1.13 1.08 1.008 0.824 0.608
0.375	7	V	0.014 0.0055 0.0032 0.0025 0.0016 0.0019	1.14 1.07 1.02 0.973 0.828 0.624
0.375	10	V	0.0145 0.0099 0.0034	1.13 1.09 0.568
0.375	13	V	0.014 0.0119 0.0060 0.0052	1.14 1.09 0.824 0.599

VITA

Ronald Hunter Howell was born on October 19, 1935 in Chicago, Illinois. He received the degree of Bachelor of Science in Mechanical Engineering from the University of Illinois, Urbana, Illinois in February, 1958 and the degree of Master of Science in Mechanical Engineering from the same institution in 1959.

His professional experiences include: summer employment during 1957 and 1959 with the Staley Mfg. Co., Decatur, Illinois, summer employment during 1961 and 1962 with the Missile and Space Systems Division of Douglas Aircraft Corporation, and summer employment during 1963 and 1966 with Aro, Inc., Tullahoma, Tennessee. Since 1959 he has been a full time faculty member at the University of Illinois in the Department of Mechanical Engineering. From 1959 until 1963 he was an instructor and since 1963 he has been an Instructor and Research Associate in Mechanical Engineering.

He has one publication which was done at Douglas Aircraft Corporation and was entitled "Particle Penetration Damage Studies in Phenolic Coverings."

He is a member of the American Society of Mechanical Engineers.